Optically Transparent Nanocellulose-Reinforced Composites *via* Pickering Emulsification

2019

Subir Kumar Biswas

Optically Transparent Nanocellulose-Reinforced Composites *via* Pickering Emulsification

by

Subir Kumar Biswas

A Thesis
Presented to the Graduate School of Agriculture of Kyoto University in Candidacy for the Degree of Doctor of Agricultural Science

Division of Forest and Biomaterials Science
Graduate School of Agriculture
Kyoto University
September 2019

Contents

Abstract

In this study, a facile method was developed to obtain transparent nanocomposites of immiscible native hydrophilic nanocelluloses and hydrophobic resin based on the concept of emulsification of oil and water. The method, called Pickering emulsification method, allowed to uniformly disperse the resin monomer in micro-droplet forms into the network of native nanocelluloses in the water medium. The dual role of the nanocelluloses, i.e., as the emulsion stabilizer and the resin reinforcing element, was exploited. The effect of the emulsion formulations, nanocellulose content, length, and crystallinity was investigated in terms of the emulsion morphology (resin droplet size), and the corresponding microstructure and properties of the nanocomposites resulted from the Pickering emulsification method. The nanocomposites uniquely combine 3D-moldability in macro-, micro- and nanoscale, and a high mechanical, optical, and thermal-stability performances compared to the nanocomposites prepared by impregnating the same resin into the nanocellulose-paper having a similar content of nanocelluloses. The unique behavior of the nanocomposites from Pickering emulsion was attributed to their self-assembled distinctive hierarchical microstructure originated by aggregation of the nanocellulose-network-encapsulated resin micro-droplets. Geared from the outstanding results obtained in the thermal stability of the nanocomposites, a highly thermally resilient silver nanowire transparent electrode was demonstrated using the nanocomposite as a substrate. This study, therefore, provides significant insights to fabricate unique transparent nanocomposites reinforced with native nanocelluloses by using facile Pickering emulsification technique for the application in next-gen advanced optical materials.

Chapter 1
General Introduction

1.1 Background of the study

Nanocelluloses, i.e., semi-crystalline cellulose nanofibers (CNFs) and their crystalline parts called cellulose nanocrystals or nanorods (CNCs or CNs), are one of the marvelous nature materials mainly produced in the plant cell walls. With their strength several times stronger than steel, CNFs not only support the huge body of a tree, but also offer an incredible potential as the sustainable and eco-friendly reinforcement material for man-made polymer nanocomposites. Also, the crystalline parts of a CNF have an incredible thermal-dimensional stability, and therefore, CNFs are highly effective to reduce the extreme thermal expansion of the polymers. Another advantage is that the thickness of the nanocelluloses are much smaller than the wavelength of the visible light, therefore, are free from light scattering in a transparent polymer matrix.

Despite the enormous potential of the nanocelluloses as the reinforcing component for polymers, ❶ the processing of nanocomposites suffers from the difficulty of uniformly dispersing “native” hydrophilic nanocelluloses in a hydrophobic resin matrix (most commercially available resins are hydrophobic). To be noted, a uniform dispersion of nanofillers in the matrix is an important factor in order to define good mechanical and optical properties of a nanocomposite. Therefore, many surface modification techniques have been employed to produce hydrophobically “modified” nanocelluloses, which make the composite fabrication process long, and often require expensive and hazardous chemicals. In 2005, Yano et al. offered a very simple method to produce transparent nanocomposite by impregnating hydrophobic resin monomer into a nanopaper of the native (non-modified) CNFs [1]. The impregnation of the resin monomer into the nano-voids in the nanopaper was due to the capillary action, and therefore, the hydrophilic-hydrophobic interaction was not a limiting factor. Because the CNFs were distributed uniformly in the nanopaper, and thus, in the impregnated nanocomposite, the nanocomposite was several times stronger, stiffer, and thermal-dimensionally stable than the neat polymer. Also, the optical transparency was maintained as high as the neat polymer. This transparent nanocomposite caught attention as the substrate for flexible optoelectronic devices due to the combination of desirable properties, of

which high transparency, flexibility and thermal-dimensional stability like glass were highly important. However, later it was found that ❷ the impregnation process is only limited to produce flat nanocomposites, i.e., three-dimensionally (3D)-molded transparent materials are not obtainable. This was because of the high stiffness of the nanopaper bestowed by intensive hydrogen bonding among the native CNFs. Therefore, many exciting applications of the nanocellulose-reinforced transparent nanomaterials, such as the substrate for smart-contact lenses and 3D-curved displays, could not be realized.

Aimed to address the above two issues, this dissertation describes the devising of a very simple water-based method by exploiting the idea of emulsification of oil and water, and its potential to fabricate structurally hierarchical, highly transparent, strong, tough, thermally-stable and macro-to-micro-moldable nanocomposites of hydrophilic 'native' nanocelluloses and hydrophobic resins for application in the next-generation optical materials.

1.2 Nanocelluloses: The nature's wonder material

Cellulose, the long-chain polymer of β-D-glucose, is found in nature as the extended semi-crystalline fibrils which primarily serve the mechanical function in the trees, plants, marine creature tunicates, algae, and bacteria. Cellulose-rich materials such as wood, cotton, linen etc. have been used as engineering materials from ancient era. Their present use is still unprecedented in our modern civilization as endorsed by the enormous growth of industries in forest products such as construction materials (wood, timber, lumber, glued laminated timber, impreg, compreg, wood-composites, etc.), pulp-paper and packaging, textiles, and so on. These are often called "first generation or traditional cellulosic materials" that took advantages derived from the natural hierarchical design, which covers nano- to macro-scale dimensions [2]. The hierarchical design of the wood, the mostly used cellulosic material, is illustrated in Figure 1.1.

On the smallest length scale, about 20–50 cellulose chains are stacked parallel by van der Waals and intermolecular hydrogen bonds between hydroxyl groups and oxygens of the adjacent cellulose molecules that form about 3–5-nm-thick fibrils [2–5]. These are called elementary fibrils or microfibrils (MFs) (Fig. 1.1). The MFs are further aggregated into 15–50-nm-thick and several micrometers long fibrils called MF bundles [2]. The MF bundles are further arranged into lamellar structure (layers) surrounded by the matrix substances (hemicell-

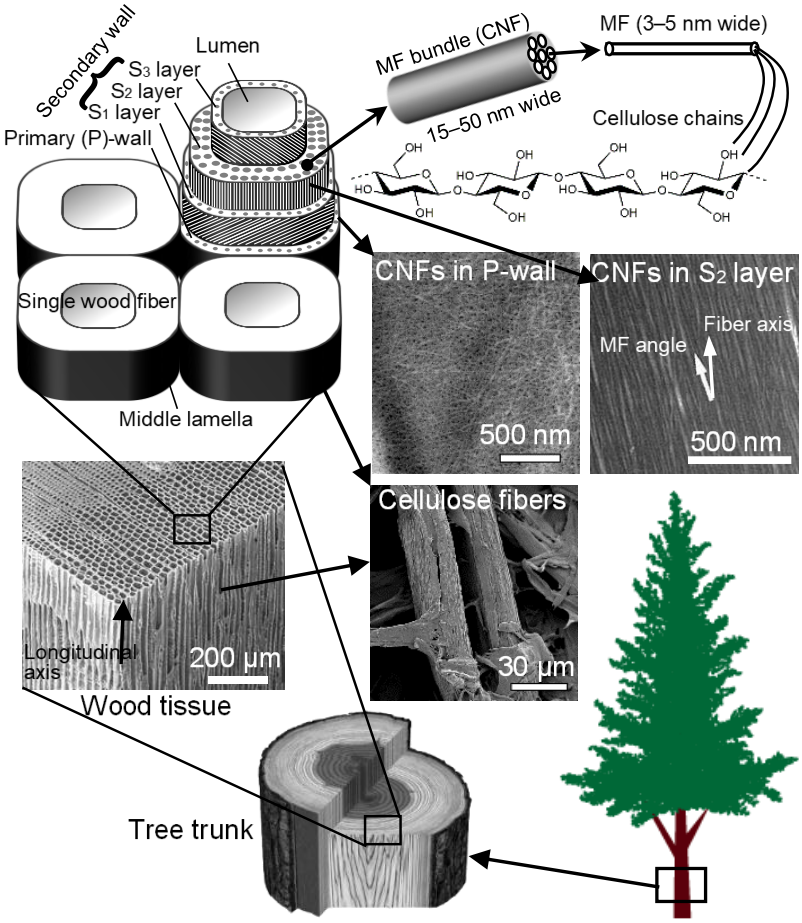

Figure 1.1. Illustration of the hierarchical structure of the wood on different length scales.

uloses, lignin etc.) to form the wall of the fibers (cells) – the building blocks of the plant body [6–8]. Given their diameter below 100 nm, the 'cellulose MF bundles' including the elementary fibrils (MFs) are presently termed as 'cellulose nanofibers (CNFs)'.

The CNFs are semi-crystalline, that is there are regions where the cellulose molecules are arranged in a highly ordered fashion called crystalline region, and regions that are disordered called amorphous region (Fig. 1.2). The amount of crystalline region varies from plant to plant. The crystallinity can be 90–100% in plant-based fibers (for example, cotton) and 60 – 70% in wood-based fibers [9]. The crystalline regions contained in the CNFs can be retrieved by acid hydrolysis resulting in cellulose nanocrystals or nanorods (CNCs or CNs) (Fig. 1.2b) [9,10]. The cellulose molecules in the crystalline regions are intimately packed by the intra- and inter-molecular hydrogen bonding network that bestows the CNFs and CNCs a high axial stiffness. Therefore, the semi-crystalline CNFs constitute the main reinforcement phase for trees and plants.

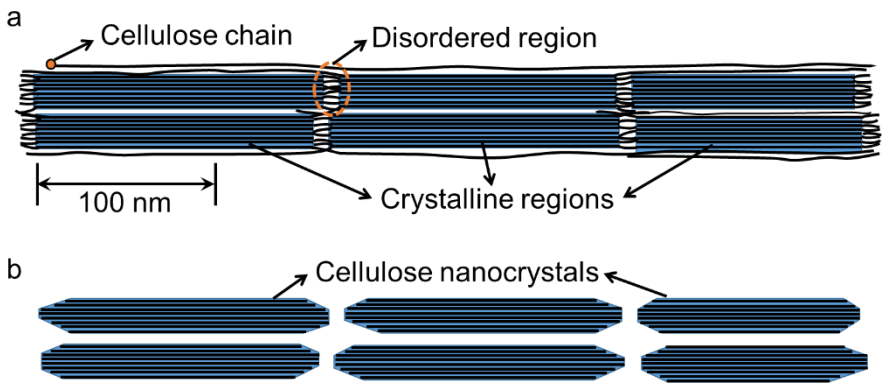

Figure 1.2. (a) Model CNFs with the semi-crystalline configuration, and (b) CNCs that can be retrieved after the removal of amorphous (disordered) regions via acid hydrolysis [2]. Adapted with permission from ref. 2 © 2011 The Royal Society of Chemistry.

The nanocelluloses, i.e., CNFs and CNCs or CNs, have many unique properties. The crystalline parts of semi-crystalline CNFs, having an extended structure of parallel cellulose chains, is extremely stiff with an axial elastic modulus of ~140 GPa [2,11–14]. The elastic modulus is comparable to Kevlar, and even comparable to some species of carbon fibers (see Table 1.1). CNFs having a comparatively low density, they weigh only $1/5^{th}$ the weight of the steel, yet the tensile strength is roughly 4 to 19 times higher than that of the different species of steels (Table 1.1). When normalized with respect to density, the specific elastic modulus (i.e., specific stiffness) of CNFs is about 3 times higher than that of stainless steels (Table 1.1). Another fascinating property of the crystalline nanocelluloses is their very low linear thermal expansion coefficient (CTE) at about 0.1 ppm K^{-1} [15]. Put another way, their CTE is about $1/50^{th}$ that of the ordinary glass and comparable to quartz crystals [16,17].

Therefore, the expression "nature's wonder material'' is truly plausible for the nanocelluloses with their fascinating material properties described above. These 'green' high-performance material is abundantly and sustainably extractable from plants including trees, considering a global production of approximately 100 billion tons per annum through photosynthesis [16]. Hence, nanocelluloses are presently being regarded as the novel 'green' reinforcement components for the production of 'next-generation cellulosic materials' to meet the demands of the modern sustainable society for the high-performance materials.

Table 1.1. Properties of crystalline cellulose and various other reinforcing materials. Adapted with permission from ref. 2 © 2011 The Royal Society of Chemistry.

Material	Density ($g\ cm^{-3}$)	Tensile strength (GPa)	Axial elastic modulus (GPa)	Transverse elastic modulus (GPa)	Coefficient of thermal expansion (CTE) ($ppm\ K^{-1}$)	References
Kevlar-49 fiber	1.4	3.6 – 4.1	124 – 131	2.5	–2.0	[18,19]
Carbon fiber	1.8	1.5 – 5.5	150 – 500	–	–0.6	[19]
Mild steel	–	0.4 – 0.6	194 – 243	–	–	[20]
High strength steel	–	0.8 – 0.9	207 – 242	–	–	[20]
Stainless steel	7.8	0.4 – 1.8	193 – 204	–	10.2 – 17.2	[19]
Clay nanoplatelets	–	–	170	–	–	[21]
Carbon nanotubes	–	11 – 63	270 – 950	0.8 – 30	–	[22,23]
Boron nanowhiskers	–	2 – 8	250 – 360	–	–	[24]
Crystalline cellulose	**1.6**	**2 – 7.7**	**~140**	**10 – 50**	**0.1**	[11–15,25–30]

1.3 Isolation of nanocelluloses

1.3.1 Isolation of CNFs

The source materials of CNFs include wood [31], plant [32,33], tunicate [34,35], algae [34,36], and bacteria [34,37–39]. However, the most common and commercially viable sources are the woods and plants which comprise about 0.1 trillion tons of cellulose on the earth.

The simplified extraction routes of CNFs from wood and plants are shown in Figure 1.3. The extraction of CNFs from lingo-cellulosic materials (wood and plants – in particulate form) starts with the chemical purification to liberate the cellulose fibers (also called pulp fibers) from the matrix of lignin and hemicelluloses. The process is well-known in the pulp and paper industries as the 'Kraft process or sulfate process' or 'sulfite process'; the most common laboratory purification process is called 'Wise method', where repeated treatment of the lingo-cellulosic particles with acidified sodium chlorite ($NaClO_2$) and potassium hydroxide (KOH) is done to remove the matrices [40,41]. The purified cellulose fibers can then be directly nano-fibrillated by mechanical treatment in a never-dried condition either using grinder [41], high-pressure homogenizer or microfluidizer [42–46], or high intensity ultrasonics [47,48]. Typically, purified cellulose materials are fed several times (i.e., number of passes) through the mechanical disintegrator. After each pass, the particles gradually get smaller and more uniform in width. Abe et al. [41] pioneered in extracting the CNFs in native (unmodified) state with a uniform width of 15 nm by feeding the purified wood-cellulose fibers only one-time through a grinder having two grind-stones assembled in a rotor-stator configuration (Fig. 1.4a).

To facilitate nano-fibrillation of the purified cellulose materials, a chemical or enzymatic pretreatment can be applied before the mechanical treatments (Fig. 1.3-2a and 2b) [4,45,46,49,50]. Those pretreatments help swell the fiber-wall that effectively loosen the interfibrillar hydrogen bonds and hence facilitate the extraction of the finer fibrils during the subsequent mechanical treatments. The enzymatic treatment does not modify the cellulose because it only attacks the amorphous regions of the cellulose microfibrils, and thus reduces the energy requirements during the mechanical fibrillation by a homogenizer/microfluidizer [45,46,50]. A chemical treatment usually introduces charges to the cellulose (i.e., modifies its surface), which helps the fiber to swell more. For example, TEMPO (2,2,6,6-tetramethylpiperidine-1-oxyl radical)-mediated oxidation can introduce carboxylate charges to the cellulose by oxidation of the hydroxyl groups (oxidation of primary alcohols) [4,49]. After

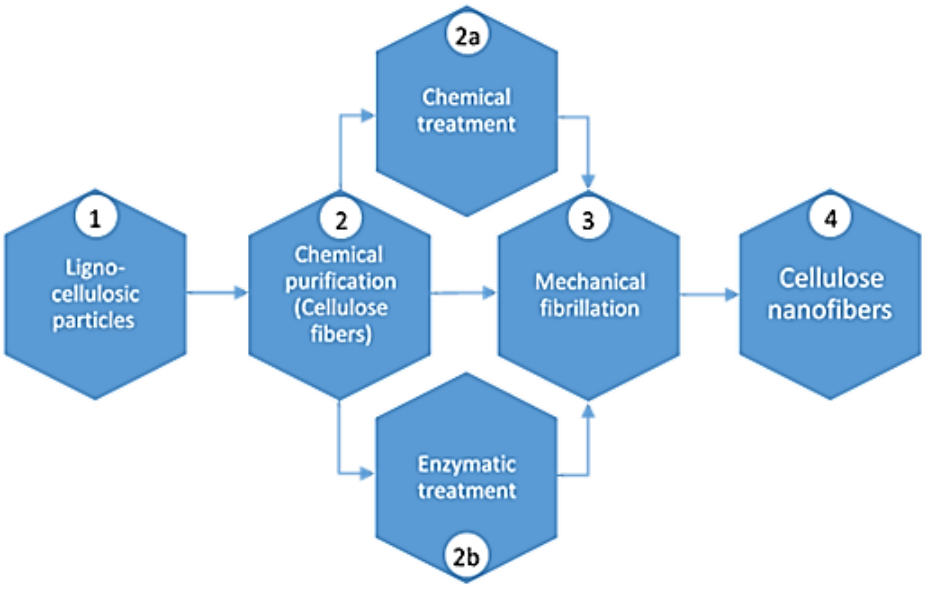

Figure 1.3. Simplified extraction steps of CNFs from wood or plants.

TEMPO pretreatment of the cellulose fibers followed by disintegration via a mild magnetic stirring, the CNFs can be obtained with a width of 3–5 nm (Fig 1.4b). Therefore, the TEMPO treatment helps liberate CNFs in their elementary dimensions (Fig. 1.1.).

The width of the CNFs may vary from 3 nm to 50 nm depending on the extraction steps used and the biological source of the cellulosic materials. The fibrils can be obtained approximately 500 nm to >2 µm in length, thus have very high aspect ratio [2,51].

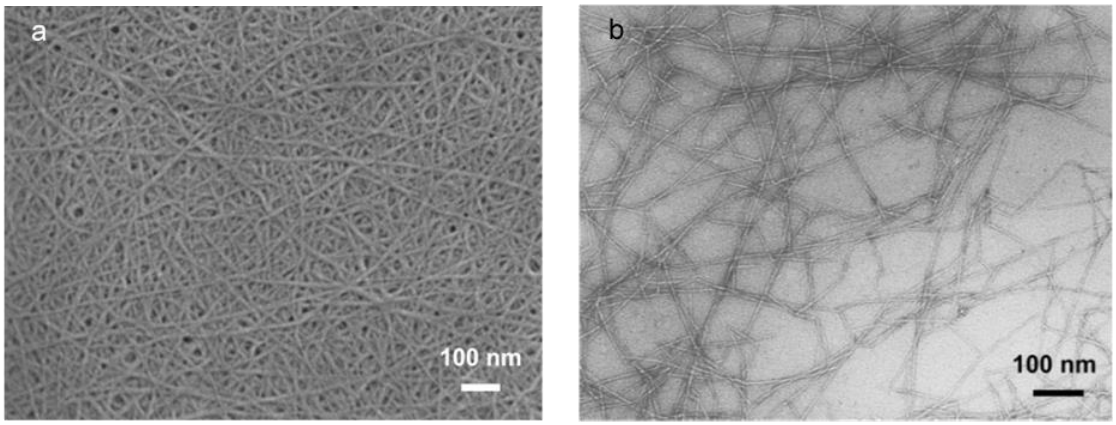

Figure 1.4. (a) Native cellulose nanofibers with 15 nm width obtained after one-pass grinder treatment [41], and (b) TEMPO-oxidized cellulose nanofibers (surface modified; carboxylate content 1.5 mmol g^{-1}) with 3–4 nm in width obtained after mild magnetic stirring [4,49]. Both nanofibers were prepared under a never-dried condition. Reproduced with permission from (a) ref. 41 and (b) ref. 49 © 2007 American Chemical Society.

1.3.2 Isolation of CNCs

The crystalline regions contained in the MFs (i.e., CNFs) can be retrieved by acid hydrolysis resulting in cellulose nanocrystals CNCs (Fig. 1.2 and 1.5) [9,10]. CNCs are rod-like or whisker-shaped in appearance with tapering ends, therefore, are often called cellulose nanowhiskers or cellulose nanorods (CNs). The CNCs can be obtained from any cellulosic source materials such as wood and non-wood fibers, bacteria, algae, tunicate, microcrystalline cellulose (MCC), microfibrillated cellulose (MFC) and CNFs.

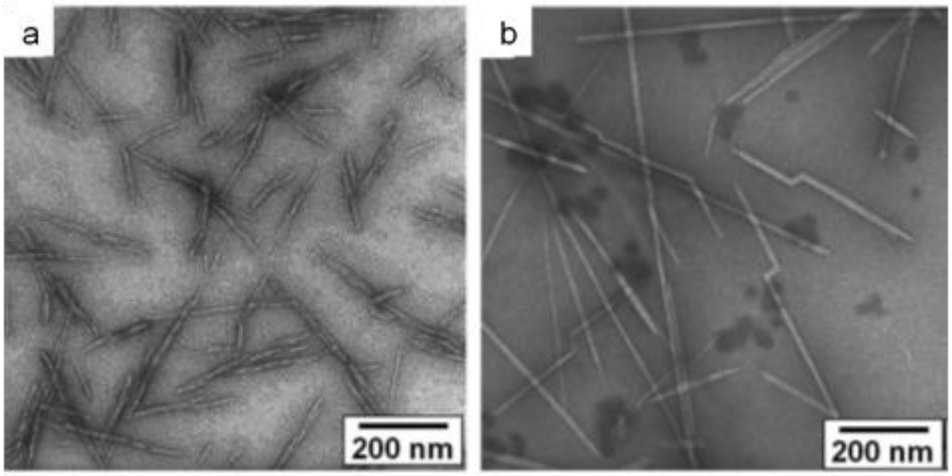

Figure 1.5. (a) CNCs retrieved from wood fibers, and (b) CNCs retrieved from tunicin [2]. Reproduced with permission from ref. 2 © 2011 The Royal Society of Chemistry.

Acid hydrolysis preferentially attacks and removes (hydrolyze) the amorphous parts (disordered regions) within the cellulose MFs. Sulfuric acid (H_2SO_4) [52], hydrochloric acid (HCl) [53,54], maleic acid [55], formic acid [56] etc. have been used to obtain CNCs. Among them, H_2SO_4 is most widely used because it can create a harsh condition that can effectively remove the amorphous parts of the cellulose MFs. So, the CNCs can even be obtained directly from the bigger particles of cellulosic materials. H_2SO_4 hydrolysis also modifies the CNCs by introducing sulfonate ester groups on their surface [2,10], the negative charge of which leads to a stable CNC/water suspension [2]. In contrast, HCl hydrolysis does not introduce any surface groups, hence, CNCs can be obtained in unmodified state [10].

The width, length and crystallinity of the retrieved CNCs highly varies depending on the cellulosic source, and the hydrolysis condition such as the concentration of acids, time and temperature. The width may vary from 3 nm to ~20 nm. The typical length is below 500 nm, but may vary from 50 nm to 4000 nm [2]. The CNCs are highly crystalline, for example, the

crystallinity of CNCs obtained from wood- and plant-based cellulose sources is reported to be 54–88% [2]. The CNCs obtained from tunicate can have crystalline of 85–100% [2].

1.4 Nanocellulose-reinforced composites

The concept of utilizing nanocelluloses as the reinforcement fillers in the composites (i.e., nanocomposites) has been derived from the prospect of exploiting their many unique properties. Nanocelluloses have high strength, stiffness and aspect ratio, low thermal expansion, and excellent functionality (such as, ability to form strong network via hydrogen bonding, amenable to chemical modification, etc.), and perhaps most importantly, in the context of environmental concerns, they are bio-derived. One of the earliest introductions of nanocelluloses in the form of nanowhiskers (from tunicates) with width 10-20 nm and lengths ranging from 100 nm to several micrometers in the polymer matrix was reported by Favier et al. in 1995 [57,58]. The cellulose nanowhiskers were mixed with the copolymer latex of styrene (35% w/w) and butyl acrylate (65% w/w). A 6 % (w/w) nanowhiskers content in the film-casted composite showed more than two orders of magnitude higher mechanical properties than that of pure copolymer film.

Nanocellulose-reinforced composites are usually fabricated either by mixing the nanocellulose suspension (in water) with a polymer matrix followed by film-casting, or by impregnating the curable monomer/polymer into the porous nanocellulose network, such as a CNF-nanopaper. In the case of mixing method, the polymers usually chosen are hydrophilic to have a good miscibility between the components in order to ensure a uniform dispersion of the nanocelluloses. A high quality dispersion of the nano-fillers is inevitable for the maximum performance of the composites [59–62]. On the contrary, had it been the case of hydrophobic polymer matrix, the uniform dispersion of the nanocelluloses would have obliterated, because the nanocelluloses tend to agglomerate [63–65]. The hydrophobic polymers are the most commonly used matrix material; more than 85% of the Japanese plastic market is occupied by the hydrophobic polymers [66]. Therefore, the surface of nanocelluloses is often modified (acetylation is the most common chemical surface modification) to give them hydrophobicity in order to improve the dispersion and adhesion in the hydrophobic matrix [64,65].

As an alternative to surface modification, nanocelluloses can be self-assembled in a 3D-network-structure by making a nanopaper or gel, and then the matrix polymer can be imbibed, directly (in the case of nanopaper) or followed by a solvent-exchange procedure (in the case of

gel), into the network by immersion in the monomer/polymer solution [1,67–69]. The process is straight-forward, broadly applicable, and permitting the fabrication of 'native' nanocellulose-based nanocomposites with otherwise immiscible components.

In 2005, for the first instance, Yano and his research group developed a fascinating optically transparent CNF-reinforced flexible nanocomposite by impregnating transparent monomer resin into the CNF-nanopaper followed by polymerization of the monomer (Fig. 1.6a,b) [1,67]. Generally, composite materials lose transparency due to the non-matching refractive indices (RI) of the components that cause light scattering to happen. However, the research group pointed out that because of the one-tenth width of the CNFs (i.e., about 20–50 nm) than that of the visible light wavelengths, the effect of the non-matching RI and hence the associated light scattering was minimized. Of note, they impregnated acrylic resins (RI= 1.488, 1.532 and 1.596) and epoxy resin (RI= 1.522) into the CNF-nanopaper; the RI of cellulose is 1.544 in the transverse direction and 1.61 in longitudinal direction [1,67,70]. The transparencies of those nanocomposites were more than 80%, which were merely 8% lower than that of the pure polymers used. A mechanical strength five times than that of the engineered plastics with a drastically low CTE was obtained. The CTE obtained was as low as 6 ppm K^{-1}, which was 8 to 33 times lower than that of the most transparent plastics (50 to >200 ppm K^{-1}), at a nanofiber content of 70 wt% [1,71,72]. The CTE was comparable to glass (7–10 ppm K^{-1}), the mostly used transparent substrate in the optoelectronic devices [73]. Considering the unique material properties of the CNF-reinforced transparent nanocomposite films and their amenability as a flexible substrate for the "roll-to-roll" processing, they caught attention as the potential innovation in the optoelectronic industries (Fig. 1.6c) [17,74,75].

1.5 Emulsion and 'Pickering' emulsion

1.5.1 Emulsion

Emulsion is a type of colloidal dispersion [76,77]. A basic colloidal dispersion consists of two phases: dispersed and continuous phase, either of which can be a gas, liquid or solid. The dispersed phase consists of a dispersion of small particles, droplets, or bubbles, having dimensions (at least one) in the order of a few molecule in size to a few micrometers [76,77]. Depending on the forms of the dispersed and continuous phases, i.e., either a gas, liquid or solid, a colloidal system can be termed as an aerosol, foam, emulsion or a suspension (Table 1.2) [77].

Figure 1.6. (a) A bacterial cellulose nanofiber (BC)-reinforced acrylic resin nanocomposite [1], (b) a wood-CNF-reinforced acrylic resin nanocomposite [67], (c) an organic light-emitting diode (OLED)-display fabricated on a flexible, low-CTE and optically transparent wood-CNF/acrylic resin nanocomposite [74]. Reproduced with permission from (a) ref. 1 © 2005 John Wiley and Sons, (b) ref. 67 © 2005 Springer Nature, and (c) ref. 74 © 2009 Elsevier.

Table 1.2. Types of colloidal dispersion [77]. Adapted with permission from ref. 77 © 2006 John Wiley and Sons.

Name	Continuous phase	Dispersed phase
Liquid aerosol	Gas	Liquid
Solid aerosol	Gas	Solid
Foam	Liquid	Gas
Emulsion	**Liquid**	**Liquid**
Sol, suspension	Liquid	Solid
Solid foam	Solid	Gas
Solid emulsion	Solid	Liquid
Solid suspension	Solid	Solid

A colloidal system can either be thermodynamically stable or metastable. The thermodynamically stable colloids are formed spontaneously. But, the metastable colloidal system requires an extra energy input to form. There are two ways to obtain a metastable colloid: (1) nucleation and growth (including precipitation), and (2) fragmentation of the dispersed phase. In either cases, the dispersed droplets or bubbles tend to coalesce due to the non-equilibrium behavior of this colloidal system. The non-equilibrium nature probably arises because of the different surface energies of the constituent dispersed and continuous phases. Therefore, specific surface active agents, called surfactants, are usually recruited to stabilize the interfaces of the fragments or growing nuclei of the dispersed phase into the continuous phase to prevent coalescence [76].

Emulsion is a dispersion system of two immiscible liquids – in general, oil and water (i.e., hydrophilic and hydrophobic liquids) [76–82]. The dispersed phase consists of a numerous droplets of one liquid in another liquid, i.e., continuous phase. Emulsions are produced by applying a shear force (blending, high-pressure homogenization, or pressurization through a membrane/microchannels) to two immiscible liquids, resulting in the fragmentation of one liquid into the other, in the presence of surfactants (Fig. 1.7). Emulsion, therefore, is an example of metastable colloids. Emulsion droplets exhibit all classical behaviors of metastable colloids: Brownian motion, reversible phase transitions as a result of droplet interactions, and irreversible transitions that generally involve the destruction of the emulsion [76].

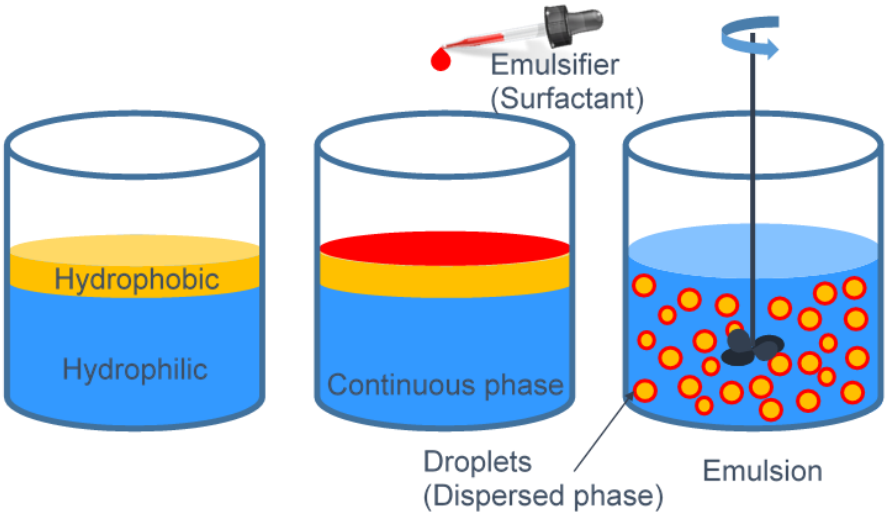

Figure 1.7. The process of emulsion formation – ‘Emulsification’.

1.5.2 Types of emulsions

Emulsions are generally classified according to the spatial presence of the constituent phases [83], i.e., dispersed and continuous phases, either oil (O) or water (W), relative to each other, and by the size and distribution of the droplets [83,84]. Depending on the spatial presence of the constituent phases, emulsion is classified in two board types: (1) primary emulsion, and (2) secondary or double or multiple emulsion.

(1) Primary emulsion contains one-component dispersed phase (Fig. 1.8), for example, oil-in-water emulsion (O/W) and water-in-oil emulsion (W/O) [77,82,83,85]. Milk is an example of O/W emulsion. An oil-in-oil (O/O) emulsion can happen if it contains a polar oil (such as, propylene glycol) dispersed in a nonpolar oil (such as, paraffinic oil), and vice versa [81,82]. A 'mixed emulsion' where dispersed droplets of two different origins that do not mix in a continuous medium can also be obtained [82].

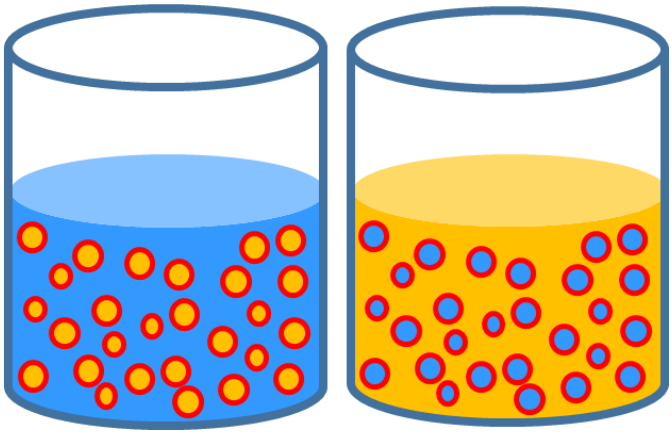

Figure 1.8. Primary emulsions – an oil-in-water emulsion (O/W) (left) and a water-in-oil emulsion (W/O) (right).

(2) Secondary or double or multiple emulsion contains two- or multi-component dispersed phase (Fig. 1.9), for example, oil-in-water-in-oil (O/W/O) and water-in-oil-in-water (W/O/W). These are obtained by making a primary emulsion followed by adding a continuous phase, and hence called 'emulsions-of-emulsions' [77,82,83,85,86].

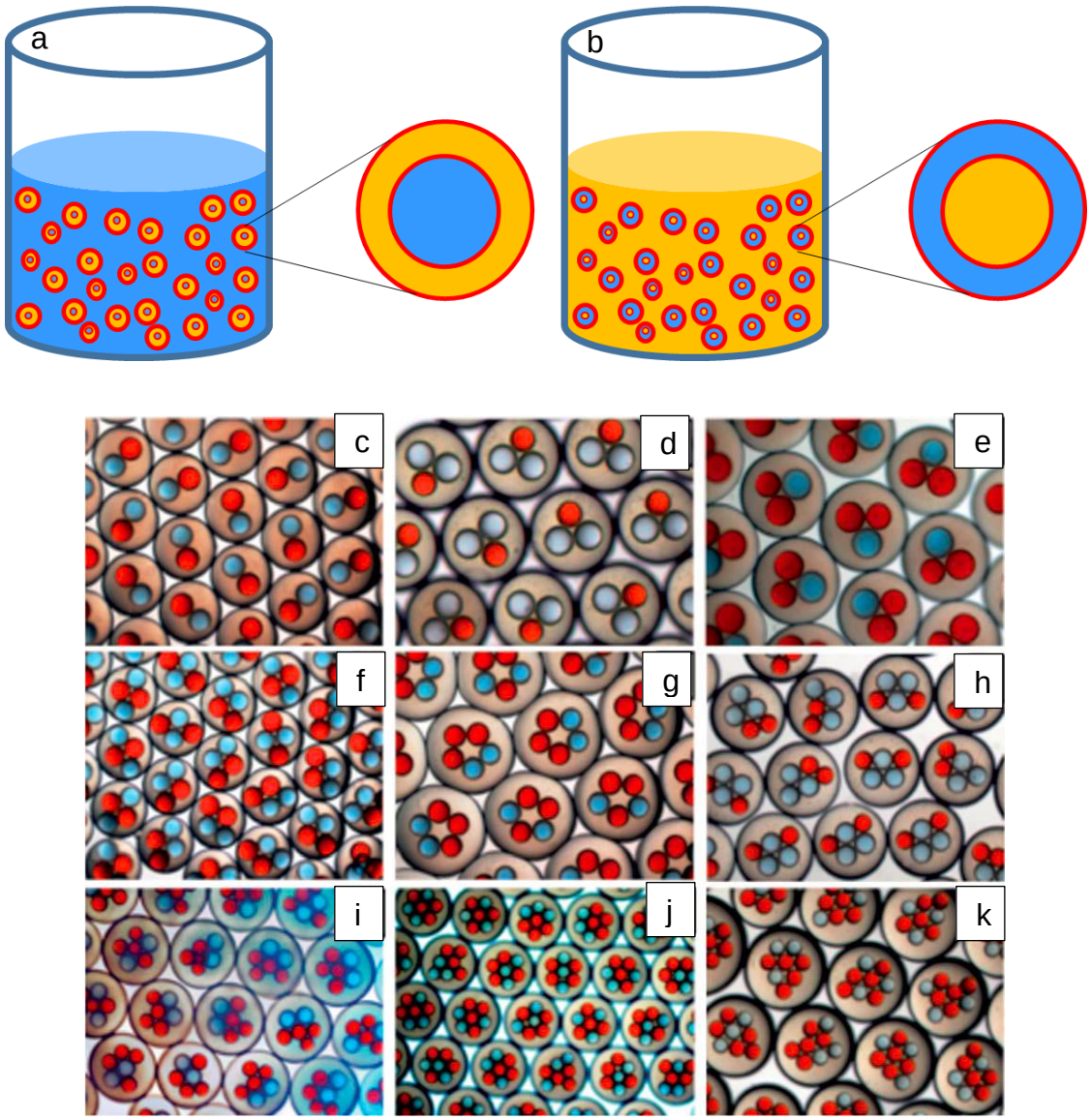

Figure 1.9. Secondary or double emulsions – (a) a water-in-oil-in-water emulsion (W/O/W), and (b) an oil-in-water-in-oil emulsion (O/W/O) (top right). Figures (c–k) show the examples of the multi-component double emulsions [86]. Reproduced with permission from ref. 86 © 2012 The Royal Society of Chemistry.

Meanwhile, the emulsion depending on the droplet diameter can be divided into four (4) groups. However, the range of the droplet diameter in each group varies from literature to literature [77,82–84,87–90].

(1) Macroemulsions: Emulsions that consist of dispersed droplets with diameter more than 1 µm [84].

(2) Miniemulsions: These emulsions contain droplets ranged between 100 nm to 1 µm [84].

(3) Microemulsions: Microemulsions are those having droplets of less than 100 nm diameter [77,84]. However, the range is specifically given between 5 and 50 nm in many literatures [78,79]. Whereas, other emulsions are metastable, i.e., not thermodynamically stable, the microemulsions are thermodynamically stable. This means that they form spontaneously given a sufficient time. The spontaneous emulsion formation may happen when a co-surfactant is added to an oil/water/surfactant system that causes the interfacial tension to drop to near zero, often on the order of 10^{-3}–10^{-4} mN m^{-1}, resulting in very small droplets [77,90]. Because of the much smaller droplet diameters than the visible light wavelengths that minimize light scattering, the emulsion is optically transparent [83].

(4) Nanoemulsion: is fairly a "new term" that consists of very small droplets with the mean diameter between 20 and 100 nm [82,83,87–89]. By virtue of the smaller droplet size than the wavelength of light, nanoemulsions also tend to be transparent or translucent. Due to very small droplet size, they have much better stability to gravitational separation and aggregation than the conventional emulsions (macroemulsion and miniemulsion), and hence are considered kinetically stable [87,88]. However, as oppose to microemulsions, nanoemulsions are still thermodynamically unstable systems because the separate oil and water phases have a lower free energy than the emulsified oil and water phases (as similar to the conventional macroemulsion and miniemulsion) [83].

In addition, according to the distribution of the droplet diameter, an emulsion can be classified as the monodispersed or polydispersed [76]. The monodisperse emulsion contains almost equal-sized droplets as shown in Figure 1.9c–k. The polydisperse emulsion contains droplets of different radii (Fig. 1.10).

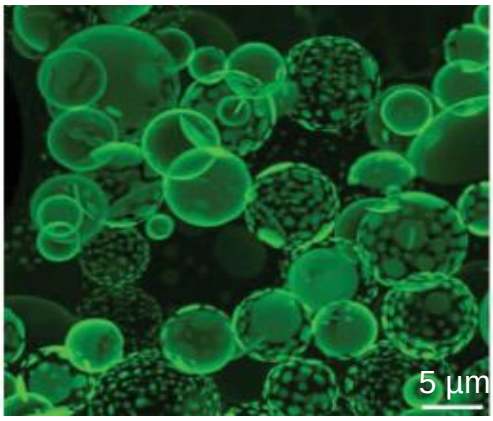

Figure 1.10. An example of a polydisperse emulsion [91]. Reproduced with permission from ref. 91 © 2013 The Royal Society of Chemistry.

1.5.3 Surfactant or emulsifier

In order to disperse one liquid in another immiscible liquid, a surface-active agent is required [76–84,90,92]. It is called as surfactant or emulsifier. Surfactants are usually long-chain molecules and are amphiphilic in nature, i.e., they combine both hydrophilic and hydrophobic moieties in a single molecule as shown in Figure 1.11. During emulsion formation, these molecules adsorb (or locate) at the interfaces of oil and water, thereby alter the surface and interfacial properties significantly. The orientation of the moieties of these molecules is naturally driven by their greatest affinity to the liquid of similar character. Put another way, the hydrophilic end will orient towards the water and the hydrophobic end will orient towards the oil droplets (Fig. 1.11), thereby stabilize the droplets in the emulsion and ensure that they do not coalesce. Surfactants lower the interfacial tension and surface energy of the dispersed phase, which in turn cause a reduction in the droplet size. The surfactant or emulsifying agent has a key role not only in the formation of the emulsion but also for its long-term stability [76–84,90,92].

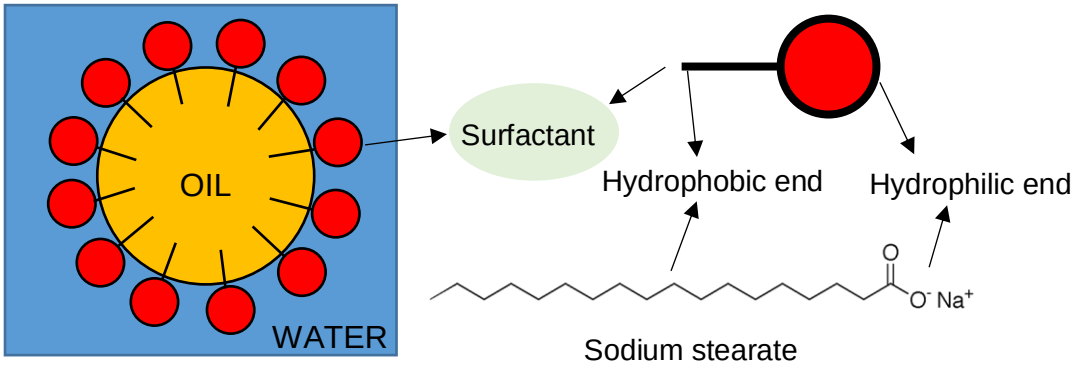

Figure 1.11. Schematic representation of surfactant molecules having an amphiphilic property.

The characteristic of the surfactant can also govern the occurrence of the phases, i.e., either the oil or the water would constitute the dispersed phase or the continuous phase. The character is often determined by the hydrophilic-lipophilic balance (HLB) of a surfactant. The HLB is a measure of how much hydrophilic or hydrophobic a surfactant is, and is determined by calculating the molecular weights of the different parts of a surfactant molecule [92–95]. Griffin's equation [94] for calculating the HLB value of a non-ionic surfactant is:

$$\mathrm{HLB} = 20 \times \frac{\mathrm{M_h}}{\mathrm{M}} \tag{1.1}$$

Where, M_h is the molecular weight of the hydrophilic part of the surfactant molecule, and M equals the total molecular weight of the surfactant molecule. The equation gives HLB value from 0 to 20 that corresponds to a completely hydrophobic (lipophilic) to a completely hydrophilic molecule. Figure 1.12 below shows the function of a surfactant based on the HLB values.

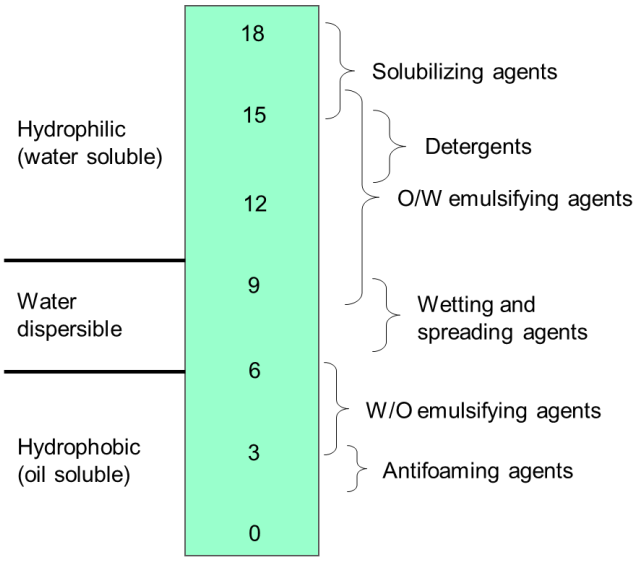

Figure 1.12. HLB scale showing classification of surfactant function. Adapted from ref. 92.

1.5.4 Pickering emulsion

Pickering emulsion is described as an emulsion in which the dispersed phase is stabilized by the solid particles. The emulsion stabilizing effect of solid particles was first recognized by Walter Ramsden in 1903 [96]. However, the phenomenon was explained by S. U. Pickering in 1907, thereby called 'Pickering stabilization' and such stabilized emulsions are called 'Pickering emulsions' [97].

Solid particles of sizes ranging from several nanometers to several microns (for example, colloidal silica) strongly adsorb onto the interfaces of oil and water (Fig. 1.13a). The adsorption happens irreversibly at the interfaces, as oppose to conventional surfactants that adsorb and desorb quickly with thermal fluctuations, consequently form a mechanical barrier that effectively prevent droplet coalescence [77,98–100]. Particles that are to be used as the emulsifying agents must have wettability by both liquids. Particles that completely wetted by water (i.e., completely hydrophilic) or oil (i.e., completely hydrophobic) remain dispersed in

either of the phases, and hence no emulsion will be obtained. Therefore, the solid particles with intermediate wettability are desired [76,77,84,98–103].

The wettability of particles is expressed as the contact angle, θ, which they make with the oil-water interface through the water phase (Fig. 1.13b,c). Preferentially, the liquid that wets the particles most will constitute the continuous phase in the emulsion. Considering an emulsion to be formed with equal parts of oil and water, the relatively hydrophilic particles, where $\theta < 90°$, will make an O/W emulsion (Fig. 1.13b). Whereas, relatively hydrophobic particles with $\theta > 90°$ will form W/O emulsion (Fig. 1.13c). Particles that are partially hydrophobic or hydrophilic, i.e., $\theta = 90°$, are better emulsion stabilizers because they are partially wettable by both liquids, and therefore anchor better to the surface of the droplets. The energy required to stabilize the system in this case is minimum [76,84,98,100–103].

There are plenty of particles, both inorganic and organic, that have partial wetting ability for most common oils. For example, silica [102], calcium carbonate and barium sulfate [104], clay particles such as montmorillonite [104,105] and laponite [106], carbon black [107–109], latex [110,111], magnetic particles [112], carbon nanotubes [113], block copolymer micelles [114] and so on. Pickering emulsion stabilization ability of proteins, chitin nanocrystals, and starch nanocrystals have been also reported [115–119]. Many of these particles are nanometric in size having diameter <100 nm such as laponite, block copolymer micelles, starch and chitin nanocrystals; whereas, many are submicron to several micrometer in size such as latex, fumed silica etc. There are many particles that are very hydrophilic and required to be incorporated a partial hydrophobic moiety (mostly by means of chemical modification) in order to ensure the partial wetting by both water and oil [103].

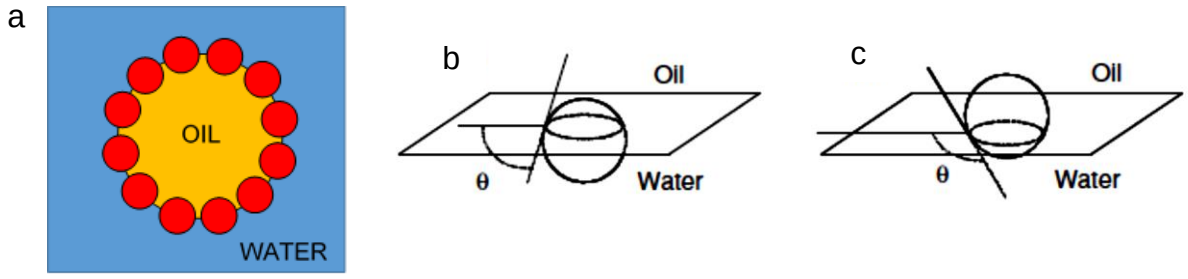

Figure 1.13. (a) Schematic of the adsorption of solid particles at the oil-water interface. (b,c) The contact angle, θ, of a particle adsorbed at the water–oil interface, where the particle is preferentially wetted by (b) water and (c) oil [76]. (b,c) Reproduced with permission from ref. 76 © 2007 Springer Nature.

1.5.5 Applications of emulsions

Emulsions are widely used in a variety of industrial applications. One of the most important applications is in medicine and drug-delivery – droplets of oil in water allow transport oil soluble medicines and ultimately release them on a chosen target in certain dosages. Many personal care and cosmetic products, such as hand-creams, lotions, hair-sprays and sunscreens, are emulsions. Foods such as mayonnaise, salad creams, deserts, butter and beverages are also emulsions. Milk is a natural emulsion of fat (oil)-in-water stabilized by protein and other compounds (calcium and phosphorus). In fact, the word ‘emulsion’ comes from the Latin word "to milk". Emulsions are often used in pharmaceuticals (capsules, syrups) and agrochemicals (pesticides, herbicides). Because, the active ingredients are usually water insoluble, therefore their emulsions with water in effective dosages are used [76,77,81,82].

Emulsification is one of the effective methods in fire-fighting, especially at extinguishing fires on small, thin-layer spills of flammable liquids (e.g., hydrocarbons). The water containing emulsifying agents is applied on the fire through a high-pressure nozzle. Emulsifying agents encapsulate the flammable liquids and trap into the water phase [120].

Another important application of emulsion technology includes all kinds of surface treatments such as painting, paper coating, road surfacing, and lubricating. In painting, paper coating, and lubricating processes, emulsion technology allows to avoid organic solvents by dispersing hydrophobic substances into water. This reduces the risks to the environment from organic solvents. Upon application of emulsion on a surface, water is safely evaporated to the environment, while the dispersed phase concentrates to form a desired hydrophobic film. Meanwhile, many hydrophobic substances are almost solid at room temperature. Dispersing it as small particles in oil followed by emulsification with water helps keep it fluid at room temperature. Bitumen used for road surfacing is a good instance [76,77,81,82].

Emulsion technology is highly used in petroleum and mining industries probably throughout all stages of the process. For example, oil-recovery, pipeline transportation, refinery process, and so on. Emulsification is often used to transport crude oils over a large distance. The advantage of emulsification is that it helps avoiding the use of diluents or heat which would otherwise be required to decrease the oil viscosity sufficiently for pumping through the pipeline [76,77,81,82].

Oil spillage is a significant cause of marine environment pollution. The spilled oil, in

addition to drifting and evaporation, may form O/W emulsion by the help of water turbulence due to wind and wave energy. Emulsion formation helps disperse oil into the water column and keeps the oil away from sensitive shorelines. The oil droplets usually get weathered, accumulate sea water-suspended fine solids, and finally settle down. Therefore, the authority usually promotes emulsion formation, if there is a case of oil spillage [76,77,81,82].

Recently, Pickering emulsions have gained much attention in different fields including cosmetics formulation, food engineering, pharmaceuticals, and nanocomposite materials [100–103]. The significance of Pickering emulsion arises from the fact that the harmful organic surfactants can be completely avoided as desirable in the cosmetic and pharmaceutical fields, and replaced by environmental friendly particulate materials with added functionalities.

Pickering emulsification towards the fabrication of nanocomposite materials is of particular importance. It offers an easy water-based fabrication approach, where the uniform dispersion of nanoparticles in an incompatible matrix is difficult to achieve. Also, this approach offers the possibility for the development of high performance nanocomposites with a well-controlled and well-designed nanostructure. Haaj et al. reported the preparation of mechanically improved acrylic and latex nanocomposites reinforced with starch nanocrystals via film-casting of their Pickering emulsions [119,121]. Highly conductive composites have been prepared by stabilizing latex particles of different polymers such as poly(methyl methacrylate), poly(styrene-co-acrylonitrile), poly(methyl methacrylate/butyl acrylate), etc. using graphene as the stabilizer followed by evaporation of the water [120]. Recently, Shams and Yano fabricated a novel double-curved chitin nanofiber-reinforced transparent composite via vacuum-filtration of Pickering emulsion [122]. These works demonstrate that the Pickering emulsions can even be dehydrated via film-casting or vacuum-filtration without any leakage of the oil phase. This is because of the nanoparticles that create a strong protective layer around the oil droplets. It is even possible to remove the oil phase to obtain a micro/macroporous materials such as foams [99]. Therefore, Pickering emulsification has received a heavy recent attention as the facile approach in order to create novel nanocomposite materials.

1.6 Nanocelluloses as the stabilizer of Pickering emulsions

Recent studies have shown that the nanocelluloses are exceptionally effective in stabilizing O/W emulsions by irreversible adsorption at the oil-water interface [123–137]. These sub-micron-sized cellulose particles are preferred over micron-sized cellulose particles

such as MFC to stabilize Pickering emulsion [124]. The MFCs are bigger in size compared to the size of the droplets that produce aggregates instead of individual droplets. A major drive for the consideration of nanocelluloses in stabilizing emulsions includes their low toxicity and biocompatibility [125].

The surface properties and morphology of the nanocelluloses are particularly important in stabilizing the oil-water interface. Literally, the crystals of cellulose are not completely hydrophilic. Rather, their different crystal planes show varying affinity to water. Kalashnikova et al. studied the crystalline orientation of BC nanocrystals (cellulose Iα) and cotton CNCs (cellulose Iβ) at the oil-water interface [126]. They identified four crystallographic planes responsible for varying surface properties (Fig. 1.14). The two most broad crystal planes in terms of surface exposure contain hydroxyl groups that are responsible for the hydrophilic property, (1−10)β/(100)α and (110)β/(010)α. Another two planes are located at the corners of the cellulosic crystals and have a small surface exposure. One of which are hydrophobic (200)β/(1$\bar{1}$0)α plane with having C–H moieties, and another is hydrophilic (010)β/(110)α plane. Therefore, the reason for O/W interface stabilization can be assigned to their amphiphilic character arising from the existence of more hydrophilic and less hydrophobic characters at the surface of the CNCs [126,127]. The crystals adopt an orientation in which hydrophobic planes are directed towards the oil phase, and hydrophilic planes towards the water phase (Fig 1.14). Another advantage of CNCs as emulsion stabilizer comes from their rod-like shape and high aspect ratio that leads to higher adsorption energy [128,129].

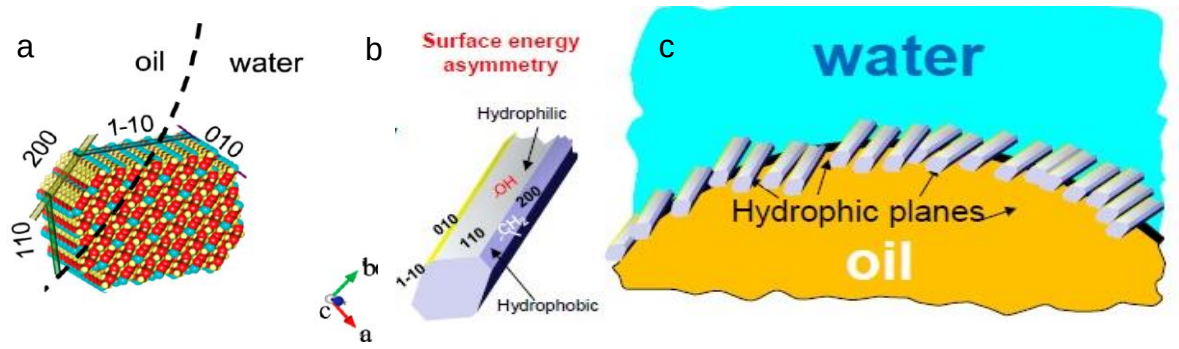

Figure 1.14. (a–c) Schematic representation of the CNCs (cellulose Iβ) at the O/W interface [126,136]. The hydrophobic plane (200) is oriented towards the oil phase. (a) Reproduced with permission from ref. 126 © 2012 American Chemical Society. (b,c) Artwork from Prof. Orlando J. Rojas, Aalto University, Finland [136].

Meanwhile, long thin CNFs with very high aspect ratio have also been studied as the Pickering emulsion stabilizer. Kalashnikova et al., in a different study, reported that the long high-aspect-ratio nanocelluloses (length: ~4 µm; aspect ratio: ~160) promote the formation of interconnected network in the emulsion (Fig. 1.15) [130]. The dense network in water traps and stabilizes the oil (hexadecane) droplets without coalescence. Winuprasith and Suphantharika fibrillated cellulose fibers by increasing number of passes through a high-pressure homogenizer; the more fibrillated fibers as happened with increasing number of passes promoted stronger three-dimensional network structures, and hence, more stable O/W emulsions with smaller soybean oil droplets [131]. Ougiya et al. compared the O/W emulsion stabilizing ability of BC nanofibers with MFC and MCC [124]. Since BC nanofibers consisted of thinner fibrils than MFC and MCC, they formed a strong network, and adsorbed on and covered a larger surface area on the oil (vegetable oil and kerosene) droplets to form a strong mechanical barrier. Thus, interrupted the coalescence of the oil droplets in order to stabilize the emulsion without reducing the interfacial tension. The emulsions stabilized by CNFs show excellent stability against fluctuations in ionic strength, pH and temperature, as oppose to the conventional emulsifying agents such as sorbitan monolaurate [124,132].

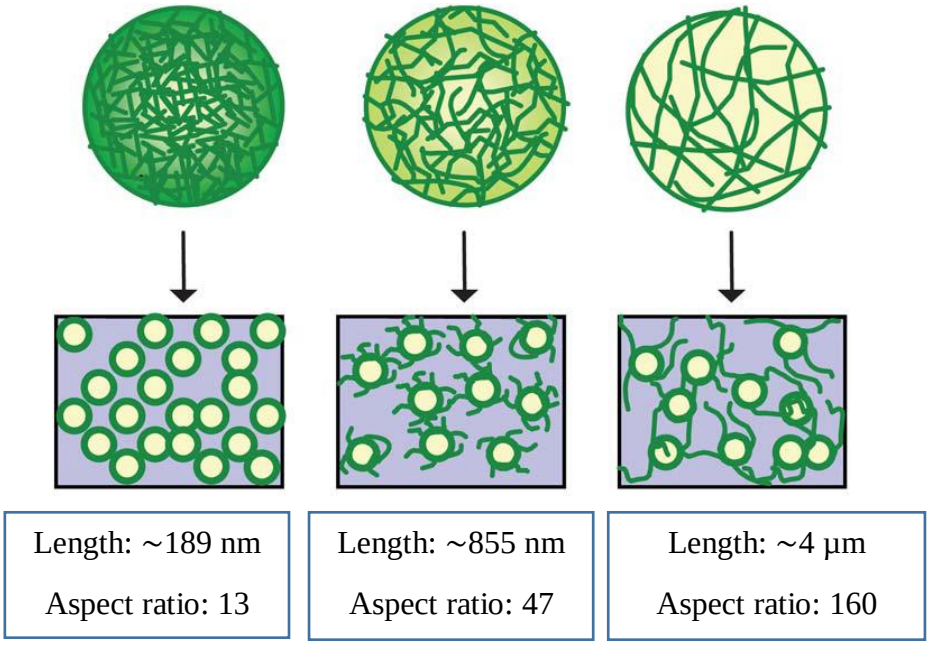

Figure 1.15. Schematic representation of the emulsions stabilized with nanocelluloses of various length and aspect ratio. The short nanocelluloses promote the formation of individual droplets, whereas, long thin nanofibrils promote an interconnected network system [130]. Adapted with permission from ref. 130 © 2013 The Royal Society of Chemistry.

Nanocelluloses have also been surface modified in order to bestow them more hydrophobic characteristic. These hydrophobized nanocelluloses have been used to form stable W/O emulsions. Xhanari el al. modified CNFs by silylation and proposed that the strong network forming ability of CNFs is the main factor to prevent coalescence of water droplets in toluene [133]. Lee et al. also proved the formation of a stable high-internal phase W/O emulsion (water-in-toluene) using modified BC nanofibers [134]. The BC nanofibers were hydrophobized by esterification with organic acids of various chain lengths, e.g., acetic (C2), hexanoic (C6), and dodecanoic (C12) acids. In another study, the surfaces of CNFs and CNCs were hydrophobically tailored with lauroyl chloride (C12) [135]. These nanocelluloses were able to stabilize W/O (water-in-hexadecane) emulsions. The combination of native and modified nanocelluloses led to the formation of O/W/O double emulsions where nanocelluloses were the sole stabilizer of the both interfaces. Furthermore, it was demonstrated that the long nanofibers lead to an increased stability of the emulsions.

Although, the long thin CNFs are also composed of crystals, having a semi-crystalline configuration (Fig. 1.2a), the orientation of their crystalline regions at the oil-water interface still remains elusive. However, most of the literatures emphasized on the strong network forming ability of these elongated nanocelluloses that effectively trap and stabilize the emulsion droplets without any coalescence (Fig. 1.15). The amount of CNFs required to stabilize a Pickering emulsion is less than that of the amount required for CNCs. For example, a completely stable emulsion (oil:water = 30:70) was obtained by using only 0.2% long thin nanocelluloses (aspect ratio 160), whereas, a stable emulsion was formed after using 0.5% CNCs (aspect ratio 13 or 47) [130]. Notably, the oil phase was consisted of hexadecane.

Therefore, it is conspicuous that the nanocelluloses are highly effective stabilizer of oil-water interfaces. The nanocelluloses are able to form a strong and non-leaking encapsulation shell around the oil or water droplets, thereby, produce highly stable O/W or W/O emulsions.

1.7 Objectives of the study

Nanocellulose-reinforced optically transparent nanocomposites have a unique combination of high strength and stiffness, incredibly low CTE, and high mechanical flexibility. However, fabrication of these nanocomposites by impregnation method restricts their 3D-molding due to the generation of strong H-bonding among the nanocelluloses in the nanopaper (Fig. 1.16). When a nanopaper of nanocelluloses is impregnated by a resin, the nanopaper still

remains intact inside the resulting nanocomposite (Fig. 1.16b). The nanocelluloses in the nanopaper (network) almost remain locked in position by the strong and recoverable H-bonds, and if the nanopaper is deformed, new positions of the nanocelluloses are locked in upon unloading [138-142]. This makes the nanopaper and its impregnated composite substantially stiff (low strain-to-failure), and hence, difficult to mold into a 3D-curved material. Therefore, many exciting applications of the nanocellulose-reinforced optically transparent and flexible materials, e.g., substrate for smart contact lenses and 3D-curved displays, microlens arrays, etc., could not be realized.

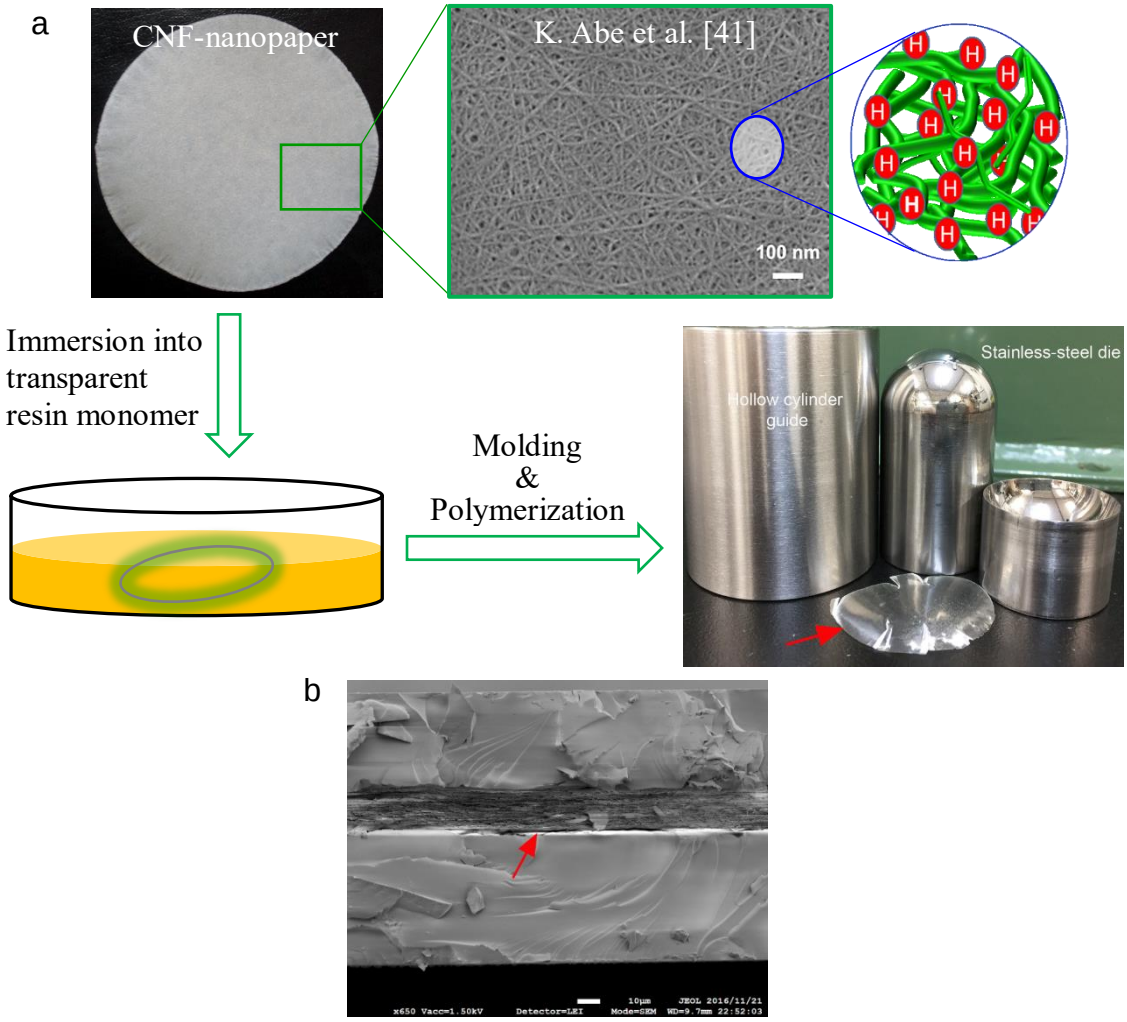

Figure 1.16. (a) The impregnation method to prepare transparent CNF-reinforced nanocomposite and its limitation to obtain a 3D-molded material. The scanning electron micrograph of CNFs is reproduced with permission from ref. 41 © 2007 American Chemical Society. (b) The fracture surface of an 'impregnated nanocomposite' showing a three-layer structure. The middle layer consists of an intact CNF-nanopaper, the nanopores of which are impregnated by the resin. The outer two layers are composed of the neat resin. The CNF-content of this nanocomposite was ~20 wt%.

To accomplish 3D-molding with optical transparency, the hypothetical key was to minimize H-bonding by mixing nanocelluloses with resin monomer in the water medium followed by evaporation of the water and polymerization of the monomer under compression in a 3D-shaped die. However, as mentioned earlier, hydrophilic "native" nanocelluloses that are usually suspended in water and hydrophobic resin (most commercial resins are hydrophobic) are typically immiscible, and hence, their homogeneous dispersion is difficult to achieve.

Therefore, the main objective of this study was to exploit the potential of the Pickering emulsification approach to directly and homogeneously disperse the native nanocelluloses into the hydrophobic resin monomer in a water medium (i.e., to form resin-in-water emulsion stabilized by nanocelluloses), hence to minimize H-boning among the nanocelluloses, in order to facilitate the fabrication of 3D-molded transparent nanocomposites. One hypothesis was that the encapsulated monomer micro-droplets in the nanocellulose-network will minimize the H-boding among the nanocelluloses even after dehydrating the emulsion. Another hypothesis was based on the consideration that the nanocelluloses can form a non-leaking encapsulation network around the monomer micro-droplets that can be collected on a filter membrane to obtain a monomer/nanocellulose film, which then easily can be 3D-molded in the macro- or micro-scale before polymerization.

Another objective was to explore the potential of the Pickering emulsification approach to generate self-assembled hierarchical structure in the transparent nanocomposites. Hierarchical structure is often found in nature materials, such as wood, crustacean shells (crab, shrimp etc.), nacre (mollusk shells) etc., which offers excellent structural and mechanical functionalities, e.g., rare combination of strength, stiffness, and toughness, but is usually absent in man-made composite materials. The hypothesis was that the resin micro-droplets that are individually encapsulated by the nanocellulose network will form another bulk network during their aggregation in a nanocomposite film, thereby, a two-tier hierarchical network of nanocelluloses will be formed. Based on this hypothesis, an important objective was to compare the structure, property, and their relationship in the nanocomposites prepared via Pickering emulsion method versus impregnation method.

Additional objective was to investigate the mechanical, thermal, and optical performances of the nanocomposites in relation to resin droplet diameter, nanocellulose content, and nanocellulose morphology and crystallinity (i.e., CNFs versus CNCs).

Finally, transparent conductive electrodes based on the nanocomposite substrate were prepared in an objective to demonstrate the potential application in the smart optoelectronic devices, and their performances compared to the electrodes prepared on the neat polymer film were investigated.

This study, therefore, provides significant insights to fabricate unique nanocomposites reinforced with nanocelluloses by using facile Pickering emulsification technique for the application in next-gen advanced optical materials.

1.8 References

1. Yano H., Sugiyama J., Nakagaito A. N., Nogi M., Matsuura T., Hikita M., and Handa K. Optically transparent composites reinforced with networks of bacterial nanofibers. Advanced Materials, 2005, **17**, 153–155.
2. Moon R. J., Martini A., Nairn J., Simonsen J., and Youngblood J. Cellulose nanomaterials review: structure, properties and nanocomposites. Chemical Society Reviews, 2011, **40**, 3941–3994.
3. Fernandes A. N., Thomas L. H., Altaner C. M., Callow P., Forsyth V. T., Apperley D. C., Kennedy C. J., and Jarvis M. C. Nanostructure of cellulose microfibrils in spruce wood. Proceedings of the National Academy of Sciences of the United States of America, 2011, **108**, E1195–E1203.
4. Isogai A., Saito T., and Fukuzumi H. TEMPO-oxidized cellulose nanofibers. Nanoscale, 2011, **3**, 71–85.
5. Wickholm K., Larsson P. T., and Iversen T. Assignment of non-crystalline forms in cellulose I by CP/MAS C-13 NMR spectroscopy. Carbohydrate Research, 1998, **312**, 123–129.
6. Kerr A. K., and Goring D. A. I. The ultrastructural arrangement of the wood cell wall. Cellulose Chemical Technology, 1975, **9**, 563–573.
7. Salmen L., and Olsson A. M. Interaction between hemicelluloses, lignin and cellulose: Structure-property relationships. Journal of Pulp and Paper Science, 1998, **24**, 99–103.
8. Stone J. E., and Scallan A. M. A study of cell wall structure by nitrogen absorption. Pulp and Paper Magazine of Canada, 1965, **66**, 407–414.
9. Thygesen A., Oddershede J., Lilholt H., Thomsen A. B., and Ståhl K. On the determination of crystallinity and cellulose content in plant fibres. Cellulose, 2005, **12**, 563–576.

10. Agustin M. B, Nakatsubo F., and Yano H. The thermal stability of nanocellulose and its acetates with different degree of polymerization. Cellulose, 2016, **23**, 451–464.
11. Nishino T., Takano K., and Nakamae K. Elastic modulus of the crystalline regions of cellulose polymorphs. Journal of Polymer Science Part B: Polymer Physics, 1995, **33**, 1647–1651.
12. Sturcova A., Davies G. R., and Eichhorn S. J. Elastic modulus and stress-transfer properties of tunicate cellulose whiskers. Biomacromolecules, 2005, **6**, 1055–1061.
13. Wohlert J., Bergenstrahle-Wohlert M., and Berglund L. A. Deformation of cellulose nanocrystals: entropy, internal energy and temperature dependence. Cellulose, 2012, **19**, 1821–1836.
14. Cintron M. S., Johnson G. P., and French A. D. Young's modulus calculations for cellulose Iβ by MM3 and quantum mechanics. Cellulose, 2011, **18**, 505–516.
15. Nishino T., Matsuda I., and Hirao K. All-cellulose composite. Macromolecules, 2004, **37**, 7683–7687.
16. Yano H. Japan a world leader in cellulose nanofiber: 'Green nanomaterial' seven times stronger than steel but 1/5 the weight. Japan Business Press Co. Ltd, 2014. http://jbpress.ismedia.jp/articles/-/41391. Accessed on July 1, 2016.
17. Nogi M., and Yano H. Transparent nanocomposites based on cellulose produced by bacteria offer potential innovation in the electronics device industry. Advanced Materials, 2008, **20**, 1849–1852.
18. Kawabata S., Sera M., Kotani T., Katsuma K., Niwa M., and Xiaoxin C. Anisotropic mechanical properties of advanced high performance fibers obtained by a single fiber testing system. In Composites Properties and Applications: Proceedings of the Ninth International Conference on Composite Materials (ICCM/9, Volume 6). Ed. A. Miravete, University of Zaragoza and Woodhead Publishing Ltd., Madrid, 1993, p. 671.
19. Callister W. D. Jr., and Rethwisch D. G. Materials science and engineering: An introduction (9th edition). Eds. W. D. Callister, Jr., and D. G. Rethwisch, John Wiley & Sons Inc., New York, 2013, pp. 881–900.
20. Yan J.–B., Liew J. Y. R., Zhang M.–H., and Wang J.–Y. Mechanical properties of normal strength mild steel and high strength steel S690 in low temperature relevant to arctic environment. Materials and Design, 2014, **61**, 150–159.
21. Hussain F., Hojjati M., Okamoto M., and Gorga R. E. Polymer-matrix nanocomposites, processing, manufacturing, and application: An overview. Journal of Composite Materials, 2006, **40**, 1511–1575.

22. Yu M. F., Lourie O., Dyer M. J., Moloni K., Kelly T. F., and Ruoff R. S. Strength and breaking mechanism of multiwalled carbon nanotubes under tensile load. Science, 2000, **287**, 637–640.
23. Salvetat P., Bhattacharyya S., and Pipes R. B. Progress on mechanics of carbon nanotubes and derived materials. Journal of Nanoscience and Nanotechnology, 2006, **6**, 1857–1882.
24. Ding W. Q., Calabri L., Chen X. Q., Kohhaas K. M., and Ruoff R. S. Mechanics of crystalline boron nanowires. Composite Science and Technology, 2006, **66**, 1112–1124.
25. Page D. H., and EL-Hosseny F. The mechanical properties of single wood pulp fibres. Part VI: Fibril angle and the shape of the stress-strain curve. Journal of Pulp and Paper Science, 1983, **9**, 99–100.
26. Saito T., Kuramae R., Wohlert J., Berglund L. A., and Isogai A. An ultrastrong nanofibrillar biomaterial: The strength of single cellulose nanofibrils revealed via sonication-induced fragmentation. Biomacromolecules, 2013, **14**, 248−253.
27. Tashiro K., and Kobayashi M. Theoretical evaluation of three-dimensional elastic constants of native and regenerated celluloses: Role of hydrogen bonds. Polymer, 1991, **32**, 1516–1526.
28. Eichhorn S. J., and Davies G. R. Modelling the crystalline deformation of native and regenerated cellulose. Cellulose, 2006, **13**, 291–307.
29. Mark R. E. Cell wall mechanics of tracheids. Yale University Press, New Haven, 1968, pp. 119,152.
30. Lahiji R. R., Xu X., Reifenberger R., Raman A., Rudie A., and Moon R. J. Atomic force microscopy characterization of cellulose nanocrystals. Langmuir, 2010, **26**, 4480–4488.
31. Hubbe M. A., Rojas O. J., Lucia L. A., and Sain M. Cellulosic nanocomposites: A review. BioResources, 2008, **3**, 929–980.
32. Alemdar A., and Sain M. Isolation and characterization of nanofibers from agricultural residues – wheat straw and soy hulls. Bioresource Technology, 2008, **99**, 1664–1671.
33. Heux L., Dinand E., and Vignon M. R. Structural aspects in ultrathin cellulose microfibrils followed by 13C CP-MAS NMR. Carbohydrate Polymers, 1999, **40**, 115–124.
34. Sugiyama J., Persson J., and Chanzy H. Combined infrared and electron diffraction study of the polymorphism of native celluloses. Macromolecules, 1991, **24**, 2461–2466.
35. Van den Berg O., Capadona J. R., and Weder C. Preparation of homogeneous dispersions of tunicate cellulose whiskers in organic solvents. Biomacromolecules, 2007, **8**, 1353–1357.

36. Hanley S. J., Revol J. F., Godbout L., and Gray D. G. Atomic force microscopy and transmission electron microscopy of cellulose from Micrasterias denticulata; evidence for a chiral helical microfibril twist. Cellulose, 1997, **4**, 209–220.
37. Iguchi M., Yamanaka S., and Budhiono A. Bacterial cellulose—a masterpiece of nature's arts. Journal of Materials Science, 2000, **35**, 261–270.
38. Jonas R., and Farah L. F. Production and application of microbial cellulose. Polymer Degradation and Stability, 1998, **59**, 101–106.
39. Yamanaka S., Watanabe K., Kitamura N., Iguchi M., Mitsuhashi S., Nishi Y., and Uryu M. The structure and mechanical properties of sheets prepared from bacterial cellulose. Journal of Materials Science, 1989, **24**, 3141–3145.
40. Wise L. E., Murphy M., and D'Addieco A. A. Chlorite holocellulose, its fractionation and bearing on summative wood analysis and on studies on the hemicelluloses. Paper Trade Journal, 1946, **122**, 35-43.
41. Abe K., Iwamoto S., and Yano H. Obtaining cellulose nanofibers with a uniform width of 15 nm from wood. Biomacromolecules, 2007, **8**, 3276-3278.
42. Zimmermann T., Bordeanu N., and Strub E. Properties of nanofibrillated cellulose from different raw materials and its reinforcement potential. Carbohydrate Polymer, 2010, **79**, 1086–1093.
43. Dufresne A., Cavaille J. Y., and Vignon M. R. Mechanical behavior of sheets prepared from sugar beet cellulose microfibrils. Journal of Applied Polymer Science, 1997, **64**, 1185–1194.
44. Stelte W., and Sanadi A. R. Preparation and characterization of cellulose nanofibers from two commercial hardwood and softwood pulps. Industrial & Engineering Chemistry Research, 2009, **48**, 11211–11219.
45. Sehaqui H., Zhou Q., Ikkala O., and Berglund L. A. Strong and tough cellulose nanopaper with high specific surface area and porosity. Biomacromolecules, 2011, **12**, 3638−3644.
46. Galland S., Andersson R. L., Salajková M., Ström V., Olsson R. T., and Berglund L. A. Cellulose nanofibers decorated with magnetic nanoparticles – synthesis, structure and use in magnetized high toughness membranes for a prototype loudspeaker. Journal of Materials Chemistry C, 2013, **1**, 7963 –7972.
47. Johnson R. K., Zink-Sharp A., Renneckar S. H., and Glasser W. G. A new bio-based nanocomposite: Fibrillated TEMPO-oxidized celluloses in hydroxypropylcellulose matrix. Cellulose, 2009, **16**, 227–238.

48. Wang S. Q., and Cheng Q. Z. A novel process to isolate fibrils from cellulose fibers by high-intensity ultrasonication, Part 1: Process optimization. Journal of Applied Polymer Science, 2009, **113**, 1270–1275.
49. Saito T., Kimura S., Nishiyama Y., and Isogai A. Cellulose nanofibers prepared by TEMPO-mediated oxidation of native cellulose. Biomacromolecules, 2007, **8**, 2485–2491.
50. Henriksson M., Henriksson G., Berglund L. A., and Lindstrom T. An environmentally friendly method for enzyme-assisted preparation of microfibrillated cellulose (MFC) nanofibers. European Polymer Journal, 2007, **43**, 3434–3441.
51. Klemm D., Kramer F., Moritz S., Lindstrom T., Ankerfors M., Gray D., and Dorris A. Nanocelluloses: A new family of nature-based materials. Angewandte Chemie-International Edition, 2011, **50**, 5438–5466.
52. de Oliveira F. B., Bras J., Pimenta M. T. B., da SilvaCurvelo A. A., and Belgacem M. N. Production of cellulose nanocrystals from sugarcane bagasse fibers and pith. Industrial Crops and Products, 2016, **93**, 48–57.
53. Wang B., and Sain M. Isolation of nanofibers from soybean source and their reinforcing capability on synthetic polymers. Composites Science and Technology, 2007, **67**, 2521–2527.
54. Montanari S., Rountani M., Heux L., and Vignon M. R. Topochemistry of carboxylated cellulose nanocrystals resulting from TEMPO-mediated oxidation. Macromolecules, 2005, **38**, 1665–1671.
55. Filson P. B., and Dawson-Andoh B. E. Sono-chemical preparation of cellulose nanocrystals from lignocellulose derived materials. Bioresource Technology, 2009, **100**, 2259–2264.
56. Lv D., Du H., Che X., Wu M., Zhang Y., Liu C., Nie S., Zhang X., and Li B. Tailored and integrated production of functional cellulose nanocrystals and cellulose nanofibrils via sustainable formic acid hydrolysis: Kinetic study and characterization. ACS Sustainable Chemistry and Engineering, 2019, **DOI: 10.1021/acssuschemeng.9b00714**.
57. Favier V., Canova G. R., Cavaillé J. Y., Chanzy H., Dufresne A., and Gauthier C. Nanocomposite materials from latex and cellulose whiskers. Polymers for Advanced Technologies, 1995, **6**, 351–355.
58. Favier V., Chanzy H., and Cavaillé J. Y. Polymer nanocomposites reinforced by cellulose whiskers. Macromolecules, 1995, **28**, 6365–6367.
59. Das P., Schipmann S., Malho J.–M., Zhu B., Klemradt U., and Walther A. Facile access to large-scale, self-assembled, nacre-inspired, high-performance materials with tunable nanoscale periodicities. ACS Applied Materials and Interfaces, 2013, **5**, 3738–3747.

60. Zhu W.–K., Cong H.–P., Yao H.–B., Mao L.–B., Asiri A. M., Alamry K. A., Marwani H. M., and Yu S.–H. Bioinspired, ultrastrong, highly biocompatible, and bioactive natural polymer/graphene oxide nanocomposite films. Small, 2015, **11**, 4298–4302.
61. Dzenis Y. Structural nanocomposites. Science, 2008, **319**, 419–420.
62. Martín Z., Jiménez I., Gómez M. Á., Ade H., and Kilcoyne D. A. Interfacial interactions in PP/MMT/SEBS nanocomposites. Macromolecules, 2010, **43**, 448–453.
63. Mathew A. P., Chakraborty A., Oksman K., and Sain, M. The structure and mechanical properties of cellulose nanocomposites prepared by twin screw extrusion (Chapter 9). In Cellulose nanocomposites: Processing, characterization, and properties (Vol. 938). Eds. K. Oksman, and M. Sain, American Chemical Society, Washington DC, 2006, pp. 114–131.
64. Oksman K., Aitomäki Y., Mathew A. P., Siqueira G., Zhou Q., Butylina S., Tanpichai S., Zhou X., and Hooshmand S. Review of the recent developments in cellulose nanocomposite processing. Composites Part A: Applied Science and Manufacturing, 2016, **83**, 2–18.
65. Lee K. -Y., Aitomaki Y., Berglund L. A., Oksman K., and Bismarck A. On the use of nanocellulose as reinforcement in polymer matrix composites. Composites Science and Technology, 2014, **105**, 15–27.
66. The Japan Plastics Industry Federation. Sales of plastics materials 2016–Japan. http://jpif.gr.jp/english/statistics/monthly/2016/2016_sales_materials_e.htm. Accessed on July 15, 2016.
67. Iwamoto S., Nakagaito A. N., Yano H., and Nogi, M. Optically transparent composites reinforced with plant fiber-based nanofibers. Applied Physics A: Materials Science and Processing, 2005, **81**, 1109–1112.
68. Capadona J. R., Van Den Berg O., Capadona L. A., Schroeter M., Rowan S. J., Tyler D. J., and Weder C. A versatile approach for the processing of polymer nanocomposites with self-assembled nanofibre templates. Nature Nanotechnology, 2007, **2**, 765–769.
69. Fall A. B., Lindstrom S. B., Sprakel J., and Wågberg L. A physical cross-linking process of cellulose nanofibril gels with shear-controlled fibril orientation. Soft Matter, 2013, **9**, 1852–1863.
70. Seferis J. C. Refractive indices of polymers, solid state properties (Chapter 6). In Polymer Handbook (4th edition). Eds. J. Brandrup. E. H. Immergut, and E. A. Grulke, Wiley, New York, 1999, p. 571.

71. Nogi M., Handa K., Nakagaito A. N., and Yano H. Optically transparent bionanofiber composites with low sensitivity to refractive index of the polymer matrix. Applied Physics Letters, 2005, **87**, 243110.
72. Nogi M., Ifuku S., Abe K., Handa K., Nakagaito A. N., and Yano H. Fiber-content dependency of the optical transparency and thermal expansion of bacterial nanofiber reinforced composites. Applied Physics Letters, 2006, **88**, 133124.
73. Ashby M. F. Materials selection in mechanical design. Pergamon Press, Oxford, 1993, pp. 44,121.
74. Okahisa Y., Yoshida A., Miyaguchi S., and Yano H. Optically transparent wood–cellulose nanocomposite as a base substrate for flexible organic light-emitting diode displays. Composites Science and Technology, 2009, **69**, 1958–1961.
75. Ummartyotin S., Juntaro J., Sain M., and Manuspiya H. Development of transparent bacterial cellulose nanocomposite film as substrate for flexible organic light emitting diode (OLED) display. Industrial Crops and Products, 2012, **35**, 92–97.
76. Leal-Calderon F., Schmitt V., and Bibette J. Emulsion Science: Basic Principles (2nd edition). Springer, New York, 2007, pp. 1–3,135,136.
77. Schramm L. L. Emulsions, foams, and suspensions: Fundamentals and applications. Wiley, New York, 2006, pp. 1–12,76,97,139,140,223–344.
78. Tadros, T. F., and Vincent, B. Liquid/liquid interfaces. In Encyclopedia of Emulsion Technology: Basic Theory (Volume 1). Ed. P. Becher, Marcel Dekker, New York, 1983, pp. 1–55.
79. Binks, B. P. Emulsions — Recent advances in understanding (Chapter 1). In Modern Aspects of Emulsion Science. Ed. B. P. Binks, The Royal Society of Chemistry Publication, Cambridge, 1998, pp. 1–48.
80. Tadros, T. F. Applied surfactants. Wiley-VCH, Weinheim, 2005.
81. Tadros T. F. Emulsion science and technology: A general introduction. In Emulsion Science and Technology. Ed. T. F. Tadros, Wiley-VCH, Weinheim, 2009, pp. 1–55.
82. Tadros T. F. Emulsion formation, stability, and rheology. In Emulsion Formation and Stability. Ed. T. F. Tadros, Wiley-VCH, Weinheim, 2013, pp. 1–73.
83. McClements D. J. Emulsion design to improve the delivery of functional lipophilic components. Annual Review of Food Science and Technology, 2010, **1**, 241–269.
84. Vincent B. Emulsions (Chapter 6). In Colloid Science: Principles, methods and applications (2nd edition). Ed. T. Cosgrove, Willey, UK, 2010, pp. 117–133.

85. Dickinson E. Double emulsions stabilized by food biopolymers. Food Biophysics, 2011, **6**, 1–11.
86. Adams L. L. A., Kodger T. E., Kim S. –H., Shum H. C., Franke T., and Weitz D. A. Single step emulsification for the generation of multi-component double emulsions. Soft Matter, 2012, **8**, 10719–10724.
87. Tadros T, Izquierdo R, Esquena J, and Solans C. Formation and stability of nano-emulsions. Advances in Colloid and Interface Science, 2004, **108–109**, 303–318.
88. Wooster T. J, Golding M., and Sanguansri P. Impact of oil type on nanoemulsion formation and Ostwald ripening stability. Langmuir, 2008, **24**, 12758–12765.
89. Mason T. G., Wilking J. N., Meleson K., Chang C. B., and Graves S. M. Nanoemulsions: formation, structure, and physical properties. Journal of Physics: Condensed Matter, 2006, **18**, R635–R666.
90. Ling, T. F., Lee, H. K., and Shah, D. O. Surfactants in enhanced oil recovery. In Industrial Applications of Surfactants. Ed. D. R. Karsa, The Royal Society of Chemistry, London, 1987, pp. 126–178.
91. Pontani L.–L., Haase M. F., Raczkowska I., and Brujic J. Immiscible lipids control the morphology of patchy emulsions. Soft Matter, 2013, **9**, 7150–7157.
92. Attwood D. Disperse systems (Chapter 6). In Pharmaceutics: The Science of Dosage Form Design. Ed. M. E. Aulton, Churchill-Livingstone, London, 2001, pp. 86–99.
93. Griffin W. C. Classification of surface-active agents by 'HLB'. Journal of the Society of Cosmetic Chemists, 1949, **1**, 311–326.
94. Griffin, W. C. Calculation of HLB values of non-ionic surfactants. Journal of the Society of Cosmetic Chemists, 1954, **5**, 249–256.
95. Davies J. T. A quantitative kinetic theory of emulsion type. I. Physical chemistry of the emulsifying agent. In Gas/Liquid and Liquid/Liquid Interfaces, Proceedings of the International Congress of Surface Activity, London, 1957, pp. 426–438.
96. Ramsden W. Separation of solids in the surface-layers of solutions and 'suspensions' (Observations on surface-membranes, bubbles, emulsions, and mechanical coagulation) – Preliminary account. Proceedings of the Royal Society of London, 1903, **72**, 156–164.
97. Pickering S. U. Emulsions. Journal of the Chemical Society, Transactions, 1907, **91**, 2001–2021.
98. Destribats M., Gineste S., Laurichesse E., Tanner H., Leal-Calderon F., Héroguez V., and Schmitt V. Pickering Emulsions: What are the main parameters determining the emulsion type and interfacial properties? Langmuir, 2014, **30**, 9313−9326.

99. Arditty S., Schmitt V., Giermanska-Kahn J, and Leal-Calderon F. Materials based on solid-stabilized emulsions. Journal of Colloid and Interface Science, 2004, **275**, 659–664.

100. Binks B. P. Particles as surfactants—similarities and differences. Current Opinion in Colloid and Interface Science, 2002, **7**, 21–41.

101. Leal-Calderon F., and Schmitt V. Solid-stabilized emulsions. Current Opinion in Colloid and Interface Science, 2008, **13**, 217–227.

102. Aveyard R., Binks B. P., and Clint J. H. Emulsions stabilised solely by colloidal particles. Advances in Colloid and Interface Science, 2003, **100 –102**, 503–546.

103. Chevalier Y., and Bolzinger M.–A. Emulsions stabilized with solid nanoparticles: Pickering emulsions. Colloids and Surfaces A: Physicochemical and Engineering Aspects, 2013, **439**, 23–34.

104. Levine S., and Sanford E. Stabilisation of emulsion droplets by fine powders. The Canadian Journal of Chemical Engineering, 1985, **63**, 258–268.

105. Abend S., and Lagaly G. Bentonites and double hydroxides as emulsifying agents. Clay Minerals, 2001, **36**, 557–570.

106. Ashby N. P., and Binks B. P. Pickering emulsions stabilised by laponite clay particles. Physical Chemistry Chemical Physics, 2000, **2**, 5640–5646.

107. Schlaepffer A. U. M. Water-in-oil emulsions. Journal of the Chemical Society, 1918, **113**, 522–526.

108. Moore W.C. Emulsification of water and of ammonium chloride solutions by means of lamp black. Journal of the American Chemical Society, 1919, **41**, 940–946.

109. Gelot A., Friesen W., and Hamza H. A. Emulsification of oil and water in the presence of finely divided solids and surface-active agents. Colloids and Surfaces, 1984, **12**, 271–303.

110. Binks B. P., and Lumsdon S. O. Pickering emulsions stabilized by monodisperse latex particles: Effects of particle size. Langmuir, 2001, **17**, 4540–4547.

111. Amalvy J. I., Unali G.–F., Li Y., Granger-Bevan S., Armes S. P., Binks B. P., Rodrigues J. A., and Whitby C. P. Synthesis of sterically stabilized polystyrene latex particles using cationic block copolymers and macromonomers and their application as stimulus-responsive particulate emulsifiers for oil-in-water emulsions. Langmuir, 2004, **20**, 4345–4354.

112. Qiao X., Zhou J., Binks B. P., Gong X., and Sun K. Magnetorheological behavior of Pickering emulsions stabilized by surface-modified Fe_3O_4 nanoparticles. Colloids and Surfaces A: Physicochemical and Engineering Aspects, 2012, **412**, 20–28.

113. Wang H., and Hobbie E. K. Amphiphobic carbon nanotubes as macroemulsion surfactants. Langmuir, 2003, **19**, 3091–3093.

114. Laredj-Bourezg F., Chevalier Y., Boyron O., and Bolzinger M.–A. Emulsions stabilized with solid organic particles. Colloids and Surfaces A: Physicochemical and Engineering Aspects, 2012, **413**, 252–259.

115. Fujii S., Aichi A., Muraoka M., Kishimoto N., Iwahori K., Nakamura Y., and Yamashita I. Ferritin as a bionano-particulate emulsifier. Journal of Colloid and Interface Science, 2009, **338**, 222–228.

116. van Rijn P., Mougin N. C., Franke D., Park H., and Böker A. Pickering emulsion templated soft capsules by self-assembling cross-linkable ferritin–polymer conjugates. Chemical Communications, 2011, **47**, 8376–8378.

117. Perrin E., Bizot H., Cathala B., and Capron I. Chitin nanocrystals for Pickering high internal phase emulsions. Biomacromolecules, 2014, **15**, 3766−3771.

118. Tzoumaki M. V, Moschakis T., Kiosseoglou V., and Biliaderis C. G. Oil-in-water emulsions stabilized by chitin nanocrystal particles. Food Hydrocolloids, 2011, **25**, 1521−1529.

119. Haaj S. B, Thielemans W., Magnin A., and Boufi S. Starch nanocrystal stabilized Pickering emulsion polymerization for nanocomposites with improved performance. ACS Applied Materials and Interfaces, 2014, **6**, 8263−8273.

120. Das A. K. Principles of fire safety engineering: Understanding fire and fire protection. PHI Learning Pvt. Ltd., New Delhi, 2014, p. 127.

121. Haaj S. B, Mabrouk A. B, Thielemans W., and Boufi S. A one-step miniemulsion polymerization route towards the synthesis of nanocrystal reinforced acrylic nanocomposites. Soft Matter, 2013, **9**, 1975–1984.

122. Shams M. I, and Yano H. Doubly curved nanofiber-reinforced optically transparent composites. Scientific Reports, 2015, **5**, 16421.

123. Capron I., and Cathala B. Surfactant-free high internal phase emulsions stabilized by cellulose nanocrystals. Biomacromolecules, 2013, **14**, 291–296.

124. Ougiya H., Watanabe K., Morinaga Y., and Yoshinaga F. Emulsion-stabilizing effect of bacterial cellulose. Bioscience, Biotechnology, and Biochemistry, 1997, **61**, 1541–1545.

125. Tingaut P., Zimmermann T., and Sèbe G. Cellulose nanocrystals and microfibrillated cellulose as building blocks for the design of hierarchical functional materials. Journal of Materials Chemistry, 2012, **22**, 20105–20111.

126. Kalashnikova I., Bizot H., Cathala B., and Capron I. Modulation of cellulose nanocrystals amphiphilic properties to stabilize oil/water interface. Biomacromolecules 2012, **13**, 267−275.

127. Kalashnikova I., Bizot H., Cathala B., and Capron I. New Pickering emulsions stabilized by bacterial cellulose nanocrystals. Langmuir, 2011, **27**, 7471–7479.

128. Alargova R. G., Warhadpande D. S., Paunov V. N., and Velev O. D. Foam superstabilization by polymer microrods. Langmuir, 2004, **20**, 10371–10374.

129. Madivala B., Vandebril S., Fransaer J., and Vermant J. Exploiting particle shape in solid stabilized emulsions. Soft Matter, 2009, **5**, 1717–1727.

130. Kalashnikova I., Bizot H., Bertoncini P., Cathala B., and Capron I. Cellulosic nanorods of various aspect ratios for oil in water Pickering emulsions. Soft Matter, 2013, **9**, 952–959.

131. Winuprasith T., and Suphantharika M. Microfibrillated cellulose from mangosteen (Garcinia mangostana L.) rind: Preparation, characterization, and evaluation as an emulsion stabilizer. Food Hydrocolloids, 2013, **32**, 383–394.

132. Salas C., Nypelö T., Rodriguez-Abreu C., Carrillo C., and Rojas O. J. Nanocellulose properties and applications in colloids and interfaces. Current Opinion in Colloid & Interface Science, 2014, **19**, 383–396.

133. Xhanari K., Syverud K., Chinga-Carrasco G., Paso K., and Stenius P. Structure of nanofibrillated cellulose layers at the O/W interface. Journal of Colloid and Interface Science, 2011, **356**, 58–62.

134. Lee K.–Y, Blaker J. J., Murakami R., Heng J. Y. Y., and Bismarck A. Phase behavior of medium and high internal phase water-in-oil emulsions stabilized solely by hydrophobized bacterial cellulose nanofibrils. Langmuir, 2014, **30**, 452–460.

135. Cunha A. G., Mougel J. –B., Cathala B., Berglund L. A., and Capron I. Preparation of double Pickering emulsions stabilized by chemically tailored nanocelluloses. Langmuir 2014, **30**, 9327−9335.

136. Rojas O. J. Nanocellulose in the formulation of emulsions and formulation-composition maps. TAPPI Webinar, April 14, 2016.

137. Bai L., Huan S., Xiang W., and Rojas O. J. Pickering emulsions by combining cellulose nanofibrils and nanocrystals: Phase behavior and depletion stabilization. Green Chemistry, 2018, **20**, 1571–1582.

138. Zhu H., Zhu S., Jia Z., Parvinian S., Li Y., Vaaland O., Hu L., and Li T. Anomalous scaling law of strength and toughness of cellulose nanopaper. Proceedings of the National Academy of Sciences of the United States of America, 2015, **112**, 8971–8976.

139. Altaner C. M., Thomas L. H., Fernandes A. N., and Jarvis M. C. How cellulose stretches: Synergism between covalent and hydrogen bonding. Biomacromolecules, 2014, **15**, 791–798.

140. Henriksson M., Berglund L. A., Isaksson P., Lindström T., and Nishino T. Cellulose nanopaper structures of high toughness. Biomacromolecules, 2008, **9**, 1579–1585.

141. Keckes J., Burgert I., Frühmann K., Müller M., Kölln K., Hamilton M., Burghammer M., Roth S. V., Stanzl-Tschegg S., and Fratzl P. Cell-wall recovery after irreversible deformation of wood. Nature Materials, 2003, **2**, 810–813.

142. Fellers C. The structure of paper and its modelling (Chapter 1). In Paper Products Physics and Technology. Eds. M. Ek, G. Gellerstedt, and G. Henriksson, Walter de Gruyter, Berlin 2009, p. 13.

Chapter 2
Development of Pickering Emulsification Method for Facile Fabrication of Transparent and 3D-molded CNF-Reinforced Nanocomposites

2.1 Introduction

Geared from the outstanding ability of nanocelluloses in stabilizing Pickering emulsions, recently, there has been a growing interest to create new composite materials by exploiting this advantage. For instance, Blaker et al. fabricated nanocomposite foams from the W/O Pickering emulsion solely stabilized by the hydrophobized BC nanofibers [1]. They first prepared water-in-soybean oil Pickering emulsion and then replaced the soybean oil by acrylated epoxidized soybean oil (AESO) monomers followed by ultraviolet (UV)-polymerization of the monomers and evaporation of water. The pore walls of the resulting foams were reinforced by the BC nanofibers. El-Mabrouk et al. prepared film-forming nanocomposite particles of poly(styrene-co-hexylacrylate) and polybutylmethacrylate latexes covered by CNCs from the CNC-stabilized Pickering emulsions containing styrene-ethylhexylacrylate and butylmethacrylate monomers in the oil phase, respectively [2,3]. The polymerized nanocomposite particles were then film-casted to prepare films with high mechanical strength. For example, at a content of 5 wt % CNCs, about 500% increment in the storage modulus of poly(styrene-co-hexylacrylate) above the glass transition was recorded. In a recent study, Li et al. demonstrated a thermal regulating nanocomposite that was prepared by encapsulating paraffin wax droplets in the TEMPO-oxidized-CNFs network from their O/W Pickering emulsion [4]. The paraffin wax is a phase change material (PCM) that solidifies upon cooling and liquefies upon heating, therefore, stores and releases heat in response to change in temperature. In an interesting study by Svagan et al., a photon energy upconversion nanopaper was prepared from an O/W Pickering emulsion of hexadecane oil containing photoactive sensitizer and emitter compounds using a mixture of CNFs and CNCs as the emulsion stabilizer that resulted in the formation of oil-core capsules, which were then embedded in the TEMPO-oxidized-CNFs film [5]. The nanopaper film could harvest the energy of the whole deep-red sunlight region. In another study, Nypelö et al. reported the fabrication of polystyrene-core and hollow microcapsules with CNC-

$CoFe_2O_4$ hybrid shells with magnetic functionality [6]. The hollow magnetic microcapsules were then used to separate methylene blue dye from water with the help of a magnet, which they considered as a model application for wastewater decontamination. Svagan et al. in a different study reported the formation of liquid-core microcapsules with strong CNF/CNC shells from the Pickering emulsion [7]. In this case, the CNFs and CNCs in the shells were cross-linked with isophorone diisocyanate (IPDI) forming a strong network structure. These liquid-core microcapsules might be useful in medical applications such as drug-delivery. Recently, Shams and Yano fabricated a novel double-curved chitin nanofiber-reinforced transparent composite via vacuum-filtration of the chitin nanofiber-stabilized resin-in-water Pickering emulsion [8].

Contemporary to this present study, Fujisawa et al. fabricated a transparent, strong, and thermally stable polystyrene/TEMPO-oxidized-CNFs nanocomposite from the styrene-in-water emulsion [9]. First, they prepared Pickering emulsion stabilized by TEMPO-oxidized-CNFs followed by polymerization of the styrene directly in the emulsion. The TEMPO-oxidized-CNFs-encapsulated polystyrene particles were then precipitated by adding methanol and HCl, collected on a filter membrane, and finally, hot-pressed to melt the polystyrene particles to form a nanocomposite film.

From the above description, it is conspicuous that the nanocelluloses are highly effective stabilizer of not only O/W or W/O Pickering emulsions, but also resin (monomer)-in-water or water-in-resin (monomer) Pickering emulsions. The nanocelluloses are able to form a strong and non-leaking encapsulation shell around the monomer resin droplets. Therefore, the Pickering emulsification method offers an easy water-based fabrication approach to obtain nanocellulose-based unique materials for advanced applications.

Hence, in the current study, in order to fabricate CNF-reinforced novel transparent composites such as a 3D-molded curved material or even a surface-micro-molded composite, the potential of the Pickering emulsification approach was explored by exploiting the dual role of the CNFs – stabilizer of the resin-in-water emulsion and reinforcing components of the resin. As the first step of the study, this chapter reports the detailed method of the Pickering emulsion preparation, the formulation of emulsions and its effect on the droplet morphology, emulsion viscosity and the stability, and thereby, on the properties of the resulting flat/planar nanocomposites. The advantage of the Pickering emulsification method in generating hierarchical structure in the nanocomposites and the corresponding high mechanical properties

compared to the nanocomposites prepared by impregnation method are discussed. Finally, the successful fabrication of transparent 3D-molded (in macro- and micro-scale) nanocomposites and the underlying reason thereof are presented.

2.2 Materials and method

2.2.1 Preparation of CNFs

CNFs were prepared from wood powder of *Chamaecyparis obtusa* (Japanese cypress, Hinoki) sieved through 60 mesh. Literally, the process reported by Abe et al. was followed [10]. First, the extractives were removed by toluene/ethanol (2:1) azeotrope extraction in a Soxhlet apparatus for 6 h. After that, the solvent-extracted wood powder was chemically purified to remove matrices (hemicelluloses and lignin) by following "Wise method" [11]. About 50 gm of extracted wood powder was dispersed in 1.5 L of distilled water and treated with acidified sodium chlorite ($NaClO_2$) at 80 °C for 4 h to remove lignin (20 gm $NaClO_2$ and 2 ml acetic acid were added in the reaction in each hour). The reacted powder was then washed thoroughly with distilled water followed by re-dispersing in distilled water to a total weight of 800 gm. Six (6) wt % potassium hydroxide (KOH) treatment was done at 90 °C for 2 h in order to leach hemicelluloses. The product was again thoroughly washed and treated with acidified $NaClO_2$ at 80 °C for 3 h to remove any residual lignin (20 gm $NaClO_2$ and 2 ml acetic acid were added in the reaction in each hour). After washing, a white purified wood powder dispersed in water was obtained that virtually contains pure cellulose. The α-cellulose content of the wood powder purified by this process can reach more than 85% [10]. The concentration of the purified wood powder slurry was adjusted to 0.8–1% and passed through a grinder (equipped with two grind-stones assembled in a rotor-stator configuration; see Figure 2.1) for two times to obtain water-dispersed "native" CNFs at ~0.5–0.7 wt% concentration. The grinding treatment was performed at 1,500 rpm with a clearance gauge of −2 (corresponding to a 0.2 mm shift) from the 0 position.

A sample from never-dried CNFs was subjected to oven-drying at 110 °C. The dried CNF sample was platinum coated in an ion sputter coater and imaged by a JEOL JSM-6700F field-emission scanning electron microscope (FE-SEM). X-Ray diffraction (XRD) analysis was also performed to determine the relative crystallinity of cellulose before and after grinding treatment. The CNFs suspension were freeze-dried and then pressed at 1.4 MPa to get pellets that were mounted on to the sample holder and irradiated with nickel-filtered CuKa (λ= 0.154 nm)

radiation generated by an UltraX 18HF X-Ray diffractometer (Rigaku Corporation, Tokyo, Japan) operating at 40 kV and 300 mA. The scattered radiation was detected in the angle range of 5°–40° using a goniometer that collected the data at a scan rate of 1° min^{-1} with an increment of 0.02° in the reflection mode. The crystallinity indices were determined from the normalized diffraction profiles using the method developed by Segal et al. [12].

Figure 2.1. Photographs of the grinder and stones (MKCA6-2, stone type: MKGC6-80, Masuko Sangyo, Japan) used to prepare CNFs.

2.2.2 Transparent resins

For most of the experiments (in the current and subsequent chapters), acrylic resin ABPE-10 (2.2-bis[4-(acryloxypolyethoxy)phenyl]propane; EO 10 mol) obtained from Shin-Nakamura Chemical Co. Ltd., was used. The chemical structure is given in Figure 2.2. It is a photo-curable transparent liquid monomer. The density, viscosity, refractive index, molecular weight (MW), and T_g of this resin are 1.14 g cm^{-3} (25 °C), 550 mPa.s (25 °C), 1.516 (25 °C), 776.89 g mol^{-1} and –12 °C, respectively. The surface tension (γ) is approximately 48 mN m^{-1}, measured at 25 °C by Drop-weight method (Equation 2.1) [13,14]. A photo-initiator, 2-hydroxy-2-methylpropiophenone, was mixed with ABPE-10 before use at a concentration of 0.25 wt% to polymerize the monomer under UV light (20 J cm^{-2}; F300S UV lamp/LC6 bench-top conveyer, Fusion UV Systems).

$$\text{Surface tension, } \gamma = \frac{mg}{2\pi r\left(\varphi \frac{r}{V^{\frac{1}{3}}}\right)} \qquad (2.1)$$

Where, m is the mass of a single drop of a liquid, g is acceleration due to gravity, r is the radius of the tip of the glass pipe through which the liquid drop was dripped, and $\varphi \frac{r}{V^{1/3}}$ is the empirical correction factor (V is the volume of one drop of the liquid). The value of the correction factor was estimated from the previous experimental results [15–18].

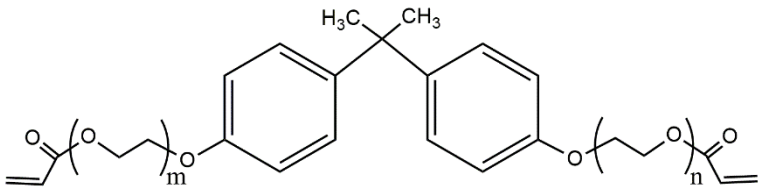

Figure 2.2. The chemical structure of ABPE-10, where m+n= 10; MW= 776.89 g mol^{-1}.

To verify the adaptability of the Pickering emulsification process to various resins in order to fabricate transparent nanocomposites reinforced with CNFs, a bis-phenol A-type epoxy resin (D.E.R.332) purchased from Sigma-Aldrich was also used. It is not only different in kind than the acrylic resin ABPE-10, but also a heat-curable transparent liquid monomer. HN5500 (Hitachi Chemical Company Ltd.) and 1,8-diazabicyclo[5.4.0]undec-7-ene (Sigma-Aldrich) were respectively used as a curing agent and catalyst. The curing agent (10.1 g) and catalyst (116 mg) were mixed with the epoxy resin (10 g) before use. The chemical structures of the epoxy resin, curing agent, and catalyst are shown in Figure 2.3.

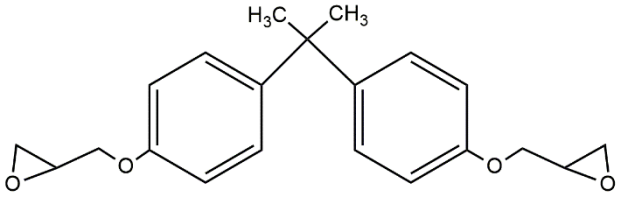

Epoxy resin D.E.R.332

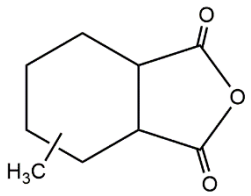

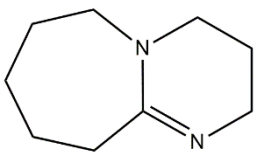

HN5500 1,8-diazabicyclo[5.4.0]undec-7-ene

Figure 2.3. The chemical structures of epoxy resin (MW= 340.41 g mol^{-1}), curing agent, and catalyst.

2.2.3 Preparation of Pickering emulsions

The acrylic resin-in-water Pickering emulsions were prepared by direct shearing of the mixture of CNFs/water-suspension and resin (Fig. 2.4). The shear force was given by a high-speed blender (Vita-Mix Absolute 3, Osaka Chemical Co. Ltd.). Pickering emulsions with several formulations were prepared. The amount of the CNFs to the resin was kept constant at 10 wt% (on dry-weight basis), but the formulation was changed by changing the water content. This was done to investigate the effect of the viscosity on the droplet formation, and hence, the effect on the properties of the nanocomposites containing identical CNFs content. The detailed formulations are given in Table 2.1. To obtain an emulsion, first, a CNF-suspension containing 0.5 gm CNF (on dry-weight basis) was poured into the blender. Acrylic resin of 4.5 gm was then added. Water content was adjusted to the desired formulation. An initial blending at 5000 rpm for 2 min was performed to disperse the resin as much as possible. After that, the speed of the blender was adjusted to 37000 rpm and blended for 15 min with a 5 min interval after 7.5 min. The interval allowed to reduce the temperature that reached about 80 °C during blending. The obtained emulsions were stored in dark to avoid any undesirable polymerization of acrylic resin droplets.

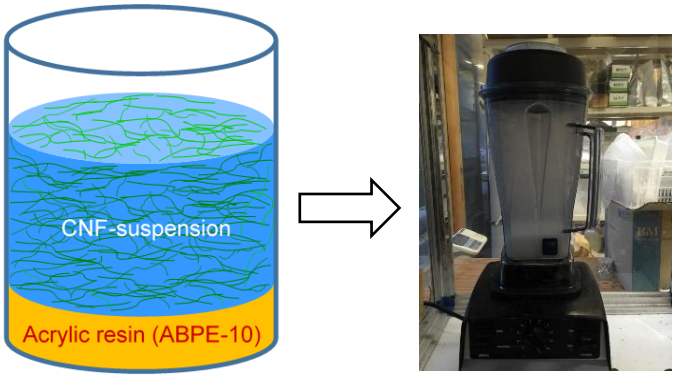

Figure 2.4. The resin-in-water Pickering emulsions were prepared by direct shearing of the mixture of acrylic resin and CNF-suspension using a high-speed blender.

2.2.4 Microscopic observation of the droplets

Emulsion samples were UV-cured immediately after preparation to keep the size and shape of the droplets intact. The cured emulsions were then dried over-night at 40 °C in an oven. A thin film was formed that was either cut by a sharp knife or cryo-fractured in liquid nitrogen to observe the droplets by a JEOL JSM-6700F or a JEOL JSM-7800F Prime FE-SEM after platinum coating. The diameter of the droplets was measured by an image processing

software (ImageJ) directly from the FE-SEM images. The diameter of about 200 droplets was measured.

Table 2.1. Formulations of the emulsions.

Nomenclature	CNF (dry weight) g	Acrylic resin g	Water g	CNF %	CNF to resin %
PE1	0.5	4.5	495	0.1	10
PE2			245	0.2	
PE3			161	0.3	
PE4			120	0.4	

* Note: The amount of CNFs and resin was kept same.

2.2.5 Viscosity measurement

The viscosity of the emulsions was measured at 25 °C by a viscometer (Visco Basic Plus R, Fungilab S. A.) according to ISO 2555 and ISO 1652 standards. The viscosity of the CNF-suspensions with concentrations from 0.1 wt% to 0.4 wt% was also measured.

2.2.6 Emulsion stability test

Samples of emulsions were taken into small glass bottles soon after the preparation and kept in a dark place. The photographic images were taken at a desired frequency of hours, days, and months. The stability of the emulsions were visually inspected to check any occurrence of the phase separation.

2.2.7 Fabrication of transparent nanocomposites from Pickering emulsion

The CNF-stabilized acrylic resin-in-water Pickering emulsions formulated by high-speed blending were subjected to vacuum-filtering to remove water in order to obtain a transparent nanocomposite. A PTFE filter-membrane (Advantec) with 0.1 µm pore-size was used. To keep the CNFs content identical, 45 gm, 22.5 gm, 15 gm, and 11.25 gm emulsions were taken for PE1, PE2, PE3, and PE4, respectively (please see Table 2.1 for emulsion formulations). The filtration time was about 8 h, 5 h, 3 h, and 2 h, respectively. After filtration, the wet CNF/resin nanocomposites (35 or 75 mm in diameter) were dried in an oven at 40 °C for 3 h to remove residual water. The nanocomposites contained 90 wt% liquid resin monomer, but were free-

standing. Unexpectedly, the nanocomposites were not optically transparent even after polymerization of the monomer. Therefore, these nanocomposites containing liquid monomer were termed as “CNF/resin mat”.

To obtain optically transparent nanocomposites, the mats were hot-pressed by placing between glass slides followed by polymerization using an UV light (Fusion UV Systems). The pressing temperature and pressure were 150 °C and 5 MPa, respectively. The hot-pressing time was 10 min plus an extra 5 min under a circulating cooling water (the cooling system was integrated with the hot-press). The moisture content of the composites was between 1 to 3%. The thickness of the composites was ~150−180 μm.

For fabricating 3D-molded transparent composites, a lens-shaped stainless steel die was used. First, the CNF/resin mat was placed on the female-part followed by placing the male-part on the top. A hollow cylinder was used as guide during hot-pressing (150 °C and 5 MPa). The picture of the die is shown in Figure 2.5. The composites were UV-cured immediately after hot-pressing.

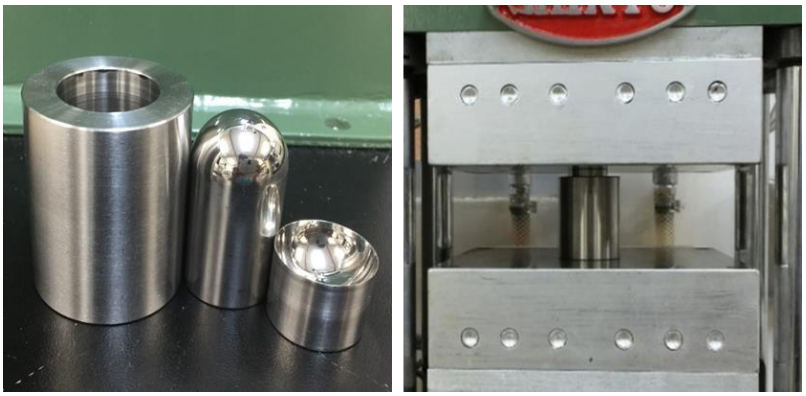

Figure 2.5. Photograph of stainless steel die for fabricating 3D-curved transparent nanocomposite (left). Photograph of the assembly of the die placed in a hot-press (right).

For surface micropatterned composites, a Patterned Sapphire Substrate (PSS) was used to copy the micro-pattern on the CNF/resin mat. The PSS was a kind gift from SAMCO Inc., Kyoto, Japan. Its surface is patterned with numerous lenses of about 2 μm in diameter (circular base) and 1.5 μm in height (Fig. 2.6). The mat was placed on the PSS and sandwiched with a glass slide, and then hot-pressed (150 °C and 5 MPa) followed by UV-curing. Given the PSS substrate consisted of convex lenses, the composites obtained were having concave micropatterns. Similarly, neat PMMA (poly(methyl methacrylate)) films with concave

micropatterns were prepared using the PSS, and subsequently used as the substrate for obtaining nanocomposites with convex micropatterns on the surface.

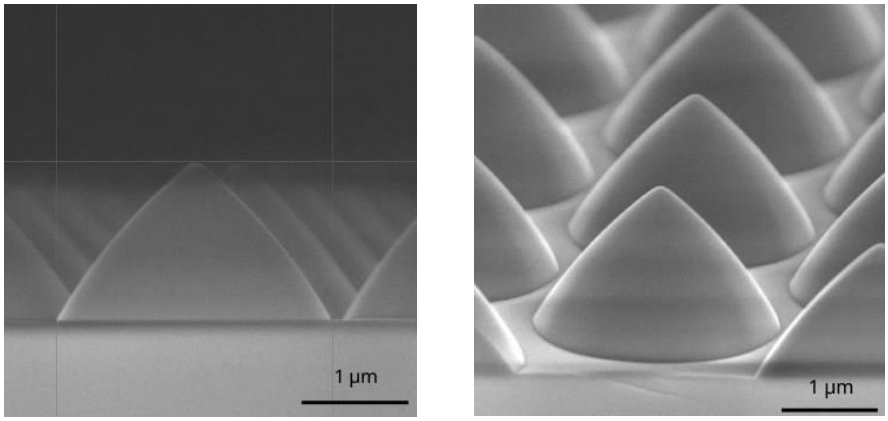

Figure 2.6. SEM images of the Patterned Sapphire Substrate (PSS) for in-situ micro-molding of the CNF/resin mat (SAMCO Inc., Kyoto, Japan).

2.2.8 Fabrication of transparent nanocomposites using impregnation method

The impregnation method was adapted from the work of Yano et al. and Iwamoto et al. [19,20]. The impregnated nanocomposite was fabricated to compare its properties with the nanocomposites prepared via Pickering emulsification method. First, the CNF-suspension was diluted with distilled water at a fiber content of 0.1 wt%, and then stirred for 3 h. Forty grams of the CNF-suspension was vacuum-filtered using a PTFE membrane with a 0.1-μm pore size to produce a wet thin sheet of 35 mm in diameter. The wet sheets were dried at 110 °C under 2 MPa pressure for 20 minutes to obtain a CNF-nanopaper of 38 μm thick. The CNF-nanopaper was immersed into the acrylic resin monomer under –0.1 MPa pressure for 6 hours. The resin impregnated CNF-nanopaper was then sandwiched between glass slides and finally cured by UV light. The thickness and CNF-content were ~120−140 μm and ~20%, respectively.

2.2.9 Electron microscopy imaging of the nanocomposites

FE-SEM imaging of the fracture surface of the nanocomposites was performed using a JSM-6700F or a JSM-7800F Prime (JEOL) after platinum coating. Transmission electron microscopy (TEM) observation was carried out using a JEM-1400 Plus (JEOL) after embedding the ultrathin nanocomposite samples in epoxy resin followed by staining with solid osmium tetroxide (OsO_4).

2.2.10 Measurement of light transmittances

Total and regular transmittances were measured in the wavelength range from 300 to 800 nm using an UV−vis spectrophotometer (U-4100, Hitachi) by placing the samples respectively at and 25 cm apart from the entrance port of the integrating sphere (60 mm in diameter).

The light transmittances were normalized to 100 μm thickness, because the thicknesses of the nanocomposites were varied depending on the hot-pressing conditions; the thickness have profound effect on the light transmittance of a material. The normalization was done according to the following equations:

$$T = \frac{I_T}{I_o} \tag{2.2}$$

$$I_T = I_o\,(1-R)^2\,e^{-\beta d} \tag{2.3}$$

$$R = \frac{(n_s-1)^2}{(n_s+1)^2} \tag{2.4}$$

Where, T = transmittance, I_T = incident light that have transmitted through a material, I_o = initial incident light, R = reflectivity/reflectance, β = linear absorption coefficient, d = thickness of the material (mm), and n_s = refractive index (RI) of the material.

n_s was calculated according to the Maxwell-Garnett Effective Medium Approximation equation [21]:

$$\frac{n_s-n_m}{n_s+2n_m} = \delta_i\left(\frac{n_i-n_m}{n_i+2n_m}\right) \tag{2.5}$$

Where, δ_i= fraction of inclusions (CNFs), n_i= refractive index (RI) of inclusions (RI of CNF is 1.544 in transverse direction [22]), n_m= RI of matrix (RI of ABPE-10 is 1.516).

2.2.11 Tensile test

The tensile test was carried out using an Instron 3365 universal testing machine (Instron) with a span length of 20 mm, at a crosshead speed of 1 mm min^{-1}. Stress−strain data were recorded for five rectangular nanocomposite specimens (5 mm × 35 mm). Prior to testing, the specimens were maintained in a controlled room at 23 °C and a relative humidity of 50% for 24–48 h.

2.2.12 Measurement of the thermal expansion

Thermal expansion properties were obtained using a thermomechanical analyzer TMA/SS 6100 (Seiko Instruments) in tensile mode with a 20 mm span and a ramp of 5 °C min^{-1} under a N_2 atmosphere. The measurements were run three times during elongation at a load of 3 g. The CTE values were determined in the temperature range of 20–150 °C in the second run.

2.2.13 Thermogravimetric Analysis (TGA)

TGA was carried out to determine the CNF-content of the nanocomposites using a TGA Q50 instrument (TA Instruments). TGA was performed from room temperature to 600 °C at a heating rate of 10 °C min^{-1}. Approximately 5–10 mg samples were used in the analyses. The samples were allowed to equilibrate at 110 °C for 20 min to remove moisture. The flow rate of nitrogen gas was maintained at 100 ml min^{-1} throughout the test.

2.2.14 Preparation of Pickering emulsion and transparent nanocomposites using epoxy resin

To verify the adaptability of the Pickering emulsification process to various resins in order to fabricate transparent nanocomposites reinforced with CNFs, the epoxy resin-in-water Pickering emulsion was also prepared by blending the mixture of CNFs/water-suspension and resin using a T25 digital ULTRA-TURRAX homogenizer (IKA). An ice-bath was used to keep the emulsion cool during the blending. The PE2 formulation was used (see Table 2.1). After filtering the emulsion, the resulting mat was oven-dried at 40 °C for 3 h and then pressed at 2–5 MPa and 50 °C for 5 min followed by increasing the temperature at 100 °C for 30 min. The nanocomposite was then removed from the hot-press and cured further in an oven at 110 °C for 2 h. The nanocomposite containing epoxy resin was only prepared to verify the potential of the Pickering emulsification method to adapt different transparent resins to obtain transparent CNF-reinforced nanocomposites.

2.3 Results and discussion

2.3.1 Characterization of CNFs

The CNFs were prepared by grinding treatment of lignin- and hemicelluloses-removed wood powder in a never-dried condition. After the grinding treatment, the obtained wood-

material became highly viscous and homogeneous colloidal-like dispersion, suggesting that comminution of original cellulose fibers occurred drastically with a high surface-to-volume ratio in water. Figure 2.7 shows the FE-SEM images of the oven-dried slurry of the CNFs with an average diameter of 23 ±8 nm. The length of the fibrils was >2 µm. However, the actual average length of the CNFs is difficult to measure, because they have very high aspect ratio and tend to entangle leaving almost no conspicuous ends. The CNFs have the similar morphology as fabricated by Abe et al. [10].

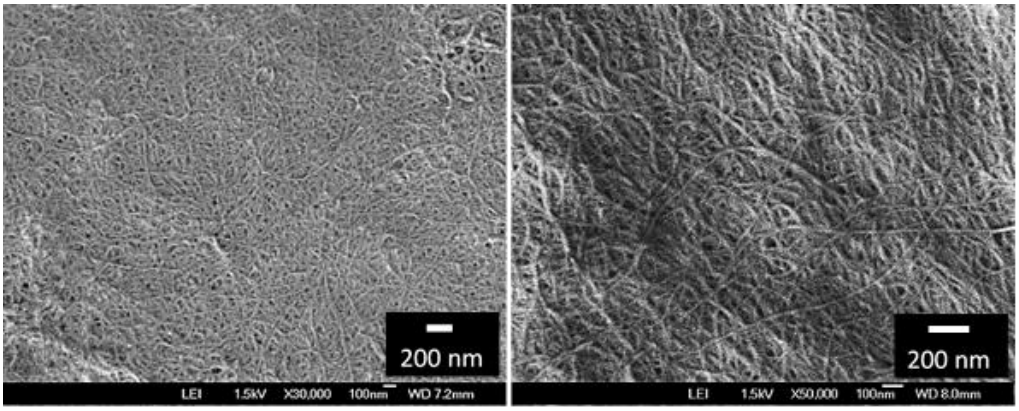

Figure 2.7. FE-SEM images of oven-dried CNFs under different magnifications (left: 30000x; right: 50000x).

The XRD patterns shown in Figure 2.8 suggest that the native cellulose-I crystal structure remained intact even after mechanical nanofibrillation. However, the crystallinity reduced to 64.2% (CNFs) from 81.4% (original fibers), which suggest that the intense mechanical comminution partially destroyed the crystalline aggregates of the cellulose fibrils. The findings from previous studies also support this result [23–25].

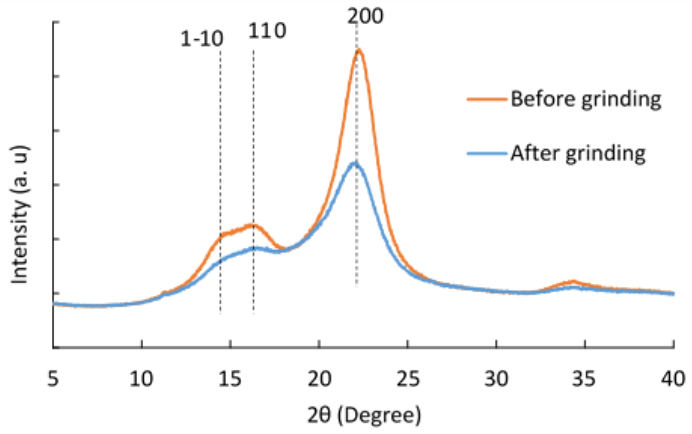

Figure 2.8. XRD patterns of purified wood powder before and after (CNFs) grinding treatment.

2.3.2 Formation of CNF-stabilized resin-in-water Pickering emulsions

The mixture of CNFs, acrylic monomer and water was mechanically sheared by a high-speed blender at 37000 rpm. After the intense blending, the mixture was turned into a homogeneous and milky colloidal-like dispersion (Fig. 2.9a). The blending treatment disintegrated the liquid acrylic monomer into numerous droplets of spherical shapes (Fig. 2.9c–f). The FE-SEM images of the UV-cured and oven-dried emulsion reveal that the droplets are covered by the dense network of CNFs (Fig. 2.9c–f). Kalashnikova et al. also reported a similar finding for hexadecane oil-in-water Pickering emulsion that was stabilized by the long, high aspect ratio nanocelluloses (length ~4 µm; aspect ratio ~160) (also see Fig. 1.15) [26]. The CNFs prepared in this study also have a high aspect ratio of about 100 with a length of >2 µm. The dense network of the long thin CNFs in the water trapped and encapsulated the resin droplets, thereby, effectively stabilized the emulsion with almost no coalescence of the droplets [27,26,28–32].

2.3.3 Effect of emulsion formulations on droplet size

The FE-SEM images shown in Figure 2.10a–d suggest that all of the emulsions prepared were polydispersed regardless of the formulations. With the increase in solid content (i.e., the percentage of CNFs plus resin in water), the diameter of the droplets and their polydispersity were increased (Fig. 2.10e,f). Although, the amount of CNFs and resin were kept constant in the formulations, but the difference in solid content was resulted from varying water content. A low solid content resulted in low viscosity of the emulsion (Fig. 2.10g), which probably produced a more uniform distribution of the shearing energy during blending. As a result, the emulsion with the PE1 formulation produced more uniform and smaller droplets compared to the emulsion with PE2 formulation, and similarly, PE2 formulation compared to PE3 formulation, and PE3 formulation compared to PE4 formulation (Table 2.2). The viscosity, thus droplet size and polydispersity of the emulsions, was found to be governed mainly by the concentration of the CNFs, because the viscosity of the emulsion was lower than that of the CNF/water suspension, both of which were having a same CNF content (Fig. 2.10g). This is probably due to the fact that the resin droplets in the emulsion provided low friction in the suspended CNFs network. The effect was minimum at diluted condition. The effect increased gradually with the increase in droplet size, probably because the bigger droplets helped sliding the network more effectively, thereby, profoundly reduced the viscosity of the emulsion.

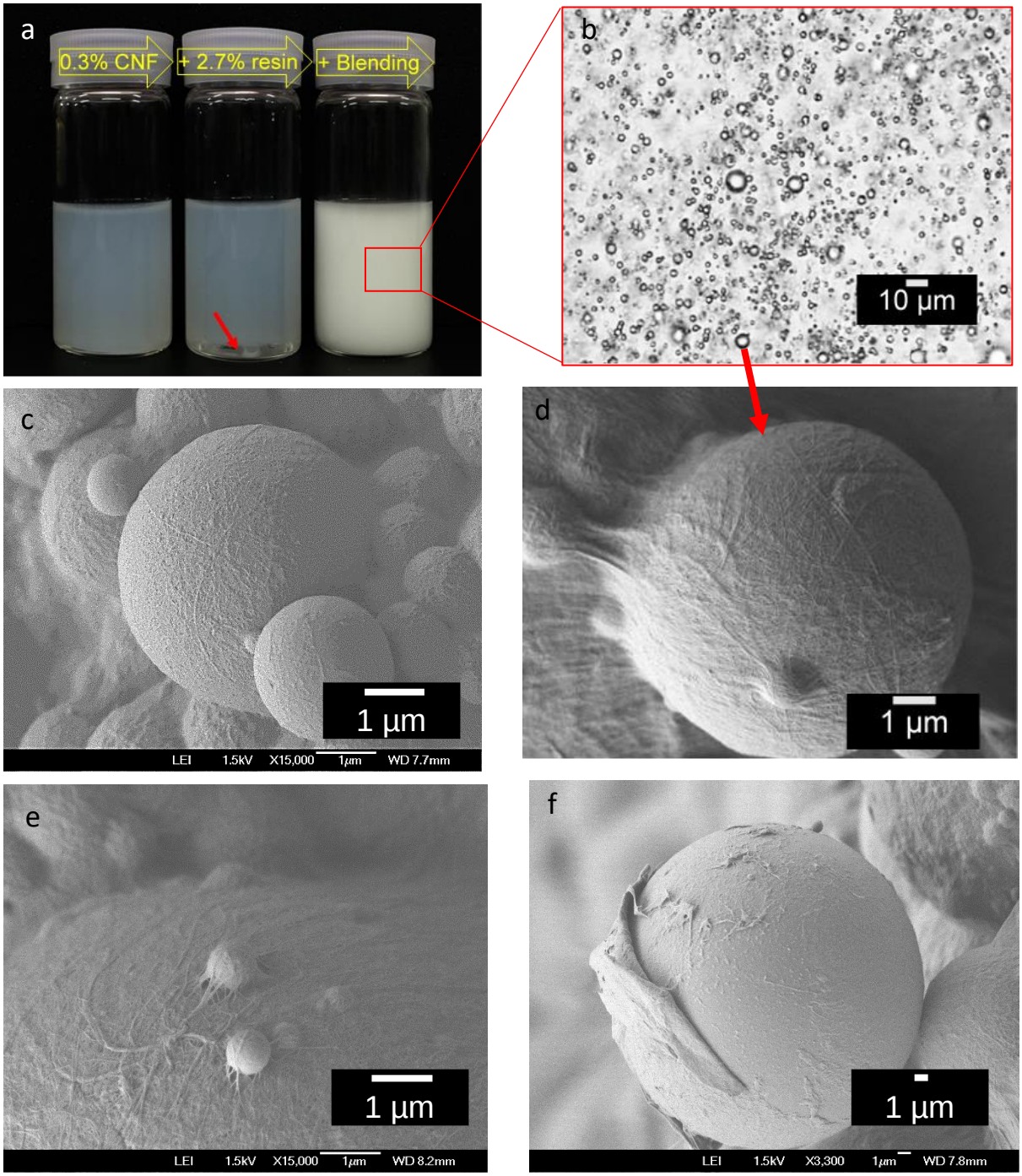

Figure 2.9. (a) Appearance of the emulsion produced after blending. (b) A digital microscopic image of the emulsion taken in situ. (c–f) FE-SEM images of the UV-cured followed by oven-dried emulsions at high magnifications. Image (f) shows that the CNF-shell around the resin droplet was torn apart during the sample preparation. All the images except (f) represent the emulsion of the formulation PE3. Image (f) represents PE4.

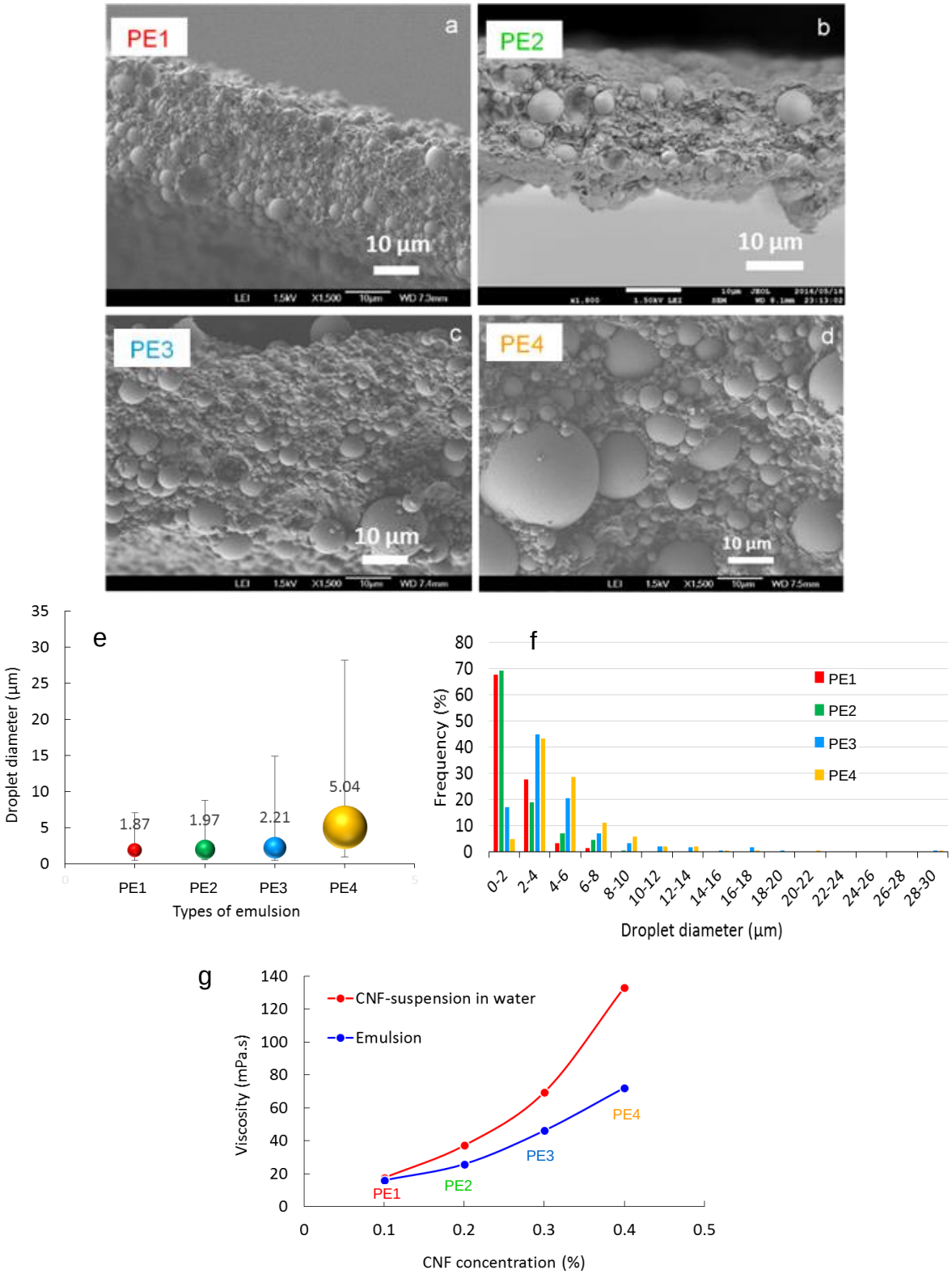

Figure 2.10. (a–d) FE-SEM images of the UV-cured followed by oven-dried emulsions of different formulations. (e) Effect of emulsion formulations on droplet diameter. The bar indicates the diameter of smallest and biggest droplet; the number indicates the average diameter of ~200 droplets. (f) Frequency distribution of the diameter of the droplets. (g) Effect of formulations on the emulsion viscosity.

Table 2.2. The average, maximum, and minimum diameter of the droplets, and the corresponding viscosity of the emulsions.

Emulsion type	Average diameter (µm)	Maximum (µm)	Minimum (µm)	Viscosity (mPa.s)/25 °C
PE1	1.87	7.07	0.51	16.1
PE2	1.97	8.74	0.51	25.9
PE3	2.21	14.88	0.51	46.2
PE4	5.04	28.22	0.98	72.2

The result obtained for the effect of emulsion formulations on the droplet size is in disagreement with the previous studies. Carrillo et al. reported the formation of smaller soybean oil droplets in water with an increment in CNFs concentration because of the formation of a more connected CNFs network and the corresponding higher viscosity [33]. The authors explained that the denser CNFs network would effectively restrict the coalescence of the oil droplets (i.e., higher stability), and thus would produce smaller droplets. In another study, also, a sharp decrease in the droplet size of the hexadecane oil with the increasing concentration of nanocelluloses was observed [26]. Literally, the droplet size of the emulsion may vary depending on the type of the oil (viscosity, surface tension etc.) [33], emulsification condition (temperature, conductivity, energy etc.), and equipment (homogenizer, ultrasonic, blender etc.) used. However, in this study, those variables were paid less attention, because the main focuses were to develop a transparent nanocomposite with 3D-moldability, to investigate the effect of the microstructure, nanocellulose content and nanocellulose length on the mechanical, optical and thermal properties of the nanocomposites, and to investigate the suitability of the nanocomposite as the substrate for smart optoelectronic devices.

2.3.4 Emulsion stability

Figure 2.11 shows the photographic images of the emulsions taken immediately after their preparation (0 day), and after 1 day, 7 days, and 15 days. PE1 with the diluted formulation clearly showed a phase separation after 7 days. The emulsion PE2 showed a trace of phase separation after 15 days. Emulsions with higher viscosity, i.e., PE3 and PE4, showed no trace of phase separation even after 15 days. In fact, PE3 and PE4 were stable over several months. Figure 2.12 shows the FE-SEM images of the UV-cured followed by oven-dried PE3 emulsion

obtained immediately after its preparation and after 3 months. An increase in the droplet size can be observed, though no phase separation was detected in the stability test. The increased stability of the emulsion was due to the higher CNFs concentration in the water phase that formed a dense and intensely connected network, which effectively reduced the coalescence of the resin droplets [33].

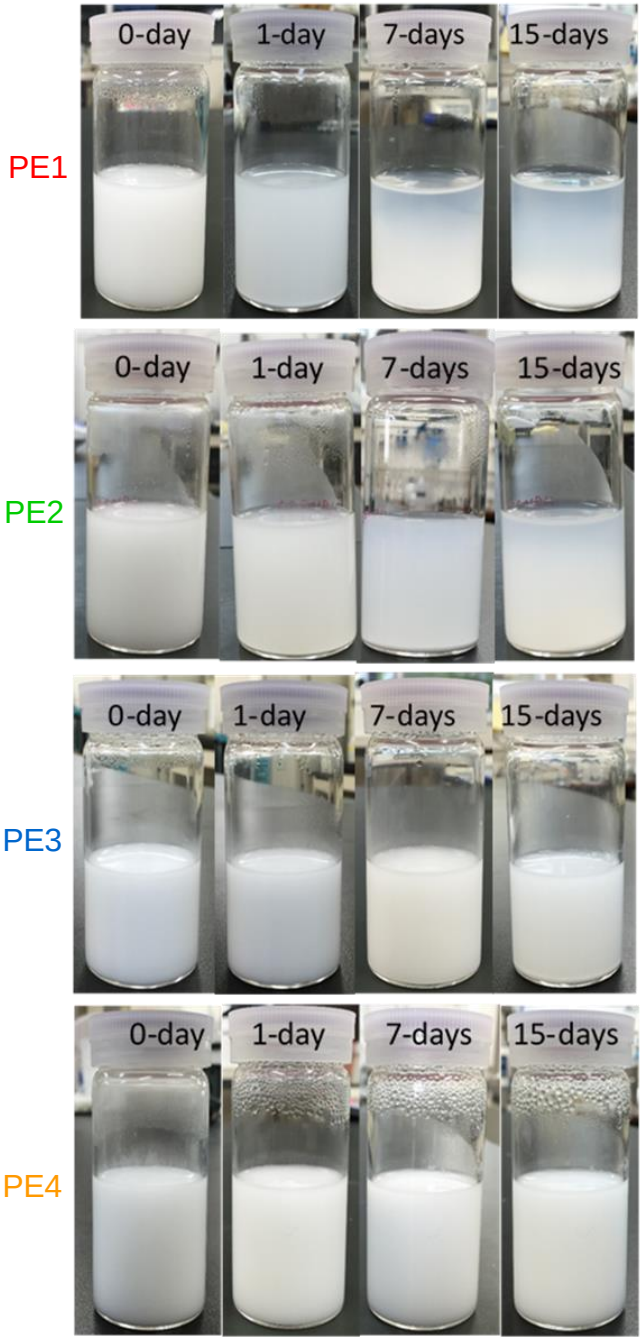

Figure 2.11. Photographic images of the CNF-stabilized resin-in-water Pickering emulsions taken immediately after their preparation (0 day), and subsequently after 1 day, 7 days, and 15 days.

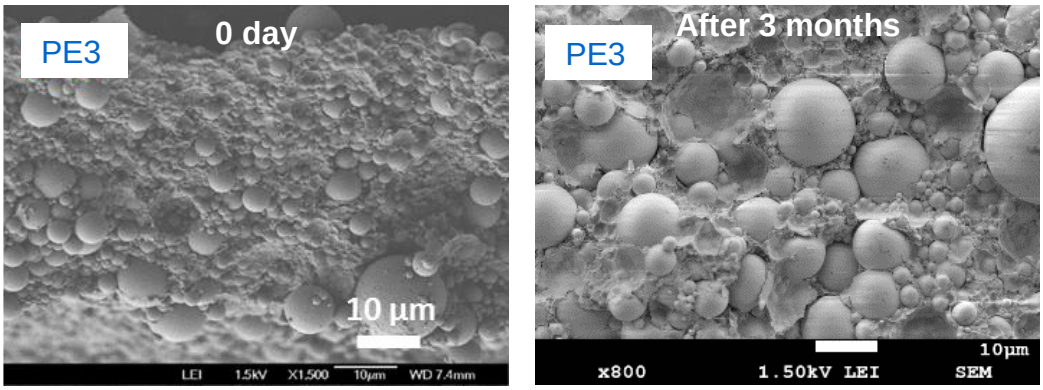

Figure 2.12. FE-SEM images of the UV-cured followed by oven-dried PE3 emulsion obtained immediately after preparation (left) and after 3 months (right).

2.3.5 Optically transparent nanocomposites from Pickering emulsion

The CNF-stabilized acrylic resin-in-water Pickering emulsions were dehydrated by vacuum-filtration. Surprisingly, no apparent resin loss through the filter membrane was observed. This is because the liquid resin droplets were encapsulated by and trapped into the intense CNF-network. Figure 2.13 shows the effect of the droplet size on the appearance of the CNF/resin nanocomposite mats that contained liquid monomer. The mat obtained from PE1 having smallest droplets was translucent and the surface was comparatively smooth. As the droplet size increased from PE2 to PE4, the mat became increasingly opaque and the surface smoothness decreased gradually. Most interestingly, even after vacuum-filtration, the liquid resin droplets did not merge or coalesce together as evident from the microstructure of the mats (Fig. 2.14). This is an evidence that the liquid droplets were strongly encapsulated by the CNFs network. However, the droplets were deformed into oval shapes from their original spherical shape due to the suction pressure during vacuum-filtration. The deformed droplets were still covered by the CNF-network in the mat as can be seen in Figure 2.14c. The thickness of the CNF-network around the resin droplets was not uniform, rather ranged between ~100 nm to ~500 nm.

The CNF/resin mats were not optically transparent even after UV polymerization and a high proportion of transparent resin (~90 wt %). The opaqueness was probably due to the light scattering from the uncompact interfaces among the CNF-covered droplets as indicated by the FE-SEM images of the fracture surface of the mat (Fig. 2.14). Therefore, the non-polymerized CNF/resin mat was sandwiched between glass slides and hot-pressed at 150 °C and 5 MPa foll-

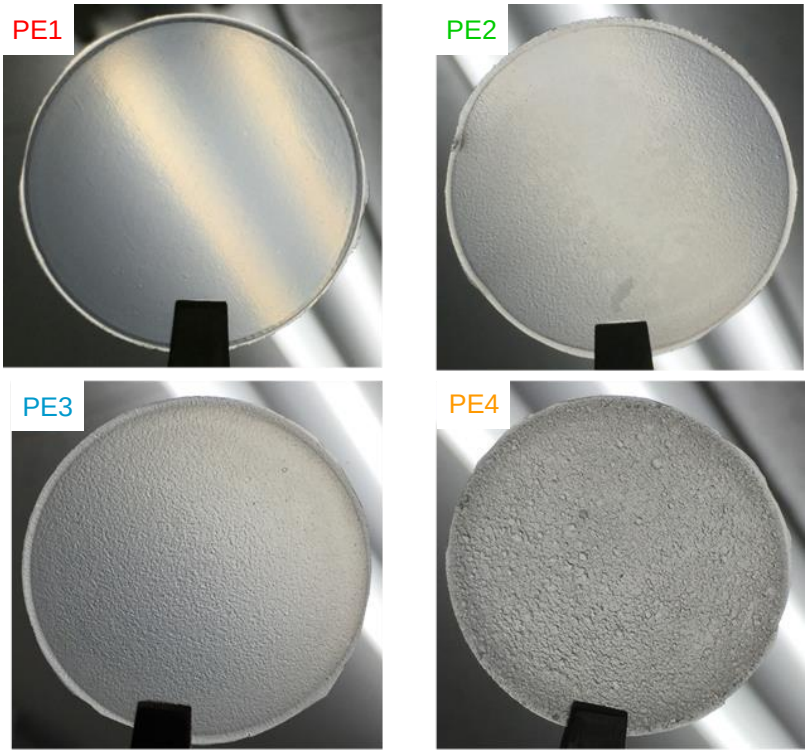

Figure 2.13. Photographic images of the self-standing CNF/resin nanocomposite mats obtained after filtration followed by oven-drying (40 °C) of the Pickering emulsions. All of the mats contain 90 wt% liquid acrylic monomer. The photographs also indicate the effect of the droplet size on the appearance of the mat.

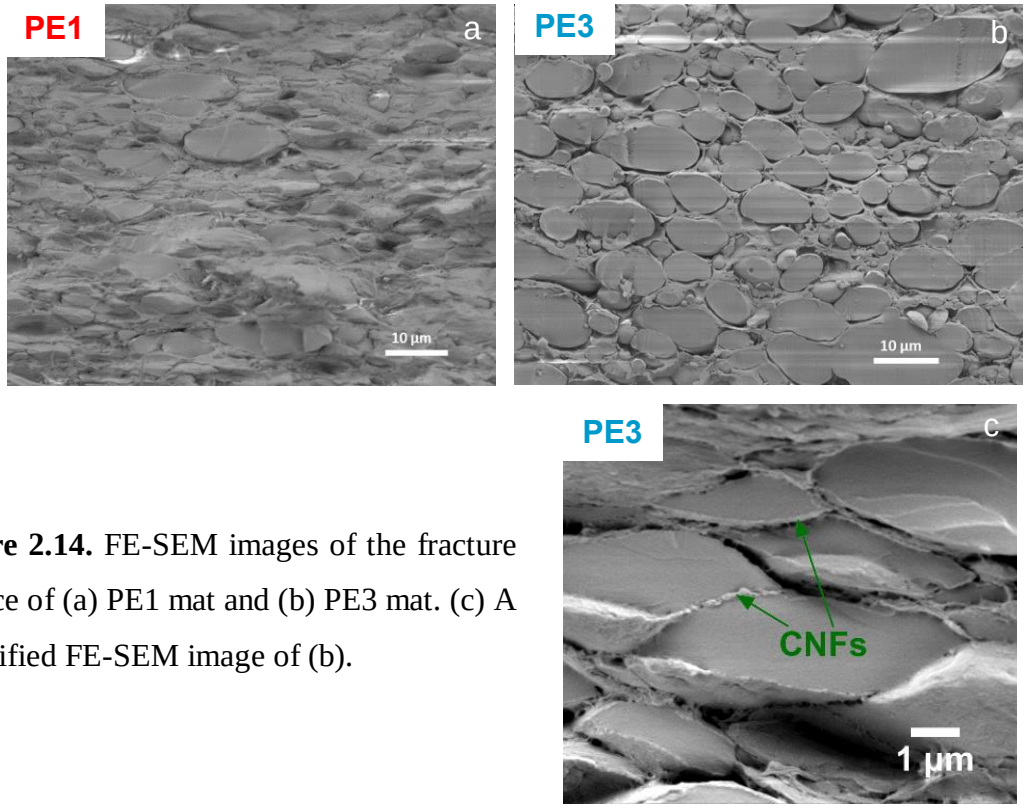

Figure 2.14. FE-SEM images of the fracture surface of (a) PE1 mat and (b) PE3 mat. (c) A magnified FE-SEM image of (b).

owed by UV polymerization. Eventually, a highly transparent nanocomposite (termed as PE nanocomposite) with a much more compact structure was obtained (Fig. 2.15a–d). The regular and total transmittances of the PE nanocomposites were 82–85% and 89% at 600 nm, respectively (Fig. 2.15e,f). For comparison, impregnated (IM) composites with the same resin and a CNF content of ~20 wt % were also prepared [19,20]. Notably, the CNF content of the transparent PE nanocomposites prepared from Pickering emulsions was increased to ~16 wt % because ~7 wt % of resin was squeezed out during hot-pressing. The optical transparency was similar to or even higher than that of the IM composites prepared in this study and in the literature [34]. The addition of CNFs reduced the regular transmittance of the acrylic resin by only 6–9%, whereas the reduction in total transmittance was only 3%.

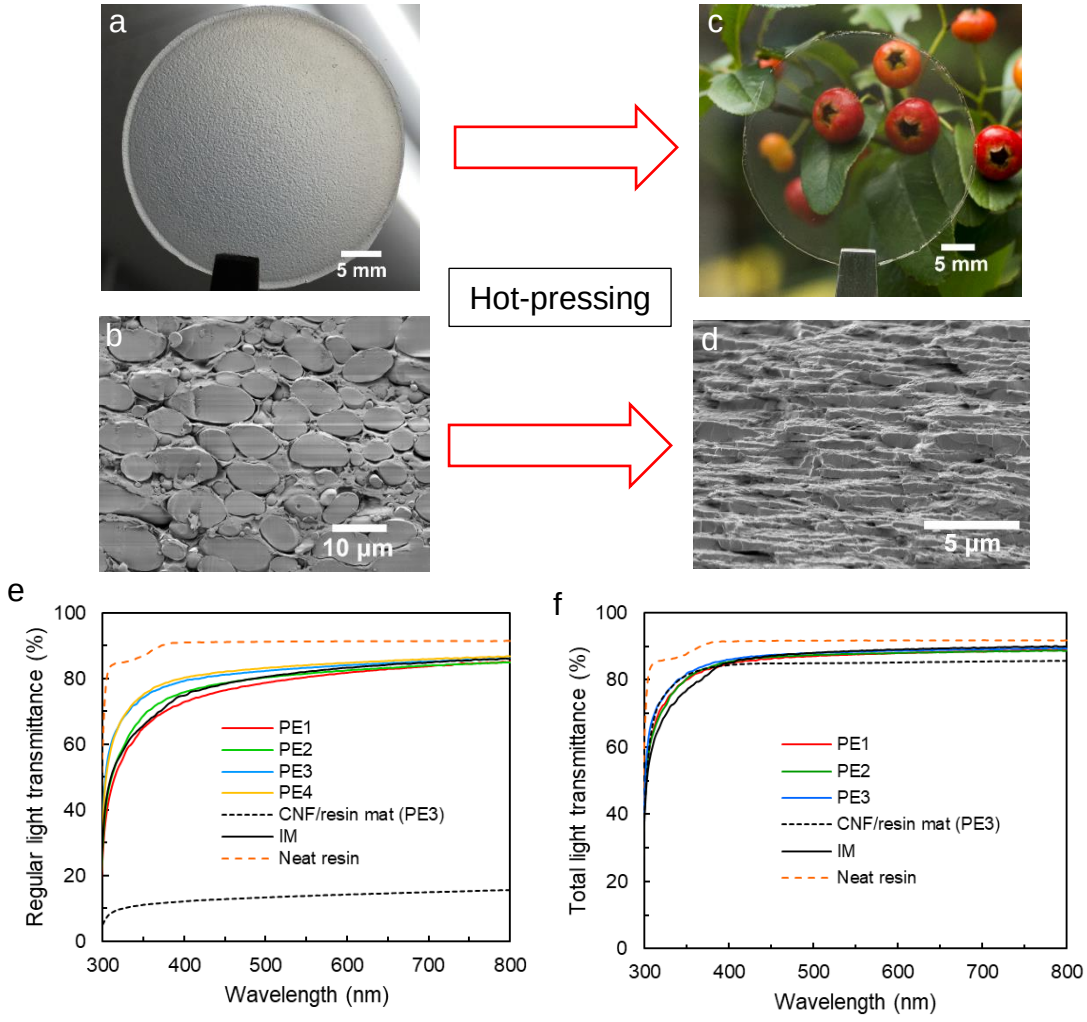

Figure 2.15. (a) Photograph of the PE3 mat. (b) FE-SEM image of the fracture surface of the PE3 mat. (c) Photograph of the transparent nanocomposite obtained after hot-pressing of the PE3 mat. (d) FE-SEM image of the fracture surface of the PE3 nanocomposite. (e) Regular light transmittances, and (f) total light transmittances of the nanocomposites. "IM" refers to the impregnated nanocomposite prepared by the impregnation method.

A gradual attenuation of the regular transmittance from PE3 to PE1 nanocomposite can be observed in Figure 2.15e. For example, the PE4 nanocomposite transmitted 85% light (at 600 nm) compared with 82% for PE1. This might be because the PE1 emulsion contained relatively uniform and smaller resin droplets, which led to a higher number of CNF/resin interfaces and thus higher light scattering even at a similar CNF content. The CNF/resin mat was opaque, with only 14% (600 nm) regular transmittance (Fig. 2.13 and Fig. 2.15e), but with a total transmittance of 85% (600 nm) (Fig. 2.15f). It can be proposed that this large amount of light scattering was eliminated by (1) hot-pressing, which made the CNF/resin interfaces more compact, and (2) better flowability of the resin monomer at the hot-pressing temperature, which penetrated into the CNF network and formed a continuous matrix, and therefore, the minute variation in the RI between the CNF and acrylic resin was minimized. Of note, the high optical transparency also indicates a good dispersion of the CNFs throughout the PE nanocomposites obtained via the Pickering emulsification method [35,36].

To verify the suitability of the Pickering emulsification process to adapt various resins in order to fabricate transparent nanocomposites reinforced with CNFs, transparent epoxy resin was also used instead of the acrylic resin to form an epoxy resin-in-water Pickering emulsion using the PE2 formulation. The CNF/resin mat and the corresponding transparent PE nanocomposite obtained after compression and polymerization are shown in Figure 2.16. The result indicates that a transparent nanocomposite can also be fabricated using the epoxy resin via the Pickering emulsification approach. Therefore, Pickering emulsification approach offers a facile water-based route to obtain transparent nanocomposites of various resins that are immiscible with native unmodified CNFs.

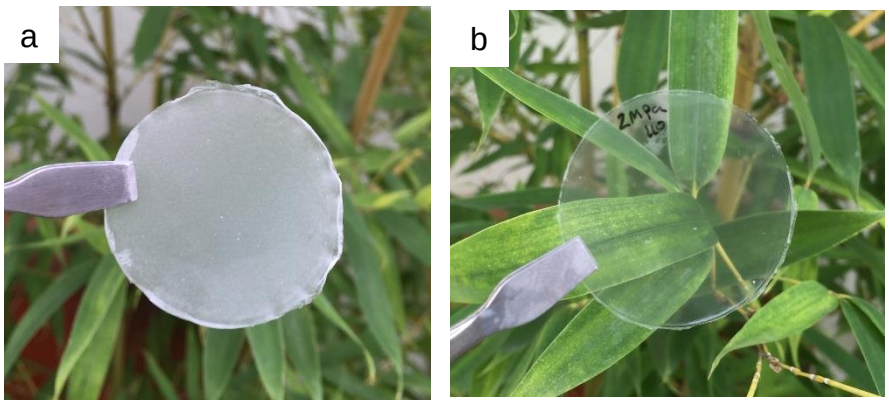

Figure 2.16. (a) Photograph of the CNF/epoxy resin mat. (b) Photograph of the transparent PE nanocomposite of epoxy resin and CNFs with ~14 wt% CNF content.

2.3.6 Hierarchical microstructure of the nanocomposites

Hierarchical structural design of materials provides an opportunity for synergistic tailoring of the materials properties [37]. Man-made composite materials usually lack hierarchical structure, but nature exploits this concept very effectively to create composite materials with superior functionalities composed of inferior components [37−41]. For example, nacre, the mollusks shell, is composed of hard but brittle aragonite platelets as the major component (95%) surrounded by a soft biopolymer matrix as the minor component (5%) (Fig. 2.17) [39−42]. Despite this composition, it displays an anomalous combination of incredible strength and toughness, thanks to its highly synergistic load-bearing, stress-dissipating, and crack-deflecting mechanism effected by the hierarchical "brick-and-mortar" structure [39−44].

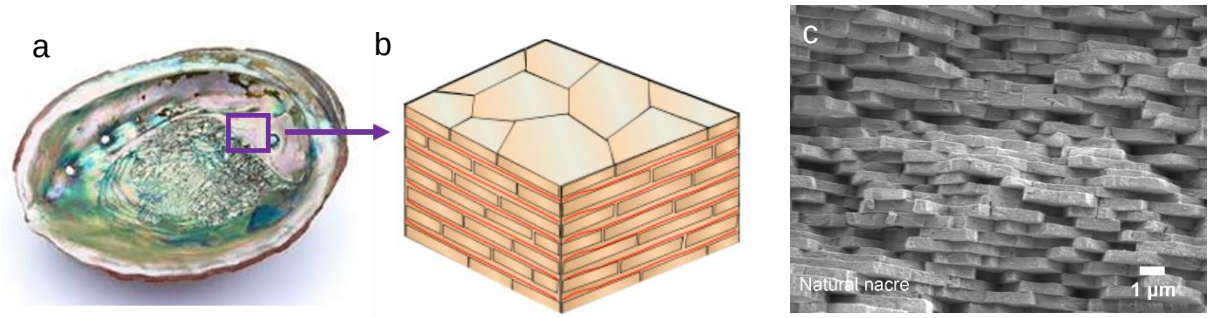

Figure 2.17. (a,b) The nacre has alternating "brick and mortar" arrangement of hard aragonite platelets (light orange color) and soft biopolymer layers (red lines) [45]. Reproduced with permission from ref. 45 © 2010 American Chemical Society. (c) FE-SEM image of the fracture surface of a nacre.

In this study, it was hypothesized that the aggregation of resin droplets that are encapsulated by a thin network of CNFs would generate a bulk network by interconnecting the droplets in the nanocomposite. Thereby, a self-assembled two-tier hierarchical structure would be generated. Therefore, the microstructure of the transparent PE nanocomposites was studied from the TEM images as shown in Figure 2.18. It was in fact found that the droplets were interconnected by a bulk micro-scale network throughout the nanocomposite. Hence, the PE nanocomposites produced by the Pickering emulsion process were hierarchical in structure. A graphical illustration to explain this phenomenon is presented in Figure 2.19. When the CNF/resin mat was hot-pressed at high temperature and pressure, the liquid resin droplets only could deform laterally because of the strong encapsulation from the CNFs network, which resulted in the transformation of the droplets into platelet-like structure. The thickness and size

of the platelets are not uniform because of the polydispersity of the resin droplets in and among the emulsions of various formations (Fig. 2.18). Nevertheless, due to the platelet-like structure of the resin droplets, the microstructure of the transparent PE nanocomposites resembled to that of the "brick-and-mortar" of the nacre (Fig. 2.15d and Fig. 2.17c). However, interestingly, this microstructure can be considered opposite to that of the nacre. Because, in nacre, the hard aragonite platelets (95%) are surrounded by the soft biopolymers (5%), whereas, in transparent PE nanocomposites, the soft acrylic resin platelets (~84%; modulus= 0.03 GPa) are surrounded by the network of strong and stiff CNFs (~16%; modulus≈140 GPa). This interesting hierarchical structure truly originated from the Pickering emulsion via the self-assembly of the CNF-covered resin droplets.

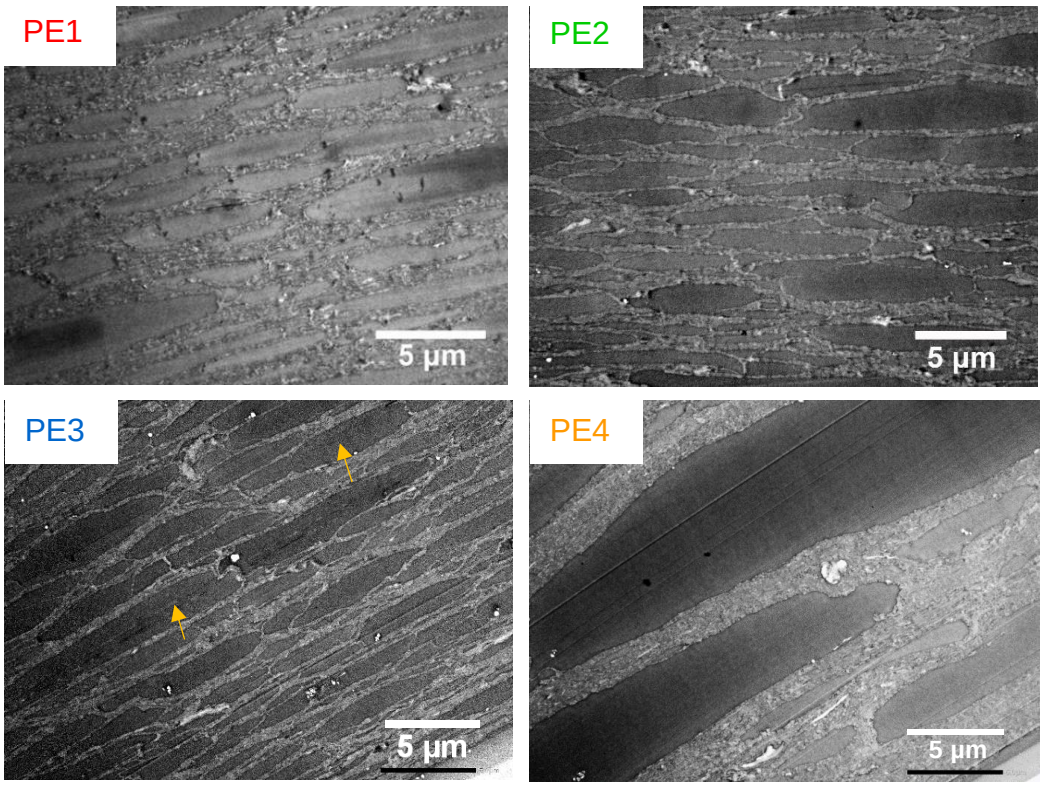

Figure 2.18. TEM images of the cross-section of the transparent PE nanocomposites. The arrows in PE3 indicate the platelet-like resin droplets. The whitish border around the droplets is made up of CNFs network. The effect of the bigger droplets can be seen in the microstructure of the PE4 nanocomposite.

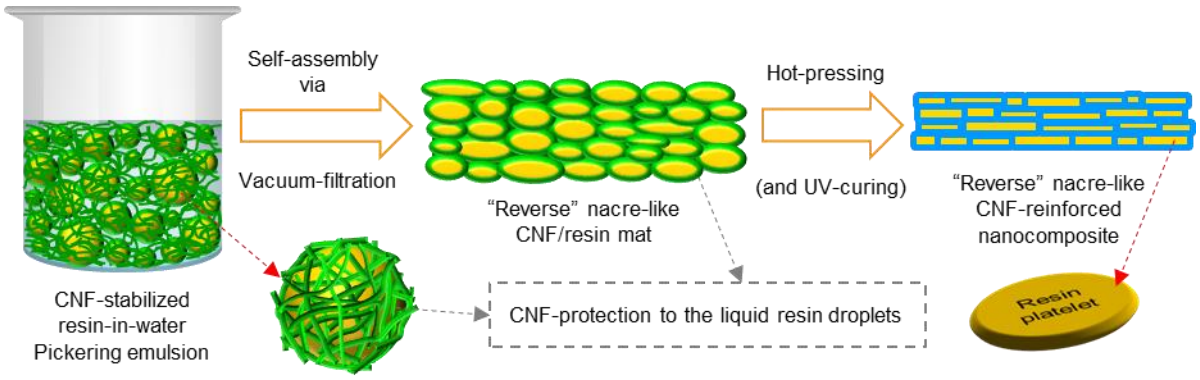

Figure 2.19. A graphical illustration of the development of hierarchical and nacre-mimetic microstructure in the CNF/resin mat and its corresponding transparent PE composite. The change in color from green to blue represents the penetration of resin into the surrounding CNFs network.

As mentioned above that the materials having a hierarchical structure offer excellent mechanical functionalities. Therefore, it is of vital importance to compare the microstructure of the transparent IM nanocomposites prepared by impregnation method with that of the PE nanocomposites prepared via Pickering emulsification method. The FE-SEM image of the cross-section of an IM nanocomposite is shown in Figure 1.16b in Chapter 1. When a nanopaper of nanocelluloses was impregnated by a resin, the nanopaper still remains intact inside the resulting nanocomposite. The IM nanocomposite, therefore, possessed a three-layer structure. The middle layer was consisted of an intact CNF-nanopaper, the nanopores of which were impregnated by the resin. The outer two layers were composed of the neat resin; however, the presence or thickness of the outer resin layers depends on the CNF-content and compactness of the nanopaper. Therefore, it can be expected that the mechanical behavior of an IM nanocomposite will be governed mainly by the stiff nanopaper. Whereas, the mechanical behavior of the PE nanocomposites prepared by the Pickering emulsification method is expected to be governed by both the homogeneously-dispersed CNF-network and the unique hierarchical structure.

2.3.7 Mechanical properties of the nanocomposites

Figure 2.20 and Table 2.3 highlight the extraordinary mechanical properties of the PE nanocomposites compared with the IM composite and neat acrylic resin film. Specifically, the strengths of the nanocomposites made from PE1, PE2, PE3, and PE4 were 40.14, 35.69, 34.61,

and 32.44 MPa, respectively. In contrast, the strength of the IM composite was 28.35 MPa, even at a ~4 wt % higher CNF content. A large strain-to-failure − 12.49% for PE1, 13.23% for PE2, 13.35% for PE3, and 9.05% for PE4 compared with only 2.06% for the IM composites − indicated that the PE nanocomposites prepared by Pickering emulsification method were flexible, and combined with their high strength significantly increased their toughness. The toughness was approximately 9 times higher than that of the IM composites. The elastic modulus of the PE nanocomposites (1.50, 1.28, 1.19, and 1.36 GPa for PE1, PE2, PE3, and PE4, respectively) was lower than that of the IM composites (2.85 GPa). This may be due to the fact that in an IM composite, the CNF nanopaper was laid intact and sandwiched between two thick resin layers (Figure 1.16b); this implies that the highly H-bonded stiff CNF network mainly governed the mechanical properties of its resin-impregnated composites [19,46]. It is likely that the inclusion of the resin platelets in the hierarchical CNF network of the PE nanocomposites may reduce H-bonding and lower the stiffness, but clearly, a synergistic strengthening and toughening mechanism was present.

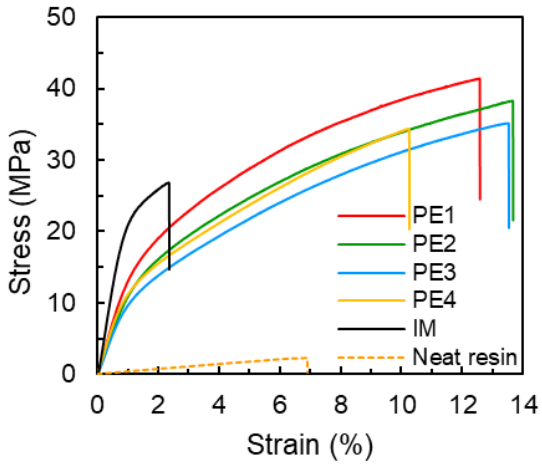

Figure 2.20. Tensile stress−strain curves of the CNF-reinforced nanocomposites and neat resin film. Compared with the IM composite and neat resin film, the PE nanocomposites prepared via Pickering emulsification method have extraordinary strength, toughness, and ductility, thanks to their hierarchical and synergistic “reverse” brick-and-mortar architecture.

In natural nacre, the brick-and-mortar arrangement of hard and soft materials synergistically bears the load, dissipates stress across the interfaces through mutual sliding, and impedes crack propagation through crack deflection and crack bridging [39−44]. In PE nanocomposites, the “reverse” nacre-like two-tier hierarchical CNF-network carried the load,

and stress dissipation occurred at the interfaces of the CNF network/resin platelets through mutual sliding and also in the CNF network itself where the soft resin penetrated during hot-pressing. To prove this synergistic mechanism, the fractured surface of the PE nanocomposites after tensile test was investigated under the FE-SEM. The occurrence of crack bridging by CNFs and crack deflection by microcrack formation were observed (Fig. 2.21a–c), which are known mechanisms of extrinsic toughening [39–44]. In contrast, no such synergistic mechanism in the IM nanocomposite was observed (Fig. 2.21d,e). Rather, the facture mechanism was dominated by the breaking of the CNFs in the resin-impregnated nanopaper. The CNFs in the nanopaper were also locked in position by the intensive H-bonding [47–51]. Therefore, the mechanical behavior of the IM nanocomposites was mostly governed by the nanopaper containing strong network of the stiff CNFs.

Table 2.3. Comparison of mechanical properties of the PE nanocomposites, IM composites, and neat acrylic resin film. The values in the parenthesis represent standard deviation.

Sample	Strength [MPa]	Toughness [MJ m^{-3}]	Modulus [GPa]	Strain-to-failure [%]
IM	28.35 (2.51)	0.41 (0.06)	2.85 (0.25)	2.06 (0.26)
PE1	40.14 (4.49)	3.69 (0.02)	1.50 (0.03)	12.49 (0.43)
PE2	35.69 (2.27)	3.54 (0.14)	1.28 (0.07)	13.23 (0.85)
PE3	34.61 (2.42)	3.49 (0.37)	1.19 (0.05)	13.35 (2.00)
PE4	32.44 (2.40)	2.19 (0.22)	1.36 (0.04)	9.05 (1.25)
Neat resin	2.00 (0.26)	0.07 (0.02)	0.03 (0.00)	6.17 (0.72)

Apart from the high strength, toughness and strain-to-failure of the PE nanocomposites compared with the IM nanocomposites at a similar CNFs content, the mechanical properties of the PE nanocomposites can be tuned easily by varying the droplet size of the resin simply by adjusting the water content in the emulsion while keeping the CNF-content identical. For example, diluted PE1 emulsion, having relatively uniform and tiny resin droplets, produced stronger, tougher, and stiffer nanocomposites compared with PE2, PE3 and PE4 (Fig. 2.20 and Table 2.3). This is because more uniform and smaller resin platelets in the nanocomposite resulted in much more homogeneous CNF/resin interfaces, thereby causing an effective

transfer of the stress across interfaces. Another interesting observation can be made that the modulus of the PE4 nanocomposites was higher than that of PE2 and PE3 nanocomposites and the strain-to-failure of the PE4 nanocomposites was lower than that of other PE nanocomposites (Fig. 2.20 and Table 2.3). The possible reason could be the presence of thicker CNFs network around the resin platelets resulted from the presence of bigger droplets in the PE4 emulsion (Fig. 2.18).

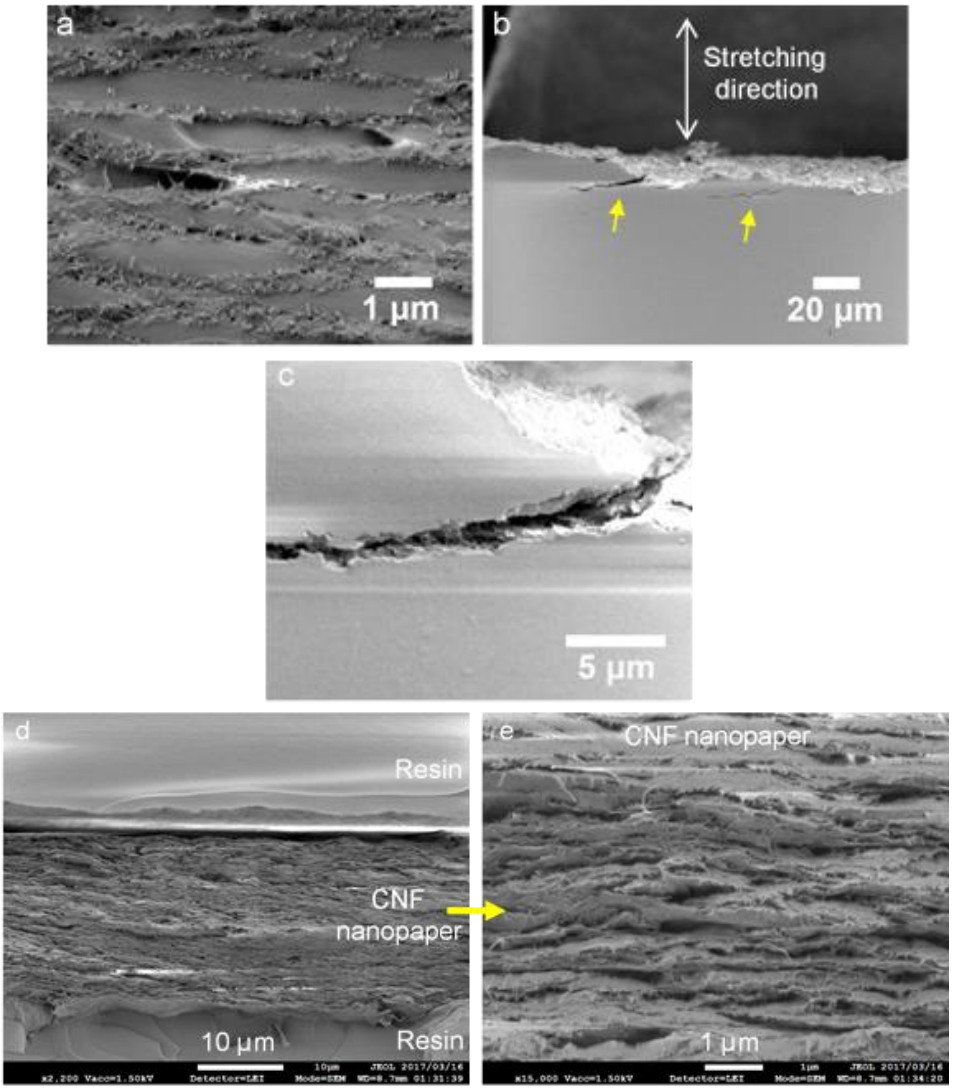

Figure 2.21. FE-SEM images of the fracture surface of the reverse nacre-like PE nanocomposite (PE3) after the tensile test. (a) Top view of the fracture surface showing "protruded" CNFs, which provided crack bridging. (b) Side view of the fracture surface showing crack deflection by microcrack formation. (c) Zoom-in image showing CNF bridging inside the microcrack. (d,e) Fracture surface of an IM composite after tensile test under different magnifications showing two outer resin layers with a smooth fractured-surface, and the sandwiched resin-impregnated CNF-nanopaper with a layered structure showing an evidence of the severing of nanofibers.

2.3.8 Thermal expansion of the nanocomposites

The high thermal expansion of polymers, especially of flexible polymers the CTE of which often exceeds 200 ppm K^{-1} [34], is a potential drawback for their applications. For example, the fabrication of optoelectronic devices often includes high-temperature (>100 °C) processing steps. The high thermal expansion of the polymer films often creates issues during the fabrication of devices. Therefore, brittle glass substrates are still preferred because of their low thermal expansion, CTE 7−10 ppm K^{-1} [52]. CNFs, having crystals of very low CTE (0.1 ppm K^{-1}), are highly effective in reducing thermal expansion of the polymers while keeping their transparency [19,20,34]. Figure 2.22 and Table 2.4 highlight that the thermal expansion of the PE nanocomposites was extremely low, CTE ∼13 ppm K^{-1}, which is comparable to that of glass. The inclusion of CNFs drastically reduced (∼15 times) the thermal expansion of the soft acrylic resin. However, the IM composite had a lower CTE of 9.9 ppm K^{-1}, which was due to the intact sandwiched CNF nanopaper with a CTE of 8.3 ppm K^{-1} (literature value 8.5 ppm K^{-1} [53]), as well as the ∼4 wt % higher CNF content. For comparison, the CTE of a transparent and thermally stable poly(ethylene terephthalate) film (PET; Lumirror, Toray) that is being used in the optoelectronics industry was also measured. The CTE was 38 ppm K^{-1}, much higher than that of the transparent PE nanocomposites. This suggests that the high-performance transparent nanocomposites made from Pickering emulsion have a strong potential to be used as a substrate material for flexible electronics.

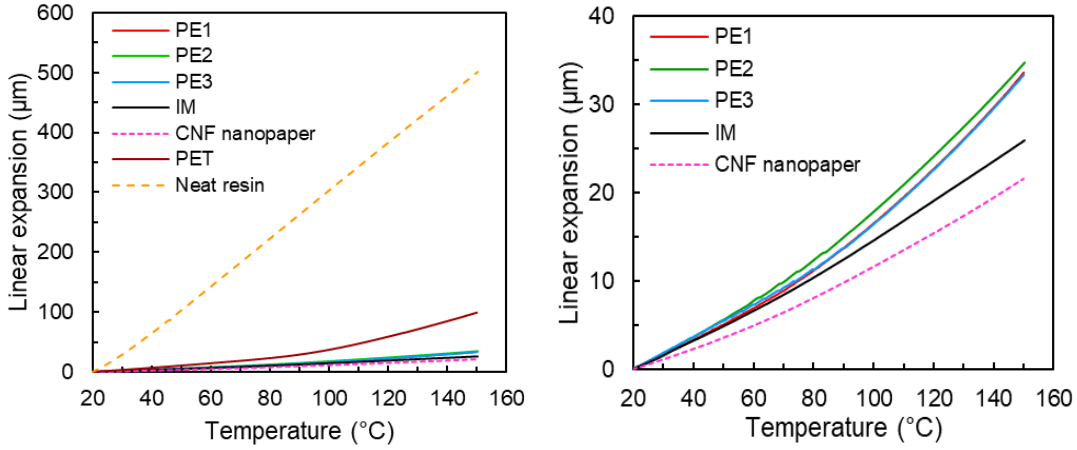

Figure 2.22. Linear thermal expansion of the nanocomposites, CNF nanopaper, commercial PET film, and neat resin film.

Table 2.4. The CTE values of the nanocomposites, CNF-nanopaper, PET film, and neat acrylic resin film.

Sample	PE1	PE2	PE3	PE4	IM	CNF nanopaper	PET	Neat resin
CTE [ppm K^{-1}]	12.85	13.27	12.77	12.71	9.92	8.25	37.97	191.66

2.3.9 TGA to determine CNFs content of the nanocomposites

In the previous sections of this chapter, it has been discussed that a small amount of resin was lost during hot-pressing of the CNF/resin mat. Therefore, the final CNF-content in the PE nanocomposites should differ from that of the Pickering emulsions. Therefore, a new method based on the TGA-residue was devised to precisely determine the CNF-content in the nanocomposites.

Apart from determining the thermal stability of a material, TGA has been widely used to determine the composition of a material. TGA method to determine composition mainly relies on the characteristic thermal decomposition temperature of each component. The area of the differential TGA (DTG) curve can be directly used to estimate the weight of each component [54]. However, if the thermal decomposition characteristic of two or more components overlaps, this method would produce faulty results.

In this study, it was found that the TGA-residue content of a CNF-resin mixture is directly proportional to the CNF-content. Therefore, a calibration graph was developed first from a known composition of CNF-resin mixtures to obtain the regression equation (Fig. 2.23). A high degree of correlation, R^2= 0.9973, was found. Then, the TGA-residue content of the PE nanocomposites were put in the equation to estimate the CNFs content.

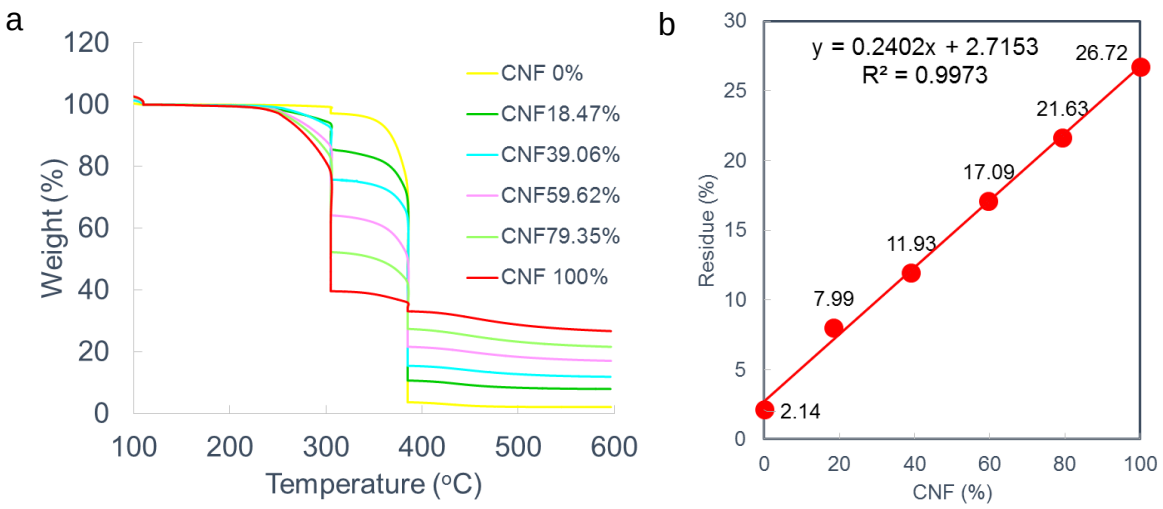

Figure 2.23. (a) TGA thermograms of the CNF-resin mixture with a known composition. (b) Correlation of the CNF-content with the TGA-residue content. The number indicates residue content.

2.3.10 3D-molded transparent nanocomposite

The modulus of the transparent PE nanocomposites prepared by the Pickering emulsification method is about one-half or even lower than that of the IM nanocomposite at a similar content of CNFs (Fig. 2.20 and Table 2.3). It is a clear evidence that the inclusion of the resin platelets significantly minimized the H-bonding among the nanofibers. Additionally, it is an advantaged that the tiny liquid resin droplets can be confined into the CNF-network (i.e., CNF/resin mat) without any leakage. Due to the liquid droplets, the modulus of the mat is drastically low as shown in Figure 2.24.

Realizing those advantages, the CNF/resin non-polymerized mat was placed into a lens-shaped molding die and hot-pressed at 150 °C and 5 MPa followed by UV polymerization (Fig. 2.25). A perfectly molded lens-like transparent PE nanocomposite was obtained. This was possible due to the presence of liquid resin droplets in the mat, which also reduced the extent of H-bonding in the bulk CNFs network, therefore, enabled 3D-molding of the mat with good precision. On the other hand, an attempted to mold an IM composite using a hot-press inevitably failed (Fig. 1.16 in Chapter 1). The IM composite did not form a perfect lens-like shape and developed many cracks. Evidently, such a 3D-molded transparent material with high mechanical performance, low CTE, and flexibility could not be obtained by the impregnation

method because the strong recoverable H-bonds make the CNF nanopaper substantially less deformable.

Realization of CNF-reinforced 3D-molded optically transparent nanocomposite with low CTE and high flexibility may broaden the application area of the CNF-reinforced materials. For example, they could be used in applications such as the substrate for contact lens sensors and curved displays. Contact lens sensors are smart microelectronic devices that can monitor the blood glucose level from the eye-fluid or capture an image with a blink of the eye [55,56].

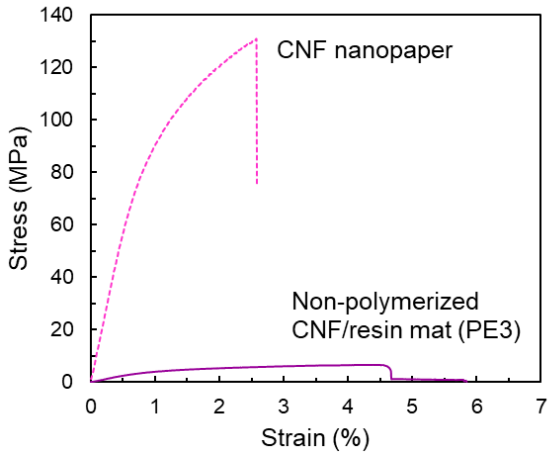

Figure 2.24. Comparison of the stress–strain behavior of a CNF-nanopaper and a non-polymerized CNF/resin mat. The nanopaper contains ~0.04 g CNFs, equivalent to the CNFs amount present in the mat. Due to the inclusion of the liquid resin droplets, the modulus of the CNF/resin mat is very low.

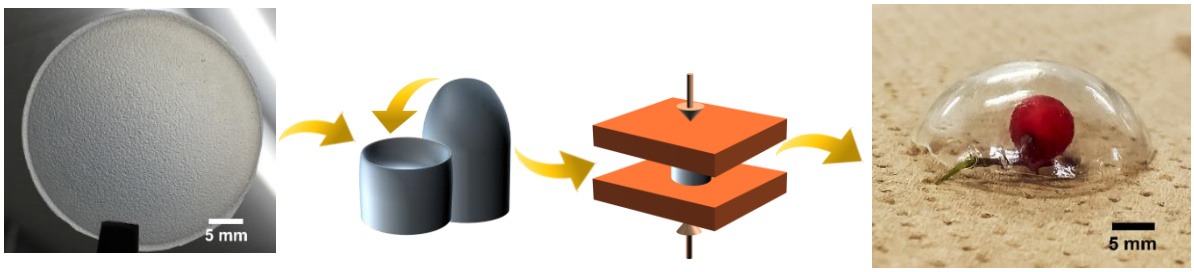

Figure 2.25. Facile fabrication of the 3D-molded transparent nanocomposite.

2.3.11 Micro-molded nanocomposites

Inspired from the above results, the CNF/resin mat was placed on a patterned sapphire substrate (PSS) instead of a molding die, and subsequently hot-pressed and UV-polymerized. The obtained PE nanocomposite exhibited a rainbow color indicating the precise transfer of the pattern on its surface (Fig. 2.26a). Figure 2.26b–e indicates that the surface of the mat can be micro-patterned with any shape; even multi-tier pattering, double-sided patterning, and nano-scale patterning are easily possible. This is because the liquid resin in the mat can squeeze-out during hot-pressing, which can take any opposite shape of the patterned substrate. Hence, nano- and microscale polymeric structures can be easily and directly obtained with great precision on the surface of the CN-reinforced transparent PE nanocomposites. This molding strategy can be regarded as a simple form of the micro- and nanoimprint lithography techniques. It does not require any sophisticated procedure/equipment such as in the case of conventional lithography where photoresist, mask, and etching technologies are used [57,58]. Also, considering the tough and flexible behavior of the PE nanocomposites, the roll-to-roll micro-patterning process could be adopted.

Surface-patterned polymeric films have numerous high-tech applications in areas such as semiconductor microelectronics, wide-angle-of-view 3D-imaging, stealth devices, fuel-cells, optoelectronics (e.g., high-efficiency organic-light-emitting-diodes (OLEDs)) and as antireflection, light-scattering, and light-trapping coatings or substrates in high-performance photovoltaics [57−70]. Owing to the good mechanical performance, a CTE similar to that of glass, high flexibility, and ease of fabrication, the surface-patterned PE nanocomposites prepared via Pickering emulsification method are suitable candidates for those applications.

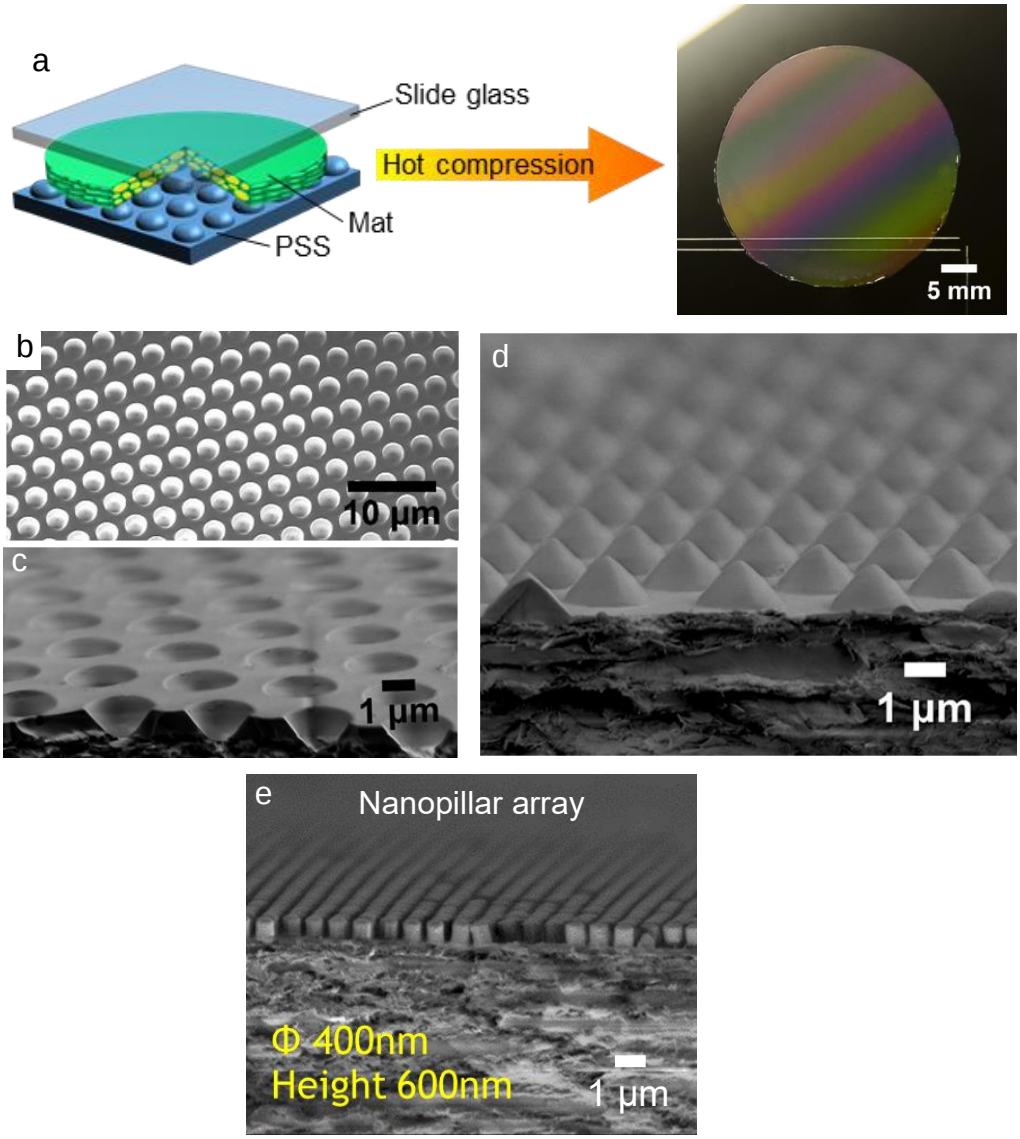

Figure 2.26. (a) Facile in-situ fabrication of surface micro-molded transparent PE nanocomposite. (b–e) Micro/nanopatterns with various shapes can easily and directly be obtained on the surface of the PE nanocomposite with great precision.

2.4 Summary

In conclusion, a simple water-based Pickering emulsification pathway was developed to fabricate hierarchical nanocomposites of immiscible polymer and native CNFs. The hierarchical network of CNFs was well dispersed throughout the nanocomposites, as indicated by the high optical transparency of the nanocomposites. The nanocomposites featured a unique "reverse" nacre-like microstructure made up of soft polymer platelets (84 wt %) surrounded by a strong hierarchical network of CNFs (16 wt %). The microstructure was self-assembled during vacuum filtration (dewatering) of the CNF-stabilized resin-in-water Pickering emulsion.

This unique microstructure synergistically led to a rare combination of high strength (40.14 MPa) and toughness (3.69 MJ m^{-3}), which are 20 and 53 times higher than that of neat polymer, respectively. The nanocomposites also possessed a high optical transparency (89%), a high flexibility, and a CTE similar to that of glass (~13 ppm K^{-1}, $1/15^{th}$ of the neat polymer) owing to the well-dispersed cellulose nanofibers. Moreover, the liquid resin droplets in the vacuum-filtered Pickering emulsion mat minimized the H-bonding in the nanofiber network, which allowed the otherwise inaccessible molding of the nanocomposite into a 3D complex shape. The surface of the nanocomposite could be patterned with micro/nanoscale features with a high resolution and fidelity by direct compression molding. The high mechanical, thermal, and optical performances together with the ease of fabrication process indicate that the nanocomposites prepared via Pickering emulsion method are suitable candidates as substrates for high-performance flexible/wearable (opto)electronic devices including displays, smart contact lens sensors, and photovoltaics. The facile Pickering emulsification approach should be easily applicable to a vast range of immiscible polymers and nanoreinforcements for unlocking new class of functional hierarchical nanocomposite materials.

2.5 References

1. Blaker J. J., Lee K. –Y., Li X., Menner A., and Bismarck A. Renewable nanocomposite polymer foams synthesized from Pickering emulsion templates. Green Chemistry, 2009, **11**, 1321–1326.
2. Elmabrouk A B., Wim T., Dufresne A., and Boufi S. Preparation of poly(styrene-co-hexylacrylate)/cellulose whiskers nanocomposites via miniemulsion polymerization. Journal of Applied Polymer Science, 2009, **114**, 2946–2955.
3. Mabrouk A. B, Vilar M. R., Magnin A., Belgacem M. N., and Boufi S. Synthesis and characterization of cellulose whiskers/polymer nanocomposite dispersion by mini-emulsion polymerization. Journal of Colloid and Interface Science, 2011, **363**, 129–136.
4. Li Y., Yu S., Chen P., Rojas R., Hajian A., and Berglund L. Cellulose Nanofibers Enable Paraffin Encapsulation and the Formation of Stable Thermal Regulation Nanocomposites. Nano Energy 2017, **34**, 541–548.
5. Svagan A. J., Busko D., Avlasevich Y., Glasser G., Baluschev S., and Landfester K. Photon energy upconverting nanopaper: A bioinspired oxygen protection strategy. ACS Nano, 2014, **8**, 8198–8207.

6. Nypelö T., Rodriguez-Abreu C., Kolenko Y. V., Rivas J., and Rojas O. J. Microbeads and hollow microcapsules obtained by self-assembly of Pickering magneto-responsive cellulose nanocrystals. ACS Applied Materials and Interfaces, 2014, **6**, 16851−16858.
7. Svagan A. J., Musyanovych A., Kappl M., Bernhardt M., Glasser G., Wohnhaas C., Berglund L. A., Risbo J., and Landfester K. Cellulose nanofiber/nanocrystal reinforced capsules: A fast and facile approach toward assembly of liquid-core capsules with high mechanical stability. Biomacromolecules, 2014, **15**, 1852−1859.
8. Shams M. I, and Yano H. Doubly curved nanofiber-reinforced optically transparent composites. Scientific Reports, 2015, **5**, 16421.
9. Fujisawa S., Togawa, E., and Kuroda K. Facile route to transparent, strong, and thermally stable nanocellulose/polymer nanocomposites from an aqueous Pickering emulsion. Biomacromolecules 2017, **18**, 266–271.
10. Abe K., Iwamoto S., and Yano H. Obtaining cellulose nanofibers with a uniform width of 15 nm from wood. Biomacromolecules 2007, **8**, 3276–3278.
11. Wise L. E., Murphy M., and D'Addieco A. A. Chlorite holocellulose, its fractionation and bearing on summative wood analysis and on studies on the hemicelluloses. Paper Trade Journal, 1946, **122**, 35–43.
12. Segal L., Creely J. J., Martin A. E., and Conrad C. M. An empirical method for estimating the degree of crystallinity of native cellulose using the X-ray diffractometer. Textile Research Journal, 1959, **29**, 786–794.
13. Gans D. M., and Harkins W. D. The drop weight method for the determination of surface tension. The effect of an inclination of the tip upon the drop weight. Journal of the American Chemical Society, 1930, **52**, 2287–2289.
14. Bailey K. C. Determination of surface tension by the drop-weight method. Nature, 1936, **137**, 323–323.
15. Harkins W. D., and Brown F. E. The determination of surface tension (free surface energy), and the weight of falling drops: The surface tension of water and benzene by the capillary height method. Journal of the American Chemical Society, 1919, **41**, 499–524.
16. Wilkinson M. C. Extended use of, and comments on, the drop-weight (drop-volume) technique for the determination of surface and interfacial tensions. Journal of Colloid and Interface Science, 1972, **40**, 14–26.
17. Wilkinson M. C., and Aronson M. P. J. Applicability of the drop weight technique to the determination of the surface tensions of liquid metals. Journal of the Chemical Society, Faraday Transactions 1: Physical Chemistry in Condensed Phases, 1973, **69**, 474–480.

18. Lee B. B., Pogaku R., and Chan E. S. A critical review: Surface and interfacial tension measurement by the drop weight method. Chemical Engineering Communications, 2008, **195**, 889–924.
19. Yano H., Sugiyama J., Nakagaito A. N., Nogi M., Matsuura T., Hikita M., and Handa, K. Optically transparent composites reinforced with networks of bacterial nanofibers. Advanced Materials, 2005, **17**, 153–155.
20. Iwamoto S., Nakagaito A. N., Yano H., and Nogi M. Optically transparent composites reinforced with plant fiber-based nanofibers. Applied Physics A: Materials Science and Processing, 2005, **81**, 1109–1112.
21. Levy O., and Stroud D. Maxwell Garnett theory for mixtures of anisotropic inclusions: Application to conducting polymers. Physical Review B: Condensed Matter and Materials Physics, 1997, **56**, 8035–8046.
22. Seferis J. C. Refractive indices of polymers, solid state properties (Chapter 6). In Polymer Handbook (4th edition). Eds. J. Brandrup. E. H. Immergut, and E. A. Grulke, Wiley, New York, 1999, p. 571.
23. Iwamoto S., Nakagaito A. N., and Yano H. Nano-fibrillation of pulp fibers for the processing of transparent nanocomposites. Applied Physics A: Materials Science and Processing, 2007, **89**, 461–466.
24. Wang Q. Q., Zhu J. Y., Gleisner R., Kuster T. A., Baxa U., and McNeil S. E. Morphological development of cellulose fibrils of a bleached eucalyptus pulp by mechanical fibrillation. Cellulose, 2012, **19**, 1631–1643.
25. Ho T. T. T., Abe K., Zimmermann T., and Yano H. Nanofibrillation of pulp fibers by twin-screw extrusion. Cellulose, 2015, **22**, 421–433.
26. Kalashnikova I., Bizot H., Bertoncini P., Cathala B., and Capron I. Cellulosic nanorods of various aspect ratios for oil in water Pickering emulsions. Soft Matter, 2013, **9**, 952–959.
27. Ougiya H., Watanabe K., Morinaga Y., and Yoshinaga F. Emulsion-stabilizing effect of bacterial cellulose. Bioscience, Biotechnology, and Biochemistry, 1997, **61**, 1541–1545.
28. Winuprasith T., and Suphantharika M. Microfibrillated cellulose from mangosteen (*Garcinia mangostana* L.) rind: Preparation, characterization, and evaluation as an emulsion stabilizer. Food Hydrocolloids, 2013, **32**, 383–394.
29. Salas C., Nypelö T., Rodriguez-Abreu C., Carrillo C., and Rojas O. J. Nanocellulose properties and applications in colloids and interfaces. Current Opinion in Colloid & Interface Science, 2014, **19**, 383–396.

30. Xhanari K., Syverud K., Chinga-Carrasco G., Paso K., and Stenius P. Structure of nanofibrillated cellulose layers at the O/W interface. Journal of Colloid and Interface Science, 2011, **356**, 58–62.
31. Lee K. -Y, Blaker J. J., Murakami R., Heng J. Y. Y., and Bismarck A. Phase behavior of medium and high internal phase water-in-oil emulsions stabilized solely by hydrophobized bacterial cellulose nanofibrils. Langmuir, 2014, **30**, 452–460.
32. Cunha A. G., Mougel J. –B., Cathala B., Berglund L. A., and Capron I. Preparation of double Pickering emulsions stabilized by chemically tailored nanocelluloses. Langmuir 2014, **30**, 9327−9335.
33. Carrillo C. A., Nypelö T. E., and Rojas O. J. Cellulose nanofibrils for one-step stabilization of multiple emulsions (W/O/W) based on soybean oil. Journal of Colloid and Interface Science, 2015, **445**, 166–173.
34. Nogi M., and Yano H. Transparent nanocomposites based on cellulose produced by bacteria offer potential innovation in the electronics device industry. Advanced Materials, 2008, **20**, 1849–1852.
35. Christmann A., Longuet C., and Cuesta J. M. L. Transparent polymer nanocomposites: A new class of functional materials. In Nanomaterials and Surface Engineering. Ed. J. Takadoum. John Wiley & Sons Inc., New York, 2013, p. 41.
36. Wang Z., Li G., Xie G., and Zhang Z. Dispersion behavior of TiO2 nanoparticles in LLDPE/LDPE/TiO2 nanocomposites. Macromolecular Chemistry and Physics, 2005, **206**, 258–262.
37. Lakes R. Materials with structural hierarchy. Nature 1993, **361**, 511−515.
38. Fratzl P., and Weinkamer R. Nature's hierarchical materials. Progress in Materials Science, 2007, **52**, 1263−1334.
39. Launey M. E., and Ritchie R. O. On the fracture toughness of advanced materials. Advanced Materials, 2009, **21**, 2103−2110.
40. Wegst U. G. K., Bai H., Saiz E., Tomsia A. P., and Ritchie R. O. Bioinspired structural materials. Nature Materials, 2015, **14**, 23−36.
41. Espinosa H. D., Rim J. E., Barthelat F., and Buehler M. J. Merger of structure and material in nacre and bone – perspectives on de novo biomimetic materials. Progress in Materials Science, 2009, **54**, 1059−1100.
42. Jackson A. P., Vincent J. F. V., and Turner R. M. The mechanical design of nacre. Proceedings of the Royal Society, Series B, 1988, **234**, 415−440.

43. Kolednik P., Predan J., Fischer F. D., and Fratzl P. Bioinspired design criteria for damage-resistant materials with periodically varying microstructure. Advanced Functional Materials, 2011, **21**, 3634−3641.
44. Li X., Xu Z.-H., and Wang R. In situ observation of nanograin rotation and deformation in nacre. Nano Letters, 2006, **6**, 2301−2304.
45. Walther A., Bjurhager I., Malho J. -M., Pere J., Ruokolainen J., Berglund L. A., and Ikkala O. Large-area, lightweight and thick biomimetic composites with superior material properties via fast, economic, and green pathways. Nano Letters, 2010, **10**, 2742−2748.
46. Capadona J. R., Berg O. V. D., Capadona L. A., Schroeter M., Rowan S. J., Tyler D. J., and Weder C. A versatile approach for the processing of polymer nanocomposites with self-assembled nanofibre templates. Nature Nanotechnology, 2007, **2**, 765–769.
47. Zhu H., Zhu S., Jia Z., Parvinian S., Li Y., Vaaland O., Hu L., and Li T. Anomalous scaling law of strength and toughness of cellulose nanopaper. Proceedings of the National Academy of Sciences of the United States of America, 2015, **112**, 8971−8976.
48. Altaner C. M., Thomas L. H., Fernandes A. N., and Jarvis M. C. How cellulose stretches: Synergism between covalent and hydrogen bonding. Biomacromolecules, 2014, **15**, 791−798.
49. Henriksson M., Berglund L. A., Isaksson P., Lindström T., and Nishino T. Cellulose nanopaper structures of high toughness. Biomacromolecules, 2008, **9**, 1579−1585.
50. Keckes J., Burgert I., Frühmann K., Müller M., Kölln K., Hamilton M., Burghammer M., Roth S. V., Stanzl-Tschegg S., and Fratzl P. Cell-wall recovery after irreversible deformation of wood. Nature Materials, 2003, **2**, 810−813.
51. Fellers C. The structure of paper and its modelling (Chapter 1). In Paper Products Physics and Technology. Eds. M. Ek, G. Gellerstedt, and G. Henriksson, Walter de Gruyter, Berlin 2009, p. 13.
52. Ashby, M. F. Materials Selection in Mechanical Design. Pergamon Press: Oxford, 1992.
53. Nogi M., Iwamoto S., Nakagaito A. N., and Yano H. Optically transparent nanofiber paper. Advanced Materials, 2009, **21**, 1595–1598.
54. Carrier M., Loppinet-Serani A., Denux D., Lasnier J.-M., Ham-Pichavant F., Cansell F., and Aymonier C. Thermogravimetric analysis as a new method to determine the lignocellulosic composition of biomass. Biomass and Bioenergy, 2011, **35**, 298–307.
55. Farandos N. M., Yetisen A. K., Monteiro M. J., Lowe C. R., and Yun S. H. Contact lens sensors in ocular diagnostics. Advanced Healthcare Materials, 2015, **4**, 792–810.

56. Sako Y., Iwasaki M., Hayashi K., Kon T., Nakamura T., Onuma T., and Tange A. Contact lens and storage medium. Sony Corporation, US patent 20160097940A1, 2016.
57. Nie Z., and Kumacheva E. Patterning surfaces with functional polymers. Nature Materials, 2008, **7**, 277−290.
58. Menard E., Meitl M. A., Sun Y., Park J.–U., Shir D. J.–L., Nam Y.–S., Jeon S., and Rogers J. A. Micro- and nanopatterning techniques for organic electronic and optoelectronic systems. Chemical Reviews, 2007, **107**, 1117−1160.
59. Brongersma M. L., Cui Y., and Fan S. Light management for photovoltaics using high-index nanostructures. Nature Materials 2014, **13**, 451–460.
60. Qiao W., Huang W., Liu Y., Li X., Chen L.–S., and Tang J.–X. Toward scalable flexible nanomanufacturing for photonic structures and devices. Advanced Materials, 2016, **28**, 10353–10380.
61. Jeong K. –H., Kim J., and Lee L. P. Biologically inspired artificial compound eyes. Science, 2006, **312**, 557–561.
62. Moghimi M. J., Fernandes J., Kanhere A., and Jiang H. Micro-fresnel-zone-plate array on flexible substrate for large field-of-view and focus scanning. Scientific Reports, 2015, **5**, 15861.
63. Nalwa K. S., Park J. –M., Ho K. –M., and Chaudhary S. On realizing higher efficiency polymer solar cells using a textured substrate platform. Advanced Materials, 2011, **23**, 112–116.
64. Hippola C., Kaudal R., Manna E., Xiao T., Peer A., Biswas R., Slafer W. D., Trovato T., Shinar J., and Shinar R. Enhanced light extraction from OLEDs fabricated on patterned plastic substrates. Advanced Optical Materials, 2018, **6**, 1701244.
65. Xiang H.–Y., Li Y.–Q., Zhou L., Xie H.–J., Li C., Ou Q.–D., Chen L.–S., Lee C.–S., Lee S.–T., and Tang J.–X. Outcoupling-enhanced flexible organic light-emitting diodes on ameliorated plastic substrate with built-in indium–tin-oxide-free transparent electrode. ACS Nano, 2015, **9**, 7553–7562.
66. Abramowitz M., and Davidson M. W. Microlens arrays. https://www.olympus-lifescience.com/zh/microscope-resource/primer/digitalimaging/concepts/microlensarray/ (accessed Jun 30, 2018).
67. Song Y. M., Xie Y., Malyarchuk V., Xiao J., Jung I., Choi K.–J., Liu Z., Park H., Lu C., Kim R.–H., Li R., Crozier K. B., Huang Y., and Rogers J. A. Digital cameras with designs inspired by the arthropod eye. Nature, 2013, **497**, 95–99.

68. Wu D., Wang J.–N., Niu L.–G., Zhang X. L., Wu S. Z., Chen Q.–D., Lee L. P., and Sun H. B. Bioinspired fabrication of high-quality 3D artificial compound eyes by voxel-modulation femtosecond laser writing for distortion-free wide-field-of-view imaging. Advanced Optical Materials, 2014, **2**, 751–758.
69. Diao Z., Kraus M., Brunner R., Dirks J.–H., and Spatz J. P. Nanostructured stealth surfaces for visible and near-infrared light. Nano Letters, 2016, **16**, 6610–6616.
70. Zhou M., Xu Y., and Lei Y. Heterogeneous nanostructure array for electrochemical energy conversion and storage. Nano Today, 2018, **20**, 33–57.

Chapter 3
Effect of CNF Content on the Microstructure and Properties of the Nanocomposites

3.1 Introduction

In Chapter 2, the development of a facile Pickering emulsification method and its potential to obtain optically transparent CNF-reinforced nanocomposites with 3D-moldability in nano-to-macro scale was described. One of the fascinating results was the development of a self-assembled structural hierarchy in the PE nanocomposites. Owing to the hierarchical structure, the PE nanocomposites combined high strength and toughness compared to that of IM nanocomposites. Interestingly, apart from 20 and 50 times improvement respectively in the tensile strength and modulus of the acrylic resin at a ~16 wt% CNFs content, the strain-to-failure of the neat resin improved ~2 times, which can be attributed to the formation of a unique hierarchical microstructure of resin droplets encapsulated by the CNF networks that delayed or prevented crack propagation and improved stress-transfer processes. This is a definite advantage of the nanocomposites prepared by the Pickering emulsion process. Because, when a resin is reinforced by the strong and stiff CNF-network, the elongation capability of the resin either decreases or remains similar to the original. This phenomena was also observed for the IM nanocomposites in this work and in literature. For example, Okahisa et al. prepared IM composites with the same resin containing 35–40 wt% CNFs and found no improvement in the strain-to-failure [1]. Suzuki et al. fabricated nanocomposites of polypropylene (PP) and high-density polyethylene (HDPE) using 20–30% CNFs as the reinforcement via melt compounding; the strain-to-failure of the nanocomposites was drastically low than that of PP and HDPE [2,3]. Fujisawa et al. reported on an improvement in tensile strength and modulus of 12 wt% TEMPO-CNF-reinforced polystyrene nanocomposites; however, the strain-to-failure of polystyrene was not improved [4].

Therefore, it would be interesting to investigate the effect of the CNFs content on the mechanical performances of the hierarchical PE nanocomposites. Expectation was that the high CNFs content would improve the strength and modulus of the PE nanocomposites, but without

compromising the strain-to-failure. As a result, a stronger and stiffer nanocomposite with a high mechanical flexibility, and hence, a high toughness would be obtained.

Hence, in this part of the study, CNF-reinforced acrylic resin nanocomposites with various CNFs contents were prepared using both the Pickering emulsion method and impregnation method, and the resulting properties were compared. The changes in the hierarchical structure of the nanocomposites were investigated, and described in terms of their mechanical properties together with the optical transparency and thermal stability.

3.2 Materials and method

3.2.1. Materials

The sugarcane bagasse pulp used as a raw material for CNFs preparation was kindly provided by Eastern Sugar & Cane Co., Ltd., Thailand. Acrylic resin monomer (2.2 bis[4-(acryloxypolyethoxy)phenyl]propane (ABPE-10) (refractive index of 1.516) used as a matrix was supplied by Shin-Nakamura Chemical Co., Ltd., Japan. A photoinitiator 2-hydroxy-2-methylpropiophenone, supplied by Wako Pure Chemical Industries, Japan, was added (0.25 wt%) to the monomer before use.

3.2.2. Preparation of CNFs

The bagasse was initially pre-treated with 3 wt% KOH solution at bagasse to liquor ratio of 1 to 10 for 2 h at 165 °C in a closed pulping unit, washed with distilled water, and completely dried. Subsequently, a bleaching process described in Chapter 2 was applied to the pre-treated bagasse. Briefly, the bagasse pulp was treated with acidified $NaClO_2$ at 80 °C for 5 h to remove lignin, and then 4 wt% KOH at 90 °C for 2 h to remove most of the hemicelluloses. The bagasse was additionally treated with acidified $NaClO_2$ at 80 °C for 3 h to eliminate any residual lignin. The treated fibers were washed with distilled water until neutralization. The fibers were dispersed in distilled water at a concentration of 0.8 wt% and initially fibrillated using a Vitamix blender (Osaka Chemical Co. Ltd.) for 1 min at 5000 rpm. Then, the slurry was passed through a grinder following the conditions described in Chapter 2.

3.2.3. Preparation of transparent nanocomposites and determination of CNFs content

The CNF reinforced nanocomposites were prepared by a similar procedure described in Chapter 2 with minor modifications. The resin monomer was mixed with CNFs and distilled

water using a Vitamix blender (Osaka Chemical Co. Ltd.) at 5000 rpm for 2 min, and then at 37000 rpm for 5 min. After a 5-min interval, the mixture was again blended for 5 min at 37000 rpm. The CNF-content in relation to resin was 3, 5, 10, and 15 wt%. Therefore, the corresponding emulsions were termed as PE3, PE5, PE10, and PE15, respectively. The obtained milky Pickering emulsion was then vacuum-filtered using a 0.1-µm-pore-size polytetrafluoroethylene (PTFE) filter membrane to obtain a CNF/resin mat, and the mat was hot-pressed at 150 °C and 2 MPa for 5 min. The pressed mat was subsequently UV-cured with a F300S UV lamp/LC6 conveyer system (20 J cm^{-2}, Fusion UV Systems, USA) to obtain a transparent nanocomposite film. The final CNFs weight-percentages of the nanocomposites after hot-pressing were 4, 9, 18, and 25, determined from the regression equation obtained from the TGA-residue versus bagasse CNFs graph (Fig. 3.1) (please also see Chapter 2 for more details). The composites were coded as PEx, where x refers to the CNFs content in the nanocomposites. Figure 3.2 illustrates the Pickering emulsification process used to prepare CNF-reinforced nanocomposites.

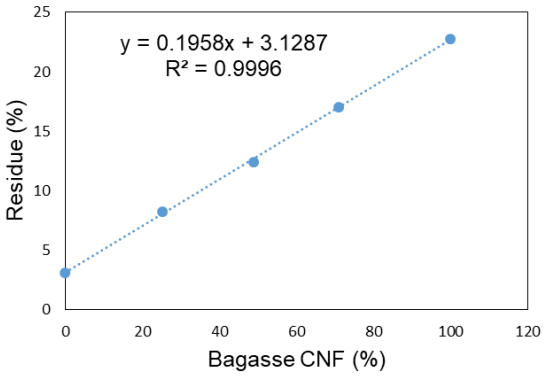

Figure 3.1. TGA-residue versus bagasse CNFs graph with the regression equation to determine the CNF-content of the nanocomposites. TGA was performed by placing approximately 5–10 mg mixture of the dried-CNFs and cured-resin of known composition on a platinum pan, stabilized at 110 °C for 10 min to remove residual moisture, and analyzed from 110 to 600 °C at a heating rate of 10 °C min^{-1} under a nitrogen flow rate of 100 ml min^{-1}.

To obtain IM nanocomposites as a control sample, the 0.1 wt% CNFs suspension was subjected to vacuum filtration, and the wet sheet was then hot-pressed at 110 °C for 30 min with the pressure of 0.1 MPa. The prepared CNF sheets were impregnated into the acrylic resin for 12 h, and the resin-impregnated CNF sheet composites placed between two glass slides were mechanically pressed under different pressures. The samples were subsequently UV-

cured to obtain the nanocomposites with CNF-contents of 15, 20 and 26 wt%. The impregnated composites were coded as IMx, where x refers to the CNFs content.

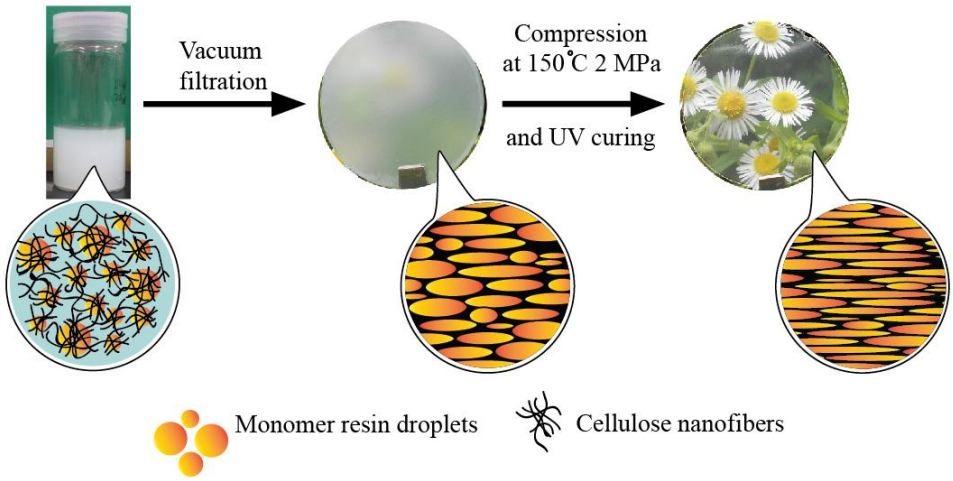

Figure 3.2. Fabrication of the composites by the Pickering emulsification process.

3.2.4. Characterizations

The FE-SEM imaging, light transmittance measurement, tensile mechanical testing, and thermal expansion analysis were done according to the procedure described in Chapter 2.

3.3 Results and discussion

3.3.1. Morphology of Pickering emulsions and nanocomposites

Figure 3.3a shows CNFs with average widths of 19.1 nm and lengths of more than 2 µm were isolated from sugarcane bagasse, and Figure 3.3b presents Pickering emulsions with various CNFs contents after storing in dark at the room temperature for 4 weeks. The Pickering emulsions PE3 and PE5 started to precipitate after one day. Whereas, no precipitation was seen for PE10 and PE15, even after 4 weeks. At a low content of CNFs, the CNF network might not be dense enough to encapsulate resin droplets in water. Notably, the effect of the precipitation in PE3 and PE5 can be ignored, because the emulsions were filtered immediately after their preparation.

During the Pickering emulsion preparation, the resin droplets were covered by the CNF-network, thereby, CNF-networks were formed at the interfaces between the resin droplets and water, as shown in Figure 3.4a,b. The formation of CNF-networks prevented flocculation and coalescence of the resin droplets in water, acting as an emulsion stabilizer [5–15]. The

diameters of the emulsion droplets covered by CNFs were 1.28 ± 0.53 µm for PE3. As the CNF-content was increased, the droplet diameter was also increased. The average diameters of PE5, PE10, and PE15 were 1.90 ± 1.15, 2.00 ± 1.46 and 1.95 ± 2.76 µm, respectively. The droplets became more polydispersed at higher CNFs concentrations, which suggested that a thick network of CNFs was developed at the high CNF-contents that in turn increased the viscosity of the emulsions, thereby, size and polydispersity of the droplets.

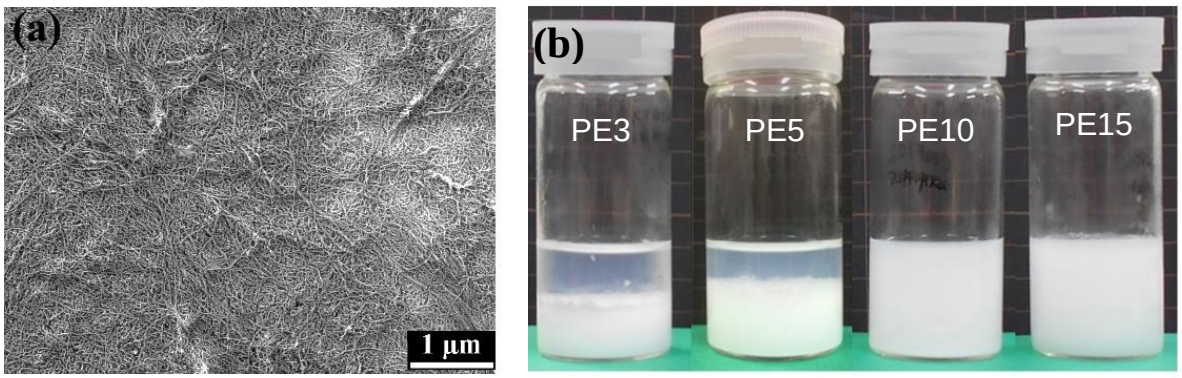

Figure 3.3. (a) Morphology of CNFs prepared from bagasse. (b) Photograph of Pickering emulsions with various contents of CNFs taken after storage at room temperature for 4 weeks.

The emulsion was subsequently vacuum-filtered to form a CNF/resin nanocomposite mat. The fracture surfaces of the non-pressed mats with 3 and 10 wt% CNFs are shown in Figure 3.4c,d. The round shape of the droplets in the emulsion became oval-shaped owing to the suction pressure during vacuum-filtration. When a compressive force was applied to the mat with heat, the morphology of the resin droplets changed to platelet-like shapes as can be observed in the fracture surface of the nanocomposites (Fig 3.4e,f). A homogenous distribution of multilayers of the CNF-networks throughout the nanocomposites was also observed. Conversely, in the IM composite, a resin-impregnated CNF-nanopaper was only laminated between two thik layers of the neat resin (Fig. 3.5).

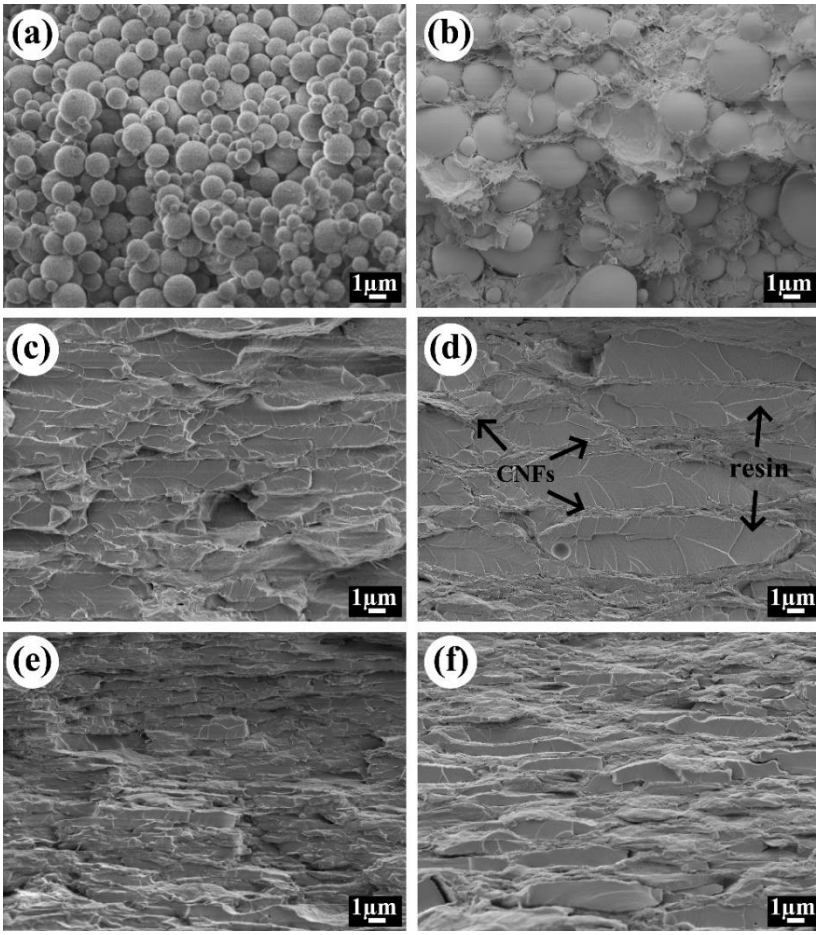

Figure 3.4. FE-SEM images of the dehydrated and UV-cured Pickering emulsion of (a) PE3 and (b) PE10. Fracture surfaces of the mats of (c) PE3 and (d) PE10. Fracture surfaces of (e) PE4 and (f) PE18 nanocomposites prepared by hot-pressing from PE3 and PE10 emulsions, respectively.

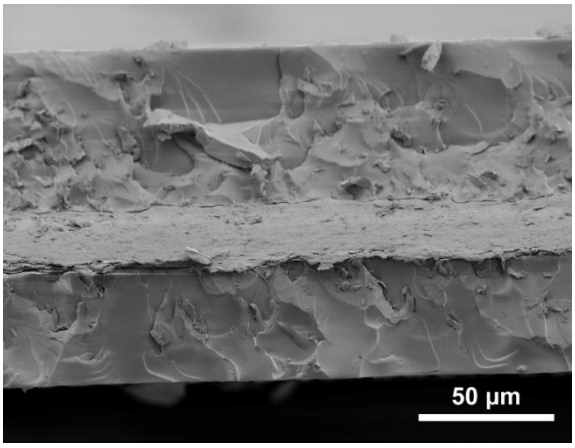

Figure 3.5. Fracture surface of the IM composite with the sandwiched CNF-nanopaper (20 wt% CNF-content).

3.3.2. Optical transparency of the nanocomposites

The effect of the CNF-content on the optical transparency of the nanocomposites are shown in Figure 3.6a,b, and the appearance of the nanocomposites before and after hot-pressing are compared in Figure 3.6c,d, respectively. The PE4 mats before hot-pressing showed low linear light transmittance of 48.9% at 600 nm. The linear transmittance decreased markedly to 6.4% as the CNFs content was increased to 25 wt%. This poor transparency at high CNF-content was attributed to the high light-scattering from the CNF-network-droplet interfaces, as shown in Figure 3.4d. The optical transmittance was changed markedly when the nanocomposite mats were hot-pressed, as shown in Figure 3.6d. At 4 wt% CNF-content, a total light transmittance of 91.5% (600 nm), which is close to that of neat acrylic film (92.4%), and a linear transmittance of 86% (600 nm) were obtained. The linear transmittance of the PE25 nanocomposite was improved to 85% (600 nm) from 6.4% after hot-pressing. This high change in linear transmittance from 48.9% to 86% for PE4 and from 6.4% to 85% for PE25 was attributed to the fact that the resin was penetrated into the surrounding CNF-network during hot-pressing, thereby, the refractive index difference between the CNFs and matrix was minimized.

In the IM nanocomposites, greater degradation of the transparency was observed at a high CNF loading. For example, the linear transmittance of IM15 was 85% (600 nm), which was reduced to 80.4% (600 nm) when 26 wt% CNFs (IM26) was used. In contrast, the linear transmittance of the PE25 nanocomposite was only degraded by 1% compared to the PE4 nanocomposite (from 86 to 85%). Although the reason for maintaining a high transparency in the PE nanocomposites is unclear, but definitely, their unique hierarchical microstructure had played an important role. A possible reason could the uniform distribution of the CNF-network throughout the PE nanocomposites (Fig. 3.4 e,f), whereas, the dense CNF-nanopaper was laid sandwiched between outer thick resin layers in the IM composites (Fig. 3.5). Moreover, compared with a previous work on the resin-impregnated BC nanofibers composites with a nanofiber content of 5 wt% [16], the PE25 nanocomposites showed higher transparency despite having a high CNFs content. These results indicate the advantages of the Pickering emulsion method in terms of the transparency of the CNF-reinforced nanocomposites.

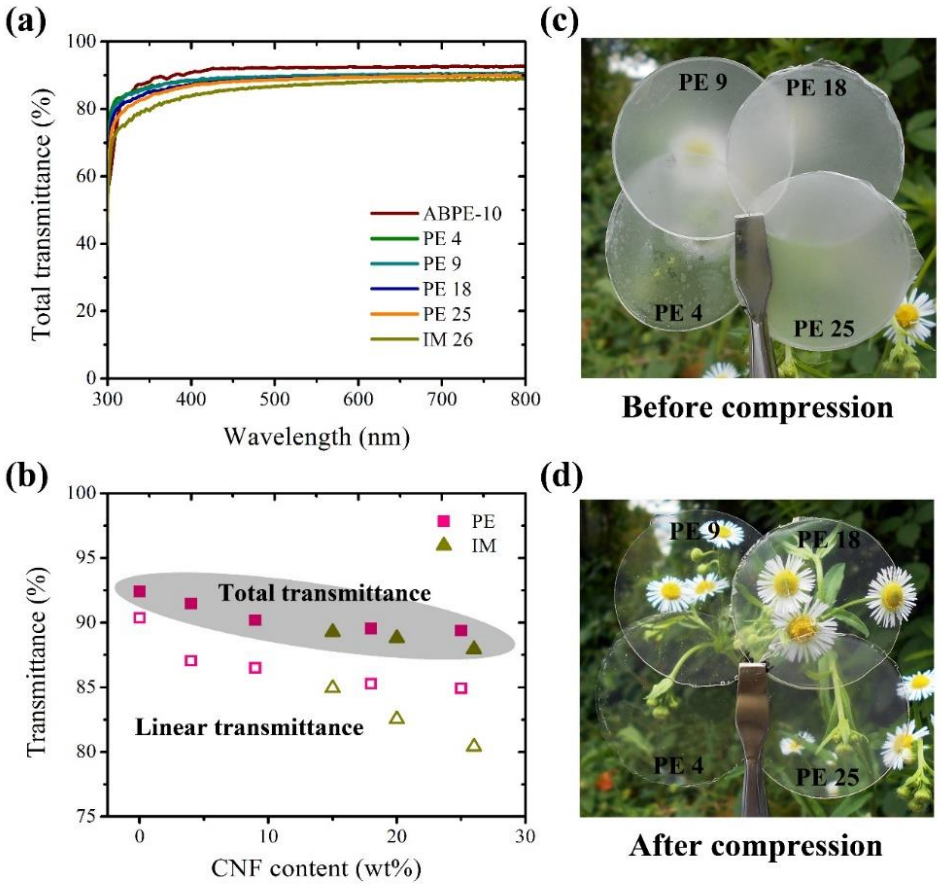

Figure 3.6. (a) Total transmittance spectra of the CNF-reinforced nanocomposites, (b) total and linear transmittance values at 600 nm with respect to CNF contents. Appearance of the nanocomposites with different CNFs contents (c) before and (d) after hot-pressing.

3.3.3. Mechanical properties of the nanocomposites

Tensile stress-strain curves of the nanocomposites are shown in Figure 3.7 and the tensile properties are summarized in Table 3.1. It has been widely reported that the increase in tensile strength and modulus is usually accompanied by a decrease in strain-to-failure for the polymer composites reinforced with cellulose particles owing to the poor compatibility or debonding between the cellulose and polymer matrix. Moreover, cellulose aggregation is the main cause of the decreased mechanical properties at a high concentration of the cellulose particles [2,17−23]. However, the hierarchically self-structured PE nanocomposites showed good mechanical properties with improved stain-to-failure even at a high CNFs content. At 4 wt% CNFs, the tensile modulus and strength were respectively 19.5 and 9.7 times as great as that of the neat resin films. Remarkably, the strain-to-failure and toughness of the PE4 composites were respectively 2 and 21.8 times as high as that of the neat resin films. This considerable

improvement in the mechanical properties can be attributed to the hierarchical CNF-network in the nanocomposites, which allowed stress to efficiently transfer from the soft resin platelets to the CNF-network, and could limit and/or delay crack initiation and growth by crack deflection, delamination, and bridging by microcrack formation accompanied with energy dissipation by mutual sliding of the CNF-encapsulated platelets during the deformation [24]. The effect of this synergistic mechanism on the mechanical performance of the PE nanocomposite was maintained as the CNFs content was increased, as shown in Figure 3.7 and Table 3.1. A great improvement in strength and modulus by 18.3 and 48.7 times compared to the neat resin was recorded for PE25. Intriguingly, the strain-to-failure of the PE25 nanocomposite was 1.5 times as great as that of the neat resin films. As a combined result, the toughness of the PE25 nanocomposite increased to 2.9 MJ m^{-3} from 0.08 MJ m^{-3}, which is 38 times as great as that of the neat resin films. Therefore, the synergistic hierarchical structure in the PE nanocomposites obtained from Pickering emulsion method offers tunability of mechanical properties by varying the CNF-content without compromising the strain-to-failure of the resin/polymer.

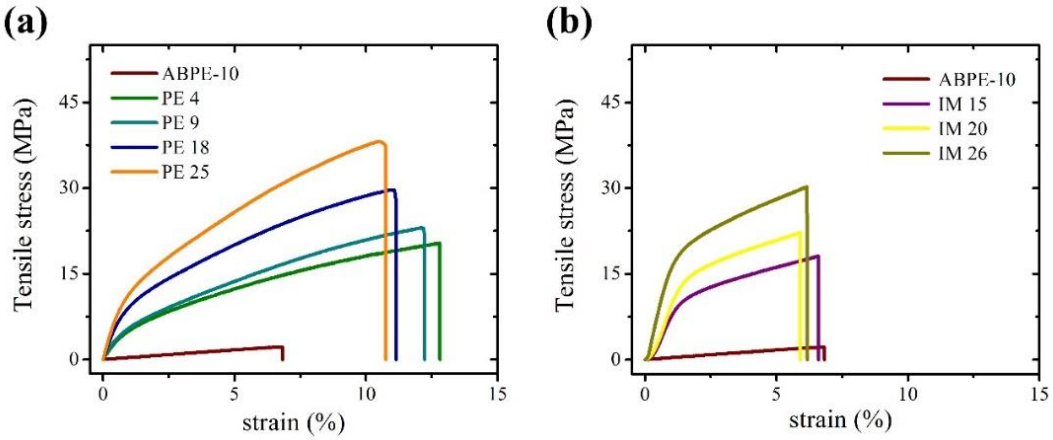

Figure 3.7. Tensile tress-strain curves of the CNF-reinforced nanocomposites prepared by (a) Pickering emulsification method and (b) impregnation method.

The mechanical performances of the nanocomposites prepared by the Pickering emulsion method and the impregnation method were also compared. Similar to the results discussed in Chapter 2, a high tensile strength, strain-to-failure, and toughness at a similar content of CNFs were observed for PE nanocomposites, whereas, a high modulus was obtained for the IM composites. The reason of this stiffer behavior of the IM composites was attributed to the stiff CNF-nanopaper, which mainly controlled the mechanical behavior of the IM composites. The lower modulus of the PE nanocomposites than that of the IM composites became less

noticeable when a higher content of CNFs were introduced, owing to the thicker network formation among the resin platelets.

The mechanical result confirms the advantage of Pickering emulsion method to obtain highly transparent, highly flexible nanocomposites with superior mechanical properties compared with the time-consuming impregnation method.

Table 3.1. Values of tensile strength, young's modulus, tensile strain and toughness for the nanocomposites with varying CNF-contents prepared by the Pickering emulsification method and impregnation method.

Materials	Tensile strength (MPa)	Young's modulus (GPa)	Tensile strain (%)	Toughness (MJ m^{-3})
ABPE-10	2.2 ± 0.5	0.03 ± 0.01	7.0 ± 1.6	0.08 ± 0.03
PE 4	21.3 ± 1.2	0.66 ± 0.09	12.7 ± 1.7	1.8 ± 0.3
PE 9	22.0 ± 1.0	0.68 ± 0.04	13.4 ± 1.7	1.9 ± 0.3
PE 18	29.2 ± 1.0	1.2 ± 0.1	11.0 ± 0.8	2.2 ± 0.2
PE 25	41.0 ± 2.6	1.7 ± 0.2	10.6 ± 0.9	2.9 ± 0.2
IM 15	17.9 ± 4.3	1.2 ± 0.2	5.1 ± 1.0	0.6 ± 0.2
IM 20	22.8 ± 2.2	1.5 ± 0.2	5.4 ± 0.9	0.9 ± 0.2
IM 26	32.3 ± 2.3	2.1 ± 0.2	6.4 ± 0.5	1.5 ± 0.1
CNF nanopaper	140.2 ± 10.8	8.6 ± 0.3	10.3 ± 2.0	11.2 ± 3.1

3.3.4. Thermal stability of the nanocomposites

Low thermal expansion is an attractive property of the CNF-reinforced nanocomposites, as well as optical transparency and flexibility, to enable use in the electronic devices. Fig. 3.8 shows the thermal expansion curves and the corresponding CTE values of the nanocomposites as a function of the CNFs content. The CTE of the neat acrylic resin was 192.3 ppm K^{-1}, which decreased to 15.6 ppm K^{-1} on addition of the CNFs at a content as low as 4 wt%. Taking into account the similarity of the structures observed in the resin-impregnated BC pellicles [16] and

the PE nanocomposites, the considerable reduction in CTE can be attributed to the randomly oriented in-plane network of rigid and low-thermal-expansion CNFs, which suppressed the thermal expansion of the resin in planar directions [16]. At CNF contents greater than 4 wt%, the CTE value of the nanocomposites decreased gradually. Nanocomposites with a CNF content of 25 wt% exhibited a value of 7.3 ppm K^{-1}, which is similar that of glass substrates (7–10 ppm K^{-1}) [25].

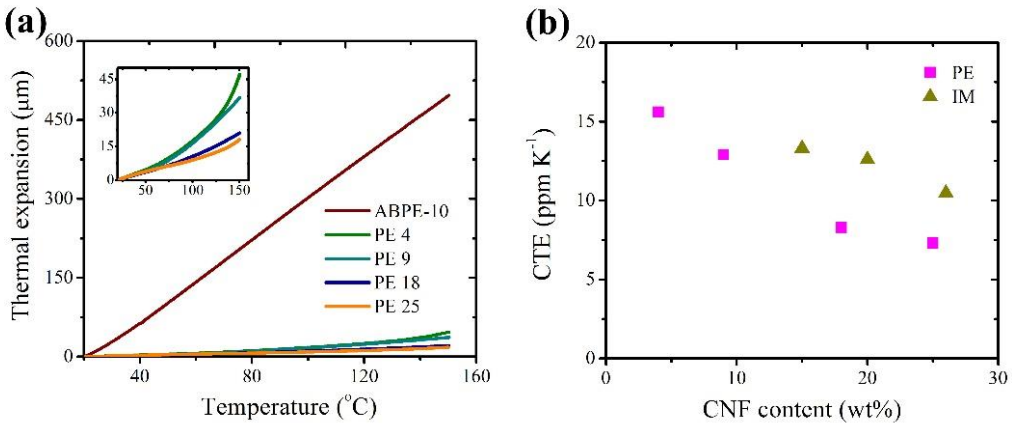

Figure 3.8. (a) Thermal expansion curves of the hierarchical CNF-reinforced nanocomposites, and (b) corresponding CTE of the nanocomposites prepared by the Pickering emulsification method and impregnation method.

Notably, the CTE of the IM nanocomposites was higher than that of the PE nanocomposites at the similar CNFs content (Fig. 3.8b). This result is in sharp contrast with the result presented in Chapter 2. This was probably due to the high modulus of the IM nanocomposite (2.85 GPa @ 20 wt% CNFs content) presented in Chapter 2 compared to that of the IM nanocomposites presented here (1.5 GPa @ 20 wt% CNFs content). This variation in modulus was resulted from different pressing pressure used to prepare CNF-nanopaper (2 MPa versus 0.1 MPa). It has been reported that there is a negative relationship exist between the thermal expansion and Young's modulus of a composite material [26]. Also, in this work, both PE nanocomposites and IM nanocomposites presented a good linear correlation between the CTE and inverse-Young's-modulus (Fig. 3.9). However, interestingly, the less-stiff PE nanocomposites had a lower CTE than that of the IM nanocomposites (Fig. 3.8b and Fig. 3.9). To obtain a similar thermal dimensional stability, the PE nanocomposites required a CNF-content as low as 9 wt%, whereas, 20 wt% CNFs was required for the IM nanocomposites. Two reasons for this behavior can be proposed: 1) the thermal expansion of the PE

nanocomposites was highly anisotropic, meaning that they expanded enormously in the thickness direction because of the horizontal in-plane orientation of the CNF-network and the resin platelets, which accommodated the thermal expansion occurred in the planar direction [16], and 2) the use of low pressing pressure (0.1 MPa) to prepare CNF-nanopaper; the less compact CNF-nanopaper could not effectively restrict the thermo-mechanical stresses generated in the resin (to be noted that the CNF-nanopaper mainly govern the mechanical behavior of the IM nanocomposites). The high thermal expansion in the thickness direction of the PE nanocomposites is not significant in terms of their practical applications because of their thinness, e.g., ~100–200 μm [16].

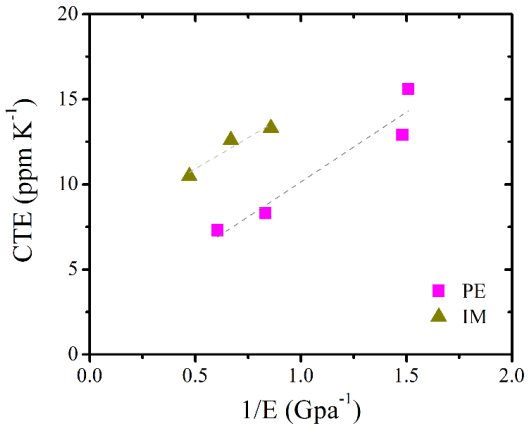

Figure 3.9. Relationship between thermal expansion and inverse of the Young's modulus of the nanocomposites prepared by Pickering emulsion method and impregnation method.

Although the thermal-dimensional stability of the PE nanocomposites was extraordinarily high, but the thermal degradability of the PE nanocomposites was increased with the addition of CNFs (Fig. 3.10). However, no thermal degradation of the PE nanocomposites was observed until 210 °C. Therefore, this should not limit the potential application of the high-performance, highly transparent PE nanocomposites up to 200 °C.

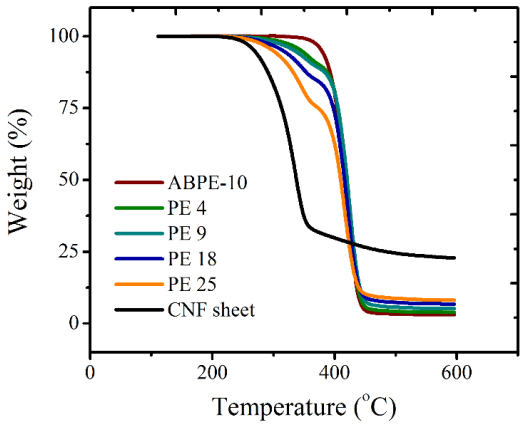

Figure 3.10. Thermograms of the nanocomposites prepared by Pickering emulsification method with respect to CNF-content and in comparison with the neat acrylic resin and CNF-nanopaper.

3.4 Summary

The Pickering emulsification process allowed to obtain a nanocomposite with a synergistic hierarchical structure that yielded an anomalous but desirable combination of high strength, modulus, and toughness with an improved elongation ability even at a CNF-content as high as 25 wt%. Therefore, this advantage provides an opportunity to tune the strength, stiffness, and toughness of the PE nanocomposites by adjusting the CNF-content up to 25 wt% without compromising the mechanical flexibility of the nanocomposites. The PE nanocomposites also had a high optical transparency compared to the IM nanocomposites. Another advantage is that the optical transparency of the PE nanocomposites was free from the effect of CNF-content, i.e., the transparency remained stable with a CNF-loading ranging from 4–25 wt%. This was due to the uniform distribution of the hierarchical CNF-network throughout the PE nanocomposites. The PE nanocomposites also possessed a high thermal-dimensional stability (CTE similar to that of glass at an 18–25 wt% CNF-reinforcement) compared to the IM nanocomposites owing to their distinctive microstructure having a horizontal in-plane orientation of the CNF-network and the resin platelets.

3.5 References

1. Okahisa Y., Yoshida A., Miyaguchi S., and Yano H. Optically transparent wood–cellulose nanocomposite as a base substrate for flexible organic light-emitting diode displays. Compossites Science and Technology, 2009, **69**, 1958–1961.
2. Suzuki K., Homma Y., Igarashi Y., Okumura H., and Yano H. Effect of preparation process of microfibrillated cellulose-reinforced polypropylene upon dispersion and mechanical properties. Cellulose, 2017, **24**, 3789–3801.
3. Suzuki K., Homma Y., Igarashi Y., Okumura H., Semba T., Nakatsubo F., and Yano H. Investigation of the mechanism and effectiveness of cationic polymer as a compatibilizer in microfibrillated cellulosereinforced polyolefins. Cellulose, 2016, **23**, 623–635.
4. Fujisawa S, Togawa E, Kuroda K. Facile route to transparent, strong, and thermally stable nanocellulose/polymer nanocomposites from an aqueous pickering emulsion. Biomacromolecules, 2017, **18**, 266–271.
5. Ougiya H., Watanabe K., Morinaga Y., and Yoshinaga F. Emulsion-stabilizing effect of bacterial cellulose. Bioscience, Biotechnology, and Biochemistry, 1997, **61**, 1541–1545.
6. Tingaut P., Zimmermann T., and Sèbe G. Cellulose nanocrystals and microfibrillated cellulose as building blocks for the design of hierarchical functional materials. Journal of Materials Chemistry, 2012, **22**, 20105–20111.
7. Madivala B., Vandebril S., Fransaer J., and Vermant J. Exploiting particle shape in solid stabilized emulsions. Soft Matter, 2009, **5**, 1717–1727.
8. Kalashnikova I., Bizot H., Bertoncini P., Cathala B., and Capron I. Cellulosic nanorods of various aspect ratios for oil in water Pickering emulsions. Soft Matter, 2013, **9**, 952–959.
9. Winuprasith T., and Suphantharika M. Microfibrillated cellulose from mangosteen (Garcinia mangostana L.) rind: Preparation, characterization, and evaluation as an emulsion stabilizer. Food Hydrocolloids, 2013, **32**, 383-394.
10. Salas C., Nypelö T., Rodriguez-Abreu C., Carrillo C., and Rojas O. J. Nanocellulose properties and applications in colloids and interfaces. Current Opinion in Colloid & Interface Science, 2014, **19**, 383–396.
11. Xhanari K., Syverud K., Chinga-Carrasco G., Paso K., and Stenius P. Structure of nanofibrillated cellulose layers at the O/W interface. Journal of Colloid and Interface Science, 2011, **356**, 58–62.

12. Lee K. -Y, Blaker J. J., Murakami R., Heng J. Y. Y., and Bismarck A. Phase behavior of medium and high internal phase water-in-oil emulsions stabilized solely by hydrophobized bacterial cellulose nanofibrils. Langmuir, 2014, **30**, 452–460.
13. Cunha A. G., Mougel J. –B., Cathala B., Berglund L. A., and Capron I. Preparation of double Pickering emulsions stabilized by chemically tailored nanocelluloses. Langmuir 2014, **30**, 9327−9335.
14. Rojas O. J. Nanocellulose in the formulation of emulsions and formulation-composition maps. TAPPI Webinar, April 14, 2016.
15. Bai L., Huan S., Xiang W., and Rojas O. J. Pickering emulsions by combining cellulose nanofibrils and nanocrystals: phase behavior and depletion stabilization. Green Chemistry, 2018, **20**, 1571–1582.
16. Nogi M., and Yano H. Transparent nanocomposites based on cellulose produced by bacteria offer potential innovation in the electronics device industry. Advanced Materials, 2008, **20**, 1849–1852.
17. Jonoobi M., Harun J., Mathew A. P., and Oksman K. Mechanical properties of cellulose nanofiber (CNF) reinforced polylactic acid (PLA) prepared by twin screw extrusion. Composites Scienece and Technology, 2010, **70**, 1742–1747.
18. Zhao J., He X., Wang Y., Zhang W., Zhang X., Deng Y., and Lu C. Reinforcement of all-cellulose nanocomposite films using native cellulose nanofibrils. Carbohydrate Polymers, 2014, **104**, 143–150.
19. Tanpichai S., and Oksman K. Crosslinked poly(vinyl alcohol) composite films with cellulose nanocrystals: Mechanical and thermal properties. Journal of Applied Polymer Science, 2018, **135**, 45710.
20. Yuwawech K., Wootthikanokkhan J., and Tanpichai S. Effects of two different cellulose nanofiber types on properties of poly(vinyl alcohol) composite films. Journal of Nanomaterials, 2015, **2015**, 908689.
21. Sato A., Kabusaki D., Okumura H., Nakatani T., Nakatsubo F., and Yano H. Surface modification of cellulose nanofibers with alkenyl succinic anhydride for high-density polyethylene reinforcement. Composites Part A: Applied Science and Manufacturing, 2016, **83**, 72–79.
22. Yano H., Omura H., Honma Y., Okumura H., Sano H., and Nakatsubo F. Designing cellulose nanofiber surface for high density polyethylene reinforcement. Cellulose, 2018, **25**, 3351–3362.

23. Tanpichai S. A comparative study of nanofibrillated cellulose and microcrystalline cellulose as reinforcements in all-cellulose composites. Journal of Metals, Materials and Minerals, 2018, **28**, 10–15.
24. Kakisawa H., and Sumitomo T. The toughening mechanism of nacre and structural materials inspired by nacre. Science and Technology of Advanced Materials, 2011, **12**, 064710.
25. Ashby, M. F. Materials Selection in Mechanical Design. Pergamon Press: Oxford, 1992.
26. Nakagaito A. N., and Yano H. The effect of fiber content on the mechanical and thermal expansion properties of biocomposites based on microfibrillated cellulose. Cellulose, 2008, **15**, 555–559.

Chapter 4
Effect of Length and Crystallinity of the Nanocelluloses on the Microstructure and Properties of the Nanocomposites

4.1 Introduction

Improving the thermal stability of the transparent plastics is of significant importance in terms of their practical application. Most plastics lose stiffness drastically, sometimes an order of magnitude, when heated from room temperature to ~100–150 °C. Another drawback of plastics is that they have very low thermal dimensional stability, and their coefficient of thermal expansion (CTE) often exceeds 200 ppm K^{-1} [1]. This high CTE causes problems in devices at high temperature during both the fabrication processes (often requiring temperatures >100 °C) and operation. This can not only lead to detrimental mechanical stresses between the functional materials (e.g., silicon crystals, CTE = ~3 ppm K^{-1}) and the substrate owing to a very large CTE mismatch [2], but also the nano/microscale surface features can also easily become deformed or damaged, which can cause attenuation of the device performance. For example, a decreased light extraction from an OLED has been observed owing to fabrication-induced damage in the nanopatterned substrate [3]. The optical clarity of plastics also decreases with heating [4].

The thermal properties of plastics can be improved by incorporating micro/nanofillers, such as silica, alumina, boron nitride, diamond, zinc sulfide, zirconium tungstate, carbon nanotube, and clays [5–10]. However, high loading (>50 wt%) of these inorganic fillers is usually required to achieve satisfactory thermal stability, which often renders the plastic relatively brittle and/or optically inferior. In this context, strong CNFs, which are ~0.1 to >2-μm-long and ~5–60-nm-diameter “semicrystalline” fibers extracted from plants [11], have attracted great attention as a nanofiller to improve the mechanical and thermal performances of plastics without decreasing the transparency [1,12,13]. Because, the “crystalline” moieties (~50–90%) of the semicrystalline CNFs have an incredibly high Young’s modulus (E) of ~140 GPa, a very low CTE of ~0.1 ppm K^{-1}, and a high thermal and chemical durability [14–16].

In Chapter 2 and Chapter 3, using “semicrystalline” long CNFs, optically transparent hierarchical nanocomposites were fabricated by a facile Pickering emulsification method (PE nanocomposites) that have high strength, toughness, and 3D-moldability compared with their counterparts prepared by the impregnation method (IM composites). Interestingly, even with a CNF-content as high as 25 wt%, the strain-to-failure of the PE nanocomposites was almost double compared to that of neat resin, because of having a synergistic self-assembled hierarchical architecture. The PE nanocomposites also showed a CTE of 7.3 ppm K^{-1} (27 times lower than that of the resin used and similar to that of glass) with a CNF-content of 25 wt%.

Therefore, considering the extremely high modulus and drastically low CTE of the “crystalline” parts of the CNFs (i.e., cellulose nanocrystals (CNCs) or cellulose nanorods (CNs)), it was hypothesized that the use of CNs would generate much more thermomechanically strong and thermal-dimensionally stable nanocomposites at a low nanocelluloses fraction. A substrate with a high thermal-dimensional stability, i.e., with a low CTE of ~3 ppm K^{-1}, similar to that of semiconducting silicon crystals, would be preferred for device fabrication.

Furthermore, Kalashnikova et al. reported that the long high-aspect-ratio CNFs (length: ~4 μm; aspect ratio: ~160) promote the formation of loose but interconnected network in the hexadecane oil-in-water Pickering emulsion (Fig. 1.15 in Chapter 1) [17]. Whereas, the short low-aspect ratio CNs (length: ~189 nm; aspect ratio: 13) promote the formation of individual oil droplets encapsulated with a dense network. Therefore, the use of nanocelluloses having different lengths to stabilize the resin-in-water Pickering emulsifications may provide an opportunity to synergistically tune the properties of the transparent nanocomposites at a same nanocelluloses content.

Therefore, in this part of the study, CNFs were acid-hydrolyzed to obtain CNs of different lengths and crystallinities, and then the acrylic resin-in-water Pickering emulsions were formed using them to subsequently obtain transparent hierarchical nanocomposites. The thermal stability of the nanocomposites in terms of the thermomechanical, thermal-dimensional, and thermo-optical properties were investigated. The thermal-dimensional stability of a microlens-array (μLA) prepared on the surface of the nanocomposite was also demonstrated.

4.2 Materials and method

4.2.1. Materials

Sugarcane bagasse was kindly supplied by Eastern Sugar & Cane Co., Ltd., Thailand. ABPE-10 monomer (reflective index = 1.516, T_g = −12 °C) was provided by Shin-Nakamura Chemical, Japan. The UV photoinitiator 2-hydroxy-2-methylpropiophenone (Wako), $NaClO_2$ (Sigma-Aldrich), KOH (Wako), acetic acid (Wako), and HCl (Wako) were used as received. The photoinitiator (0.25% w/w) was mixed with the monomer before use.

4.2.2. Preparation of CNs with varying length and crystallinity

First, long CNFs were prepared following the procedure described in Chapter 3. Highly crystalline short CNs were obtained by hydrolyzing CNFs using 2 N HCl. The hydrolysis temperatures and times to obtain CNs with different lengths and crystallinities were 50 °C and 2 h, 70 °C and 2 h, and 70 °C and 4 h, respectively. The hydrolyzed CNs were then washed by centrifugation until neutral and dialyzed in running water for 2 days. Depending on the length of the CNs, they were named as CN4K, CN1K, CN400, and CN300. For example, CN4K means that the nanocelluloses were ~4542 nm long, therefore, they can be considered as CNFs. Accordingly, CN400 and CN300 were composed of nanocelluloses of ~366 nm and ~341 nm in length, therefore, they can be considered as CNCs.

4.2.3. Preparation of transparent nanocomposites

The transparent nanocomposites reinforced with the nanocelluloses of different length and crystallinity were prepared following the procedure described in Chapter 3. For preparing surface micropatterned nanocomposite, the procedure described in Chapter 2 was followed. Notably, when the nanocellulose/resin mat containing long CNs (CN4K) was hot-pressed, a loss of resin was detected (also noted in Chapter 2 and Chapter 3). However, for CN1K, CN400, and CN300, no or negligible loss of resin was detected during hot-pressing. Therefore, the amount of long CN4K was adjusted accordingly during the emulsion preparation in order to obtain transparent nanocomposites having a nanocellulose-content (~10 wt%) similar to those of nanocomposites reinforced by CN1K, CN400, and CN300. Briefly, 0.2 g CN4K and 0.4 g CN1K, CN400, and CN300 were mixed with acrylic monomer of 3.8 g for CN4K and 3.6 g for CN1K, CN400, and CN300. The water content in all the emulsions was same at 196 g.

4.2.4. Determination of nanocellulose-content by TGA analysis

The TGA analysis was done according to the procedure described in Chapter 2 and Chapter 3. The residue-content obtained from a known composition of CN/resin mixture was used to obtain the regression equations (Fig. 4.1 and Table 4.1). Then, the residue-content of the nanocomposites were used in the equations to estimate the final CN-content in the nanocomposites.

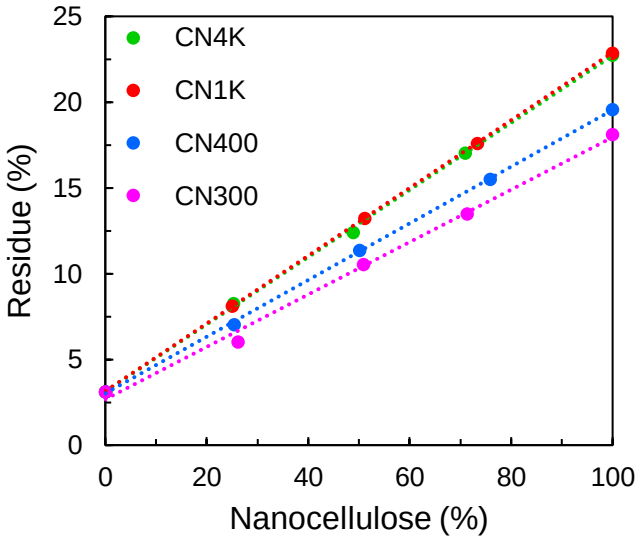

Figure 4.1. TGA-residue versus CNs graph obtained from the mixture of a known composition of dried CNs and cured resin.

Table 4.1. The regression equations obtained from the graphs presented in Figure 4.1.

	Regression equation	R^2 value
CN4K	y = 0.1958x + 3.1287	0.9996
CN1K	y = 0.1975x + 3.1464	1
CN400	y = 0.1652x + 3.018	0.9997
CN300	y = 0.1528x + 2.6724	0.9954

4.2.5. Characterizations

The FE-SEM imaging, light transmittance measurement, tensile mechanical testing, XRD analysis, and thermal expansion analysis were done according to the procedure described in Chapter 2 and Chapter 3.

The thermomechanical properties were determined with a dynamic thermo mechanical analyzer (DMS 6100, Seiko Instruments). The 5-mm-wide samples were analyzed in a N_2 atmosphere from −50 to 150 °C at a ramp of 2 °C min^{-1} in tension mode with a span of 20 mm, amplitude of 10 μm, frequency of 1 Hz, and preload force of 0.1 N.

To measure the thermo-optical properties, the samples were heated at 180 °C on a hot plate and the optical transmittance was measured every 30 min with the U-4100 spectrophotometer over a period of 120 min.

To demonstrate the thermal-dimensional stability of the µLA prepared on the surface of the nanocomposite, a custom-designed experiment was setup as shown in Figure 4.2. A thermal imaging camera (FLIR E6, FLIR Systems) was used to monitor the real-time temperature of the µLA during the thermal stability tests by laser-beam diffraction.

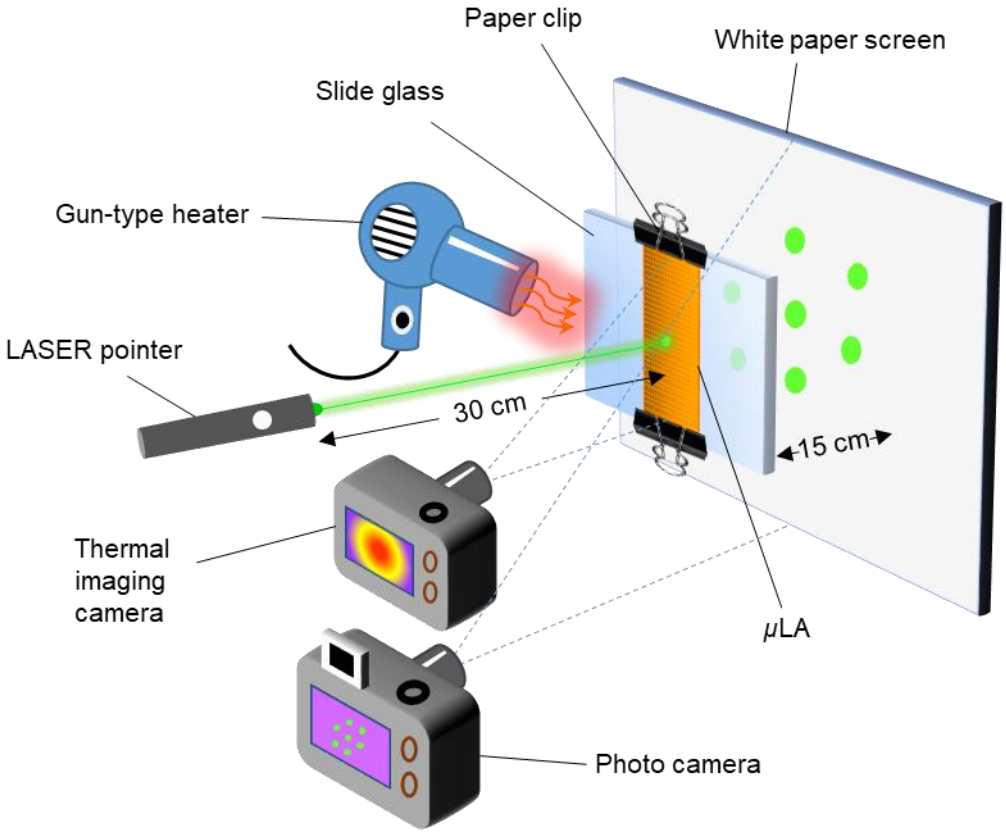

Figure 4.2. Experimental setup for thermal stability test of the µLA on the surface of the transparent nanocomposite.

4.3 Results and discussion

4.3.1. Characterization of CNs

Sugarcane bagasse pulp was used as the raw material for CN preparation. The bagasse was chemically purified by a series of acidified sodium chlorite ($NaClO_2$) and potassium hydroxide (KOH) treatments to remove the matrix lignin and hemicelluloses. The purified pulp fibers (crystallinity 81%) were then mechanically disintegrated into individual long semicrystalline CNFs (length 4542 ± 690 nm, crystallinity 70%, CN4K) by passing them twice through a grinder in a water medium (Fig. 4.3). The decrease in the crystallinity was probably because of damage of the cellulose crystals during the mechanical action [18]. The amorphous parts of semicrystalline CN4K were chemically cleaved by hydrochloric acid (HCl, 2 N) hydrolysis to produce nanocrystals/nanorods (Fig.4.3). Three types of hydrolyzed CNs with decreasing length and increasing crystallinity were produced by modifying the hydrolysis time and temperature (Fig. 4.3): 1278 ± 1029 nm long/73% crystallinity (CN1K), 366 ± 142 nm long/76% crystallinity (CN400), and 341 ± 94 nm long/79% crystallinity (CN300). Thus, short but highly crystalline CNs were successfully obtained. However, the crystallinities were little lower compared to the crystallinities (77–86%) reported by Oliveira et al. [19]. In their work, the CNs were produced directly from the sugarcane bagasse fibers by treating with 65 wt% sulfuric acid (H_2SO_4). The width of CN4K was 20 ± 6 nm and the width of all the hydrolyzed CNs was 18 nm (CN1K: 18 ± 4 nm, CN400: 18 ± 4 nm, and CN300: 18 ± 3 nm).

4.3.2. Optically transparent nanocomposites from Pickering emulsions

The CN/water slurry was mixed with liquid acrylic resin monomer and vigorously agitated to obtain a resin-in-water emulsion stabilized by CNs (Fig. 4.4). The average diameter of the resin droplets was ~2 μm for all of the emulsions. FE-SEM images revealed that the droplets were encapsulated by the CN network, thereby preventing their coalescence (Fig. 4.4). By taking advantage of the nanocellulose network, Svagan et al. encapsulated optically functional molecules contained in hexadecane oil to prepare a photon energy upconverting material and Li et al. encapsulated paraffin to prepare a thermal regulation nanocomposite [20,21]. In this study, the emulsions were easily dehydrated by vacuum filtration and drying (40 °C) without any apparent resin leakage owing to the protecting CN network. The obtained translucent CN/resin mats were then hot compressed (2 MPa, 150 °C) to obtain nanocomposites with a high optical transmittance of ~90% in the wavelength range 400–800 nm (Fig. 4.5).

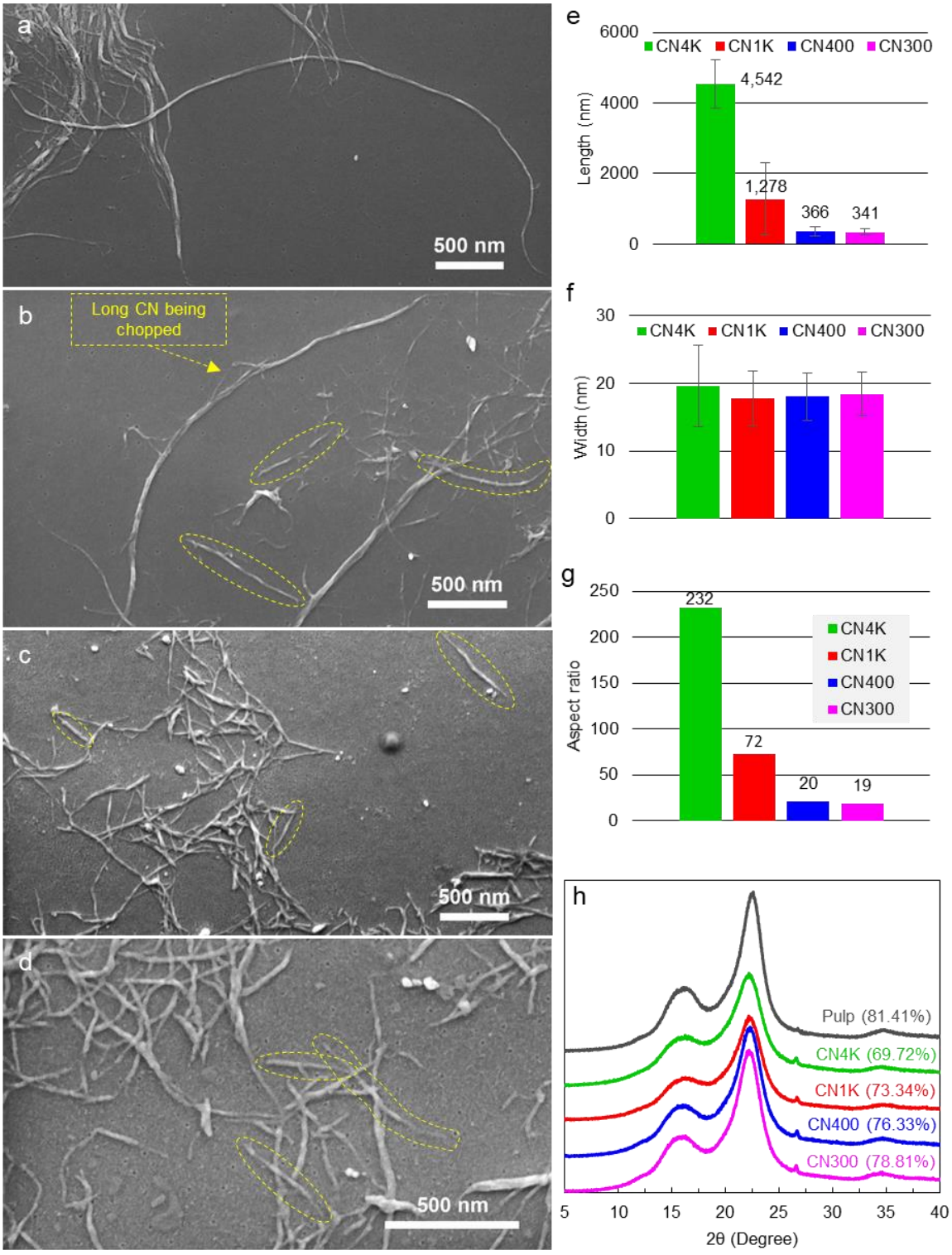

Figure 4.3. FE-SEM images of (a) CN4K, (b) CN1K, (c) CN400 and (d) CN300. (e) Length of the CNs. (f) Width of CNs. The error bars in (e) and (f) indicate standard deviation. The FE-SEM image of CN1K in (b) and the length in (e) indicate that the mild hydrolysis condition (2 h, 50 °C) produced a combination of long and short CNs. (g) Aspect ratio of CNs. (h) XRD patterns of CNs with their corresponding crystallinity.

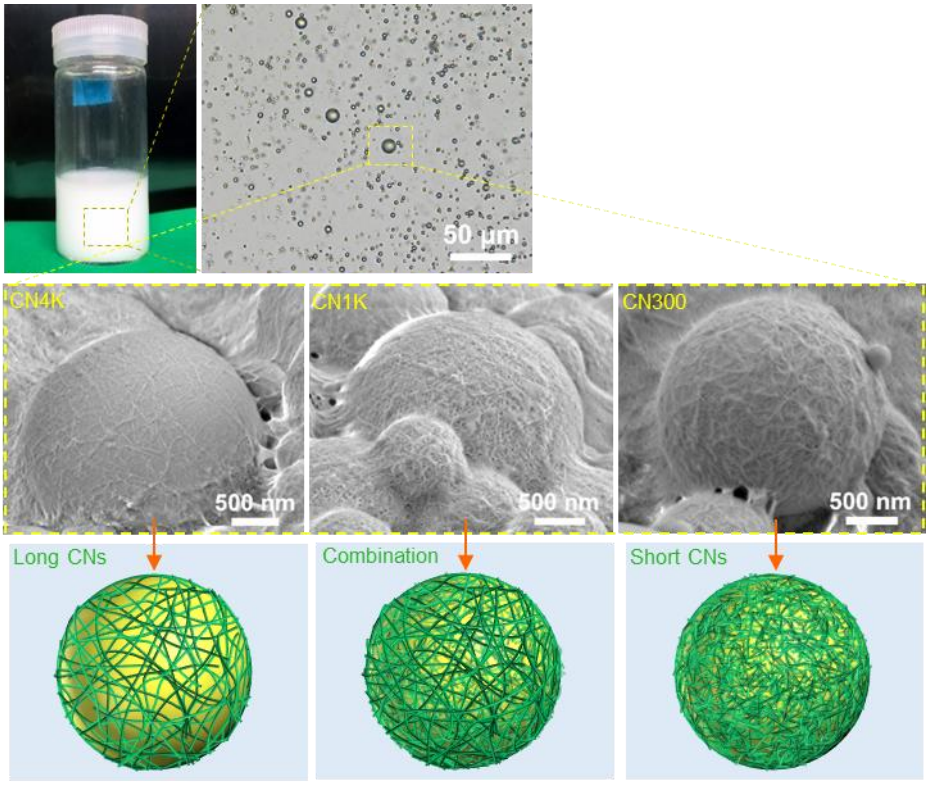

Figure 4.4. The photograph and digital microscope images of Pickering-stabilized resin-in-water emulsion together with the FE-SEM images showing that the resin droplets were encapsulated by the CN network. The long CN4K produced a loose mesh-like network. Whereas, CN1K (combination of long and short CNs) and CN400/300 (short CNs) produced a dense network.

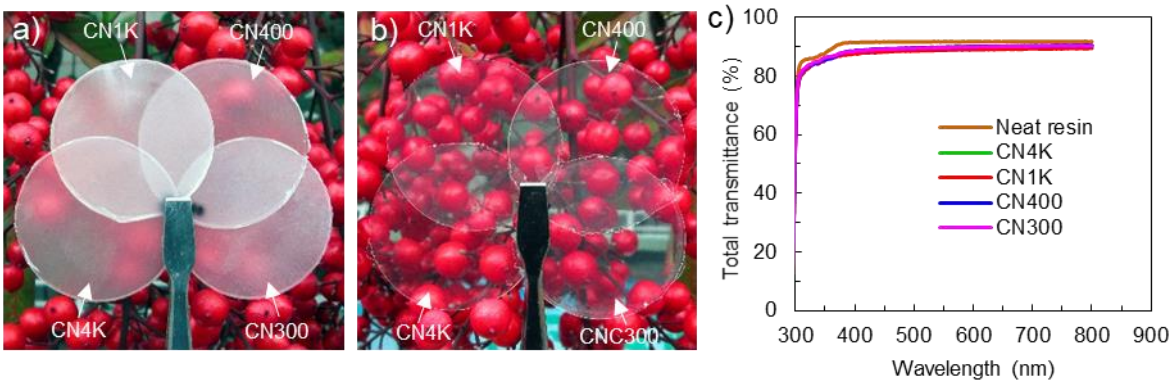

Figure 4.5. (a) Self-standing CN/resin mats containing liquid resin droplets. (b) Highly transparent nanocomposites obtained after hot compressing the mats. (c) Total optical transmittances of the nanocomposites (~125–200 μm thick). The transmittances were normalized to 100 μm thickness to eliminate the effect of the thickness variation (please see Chapter 2 for more details on transparency normalization).

The evolution of the transparency and microstructural hierarchy of the nanocomposites is shown in Figure 4.6a, which was supported by the FE-SEM images of the fracture surface of the mat and the transparent nanocomposite (Fig. 4.6b,c, respectively). The spherical resin droplets in the emulsion became oval-shaped in the mat owing to the vacuum suction pressure. During hot compression, the oval droplets were flattened to platelets and their surrounding CN network (CN shell) was infiltrated by the resin (composite shell) to form a continuous matrix. Therefore, refractive index variation and scattering at the interfaces were minimized, which led to the nanocomposites having high optical clarity. There was no significant effect of different CNs on the total transmittance of the nanocomposites (Fig. 4.5c). For the structural hierarchy, the submicrometer-thick CN network around the submicrometer–micrometer-thick resin platelets was the first order of the hierarchy (Fig. 4.6, also see Fig. 4.4). The second order of the structural hierarchy was the micrometer–millimeter scale CN network formed by interconnection and stacking of the numerous CN-encapsulated resin platelets in the bulk composite structure (Fig. 4.6).

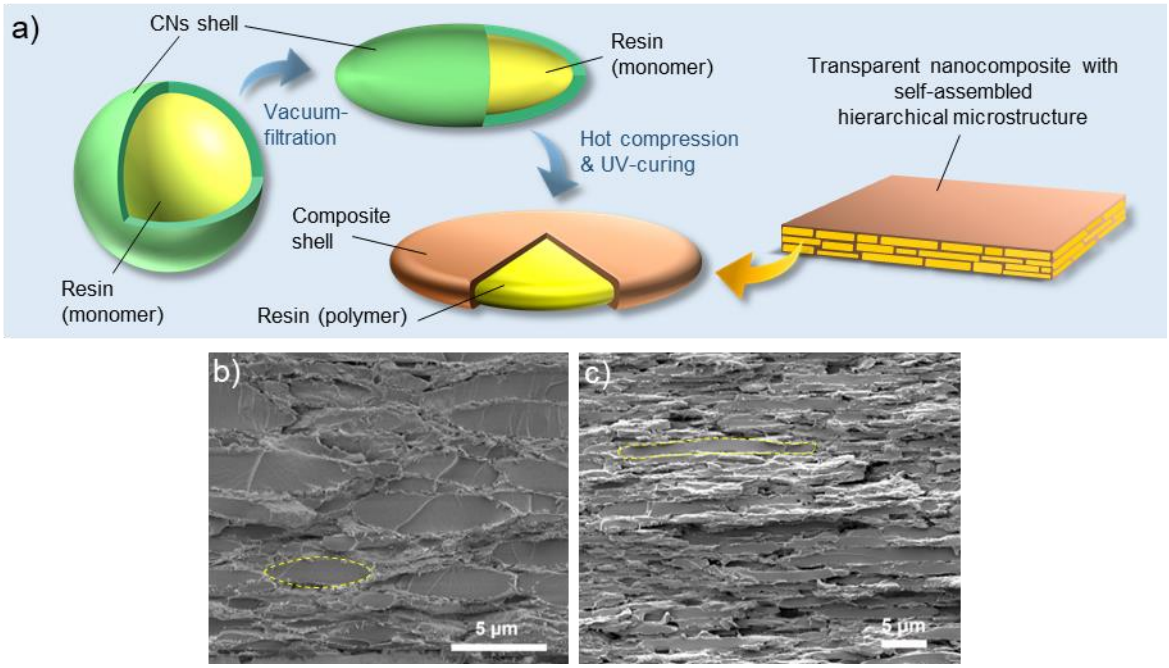

Figure 4.6. (a) Schematic of evolution of the transparency and self-assembled hierarchical microstructure. (b) FE-SEM image of the fracture surface of a CN/resin mat showing the oval-shaped resin droplets (highlighted by the yellow dashed line). (c) FE-SEM image of the fracture surface of a transparent nanocomposite showing the platelets of the resin (highlighted by the yellow dashed line).

It should be noted that a small amount of resin was squeezed out of the CN4K mat during hot compression. This might be because a loose mesh-like network structure was formed due to the long high-aspect-ratio CN4K on the droplet surface (Fig. 4.4). In contrast, CN1K, which contained both long and short CNs (Fig. 4.3b,e), and short CN400/300 produced more dense network structures, thus prevented the resin from being squeezed out; note that the loss of resin was negligible at <0.8 wt%. A similar phenomena was also observed by Kalashnikova et al. for hexadecane oil-in-water Pickering emulsions stabilized by nanocelluloses of varying lengths (Fig. 1.15 in Chapter 1) [17]. Therefore, the amount of CN4K in the emulsion was carefully chosen to obtain transparent nanocomposites with ~10 wt% CN content.

4.3.3. Mechanical properties of the nanocomposites

The tensile stress–strain curves are shown in Figure 4.7 and the tensile stress–strain data are given in Table 4.2. The results show incorporation of the hierarchical CN network resulted in a huge improvement in the mechanical properties of the soft resin, and the different types of CNs led to different mechanical behavior even for the same CN content (~10 wt%). The strength, E, and toughness increased from 2.29 ± 0.54 MPa, 0.03 ± 0.00 GPa, and 0.09 ± 0.04 MJ m^{-3} for the neat resin to 29.39 ± 1.15 MPa, 1.20 ± 0.06 GPa, and 2.38 ± 0.18 MJ m^{-3}, respectively. Notably, the highest strength and toughness were obtained with CN1K reinforcement, whereas the E value of the CN300 nanocomposite was the highest. To shed light on the underlying reasons, the fracture surfaces of the nanocomposites after tensile tests were investigated by FE-SEM (Fig. 4.8). It was noticed that the load-bearing CN networks around the resin platelets in the CN1K and CN300 nanocomposites are thicker and more densely structured than that of CN4K (Fig 4.8 and Fig. 4.4). In addition, because CN1K was composed of both long and short CNs, the load transfer from the polymer matrix was effectively governed by both the breaking of long CNs (evident by protruded broken nanofibers, as in CN4K) and pulling out of short CNs (as in CN300) [22,23]. Furthermore, in Chapter 2 and Chapter 3, it was demonstrated that the polymer nanocomposites having a hierarchical CNF-network with a brick-and-mortar architecture show a synergistic stress-bearing, stress-dissipating, and crack-minimizing mechanism. Here, a similar synergistic hierarchical structure was successfully obtained (Fig. 4.6 and Fig. 4.8). Consequently, compared with the soft resin, the transparent nanocomposites were highly flexible (fracture strain of up to ~15% versus ~7% for the neat resin) and strong (strength of up to ~30 MPa), which led to a much higher toughness at only ~10 wt% CN content. In comparison, the strength of the thermal regulation paraffin/CNF

nanocomposite prepared by a similar process was 30 MPa at a CNF content of 28 wt% [21]. The strength and E of the nanocomposites, particularly those of the CN1K and CN300 nanocomposites, were comparable with those of typical engineering plastics, such as polyethylene terephthalate (PET) and epoxy [24]. The toughness, strength, and E of the nanocomposites were higher than and/or comparable with those of delignified-wood/epoxy transparent composites [25].

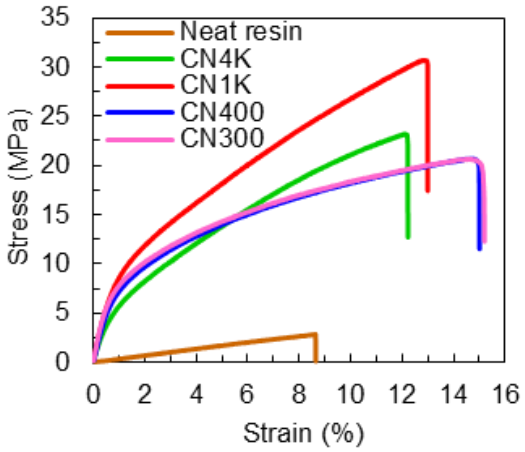

Figure 4.7. Tensile stress–strain curves of the nanocomposites at 23 °C and 50% relative humidity.

Table 4.2. Tensile stress-strain data for the nanocomposites at 23 °C and 50% relative humidity.

Sample	Strength [MPa]	E [GPa]	Toughness [MJ m^{-3}]	Strain-to-break [%]
Neat resin	2.29 (0.54)	0.03 (0.00)	0.09 (0.04)	7.00 (1.60)
CN4K	22.41 (1.06)	0.68 (0.04)	1.98 (0.27)	13.17 (1.54)
CN1K	29.39 (1.15)	1.09 (0.07)	2.38 (0.18)	12.04 (0.75)
CN400	19.28 (2.05)	1.02 (0.08)	2.35 (0.08)	14.34 (3.08)
CN300	21.01 (0.41)	1.20 (0.06)	2.32 (0.08)	14.86 (0.38)

*The values in the parenthesis represent standard deviation derived from at least 5 replications except for neat resin film (3 replications).

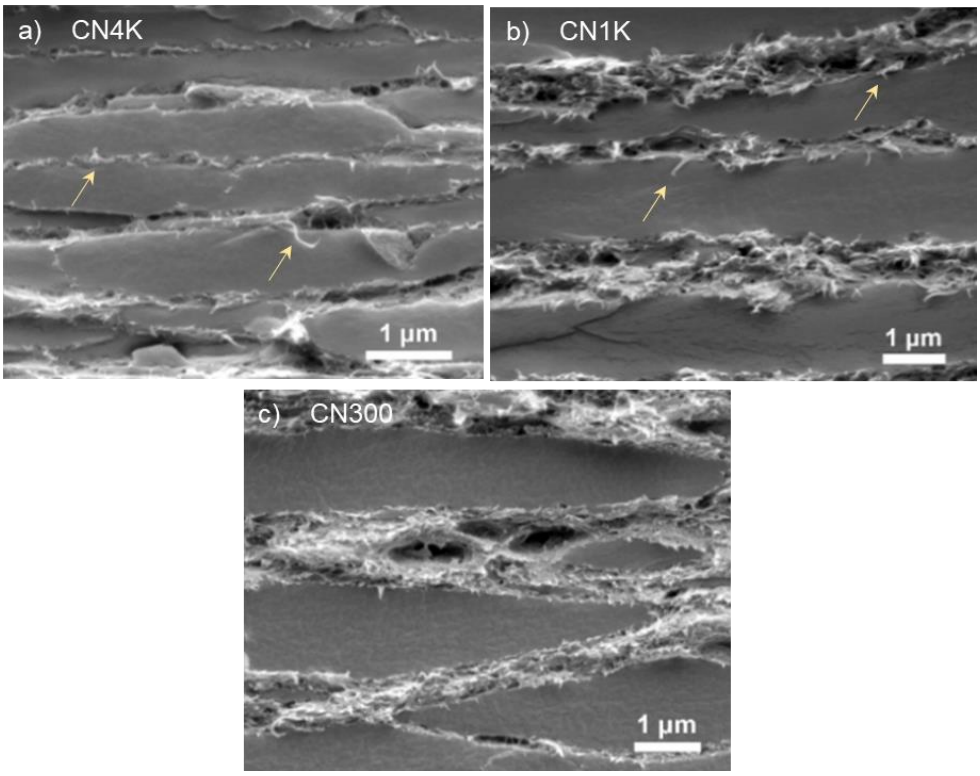

Figure 4.8. High magnification FE-SEM images of the fracture surface of CN4K (a), CN1K (b), and CN300 (c) nanocomposites. The samples were obtained after tensile test.

4.3.4. Thermomechanical stability of the nanocomposites

The thermomechanical stability results presented in Figure 4.9 and Table 4.3 show that the storage modulus (E') of the neat polymer decreased by more than one order of magnitude (4.04 to 0.08 GPa) from −50 to 150 °C owing to the glass transition. Notably, the storage modulus of the polymer was relatively stable in the temperature range from ~20 to 150 °C, although it was extremely low (0.06 ± 0.01 GPa). A polymer with T_g < 0 °C shows stable mechanics above room temperature. Therefore, when the polymer was reinforced with a hierarchical CN network, not only the storage modulus greatly improved, but, most importantly, it remained highly stable over a wide temperature range. The CN4K, CN1K, CN400, and CN300 nanocomposites retained high elastic moduli of 1.12, 1.60, 1.77, and 1.80 GPa, respectively, even at 150 °C. The high E' values indicated a good dispersion of the load-bearing hierarchical CN network with extensive hydrogen bonding and a synergistic interaction between the thermally stable CNs and the CN-network-reinforced polymer platelets, which inhibited thermal relaxation motion of the polymer phase [26]. The values also indicated that a thick and dense CN network (Fig. 4.8) and high crystallinity are beneficial.

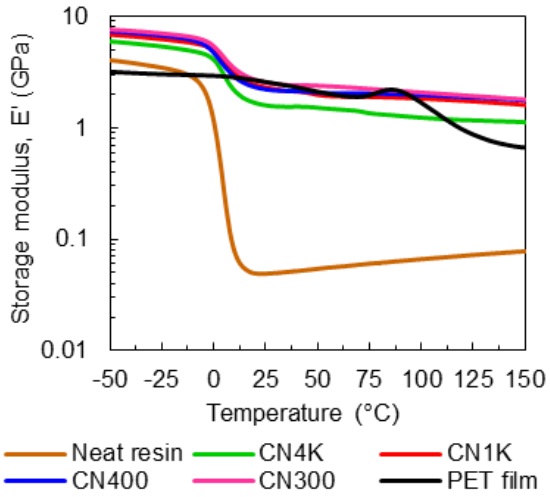

Figure 4.9. Storage modulus *E′* as a function of temperature.

Table 4.3. Storage modulus, *E′*, data for the nanocomposites and polymer films at different temperatures obtained from the dynamic mechanical analysis.

Sample	*E′* @ -50 °C [GPa]	*E′* @ 23 °C [GPa]	*E′* @ 150 °C [GPa]
Neat resin	4.04	0.05	0.08
CN4K	5.96	1.62	1.12
CN1K	6.85	2.35	1.60
CN400	7.36	2.25	1.77
CN300	7.58	2.60	1.80
PET	3.18	2.62	0.66

For comparison, a commercial thermally stable biaxially oriented PET film (Lumirror, Toray, Japan) used in the optoelectronic industry was also tested (Fig. 4.9). After being relatively stable from −50 to 85 °C, the *E′* value of the film drastically decreased to 0.66 GPa at 150 °C. The *E′* of polyimide (PI), another commercially used polymer film, has similar high mechanical stability against elevated temperature to the nanocomposites, although it suffers from having an unwanted brownish tint [26]. Therefore, the high and stable *E′* at elevated temperatures is a promising characteristic of the transparent nanocomposites for practical application in organic/inorganic optoelectronic devices.

4.3.5. Thermal-dimensional stability of the nanocomposites

The thermal dimensional properties of the transparent nanocomposites are shown in Figure 4.10 and Table 4.4. The neat polymer expanded by 2.42% in the planar direction (*x* or *y* direction) from 20 to 150 °C. However, for the CN4K, CN1K, CN400, and CN300 nanocomposites, thermal expansion was only 0.16, 0.11, 0.08, and 0.08% in the *x* or *y* direction, respectively. The CTE of the neat polymer from 20 to 150 °C in the *x* or *y* direction was very high (190.53 ppm K^{-1}). However, owing to strong hierarchical reinforcement from the low-CTE CNs to the polymer platelets, the CTE drastically decreased to 12.10, 8.28, 6.29, and 5.49 ppm K^{-1} for CN4K, CN1K, CN400, and CN300, respectively. Clearly, the highly crystalline short CNs with a thick and dense network layer produced highly thermal-dimensionally stable nanocomposites.

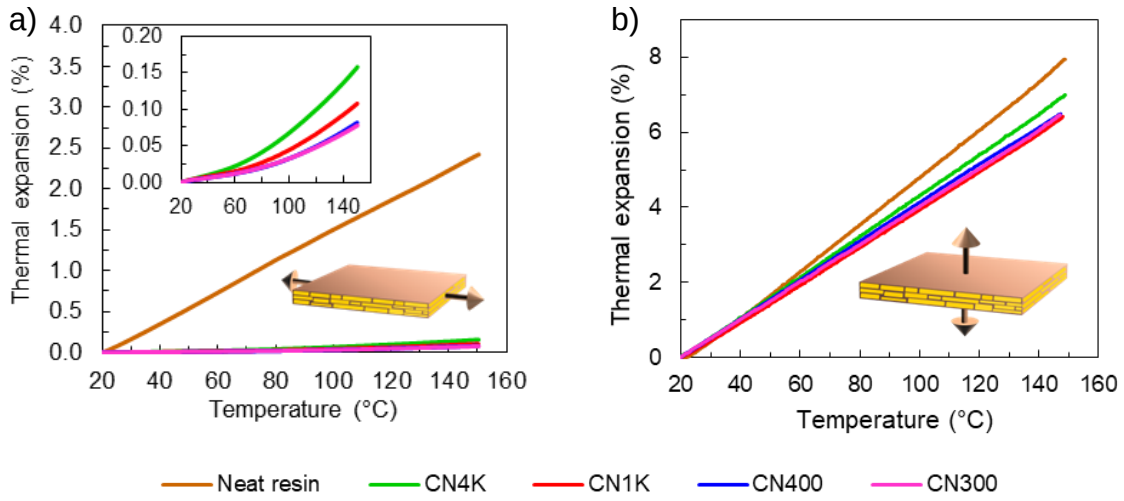

Figure 4.10. (a) Thermal expansion in the *x* or *y* direction. (b) Thermal expansion in *z* direction.

Table 4.4. CTE values in planar (*x* or *y*) and thickness (*z*) directions.

Sample	CTE (*x*- or *y*-direction) [ppm K^{-1}]			CTE (*z*-direction) [ppm K^{-1}]
	20-80 °C	20-100 °C	20-150 °C	20-150 °C
Neat resin	184.67	189.01	190.53	624.46
CN4K	6.93	8.48	12.10	542.50
CN1K	4.55	5.59	8.28	509.84
CN400	3.38	4.10	6.29	509.36
CN300	2.54	3.36	5.49	506.49

The CTE values were incredibly low at only ~10% CN content. In the previous studies, a high nanocellulose content of >60 wt% was used to obtain transparent nanocomposites with CTE values below 10 ppm K^{-1} [12,27]. To understand the underlying reason, the thermal dimensional stability of the nanocomposites in the thickness direction (*z* direction) was investigated (Fig. 4.10b and Table 4.4). It was found that thermal expansion of the neat polymer and nanocomposites is anisotropic. Thermal expansion and the CTE of the neat polymer in the *z* direction from 20 to 150 °C were 7.94% and 624.46 ppm K^{-1}, respectively. In the *z* direction, thermal expansion and the CTEs of the nanocomposites decreased to 6.46–7.00% and 506.49–542.50 ppm K^{-1}, respectively. This again proved that the nanocomposites reinforced with a thick and dense network of highly crystalline short CNs show high thermal dimensional stability. Compared with the *x* or *y* direction, thermal expansion and the CTE values of the nanocomposites in the *z* direction were extremely high. These phenomena have also been observed for a nanocomposite with a similar hierarchical structure [1]. This was probably because the CNs were randomly oriented in-plane in the nanocomposites. In addition, owing to the very low modulus of the acrylic resin (E = 0.03 GPa), the induced thermal stresses were very small [1]. Therefore, the high thermal expansion of the polymer in the *x* or *y* direction was dramatically suppressed by the hierarchical in-plane rigid network of short and highly crystalline CNs, and it was also accommodated by the huge expansion in the *z* direction. Note that the absolute value of *z*-direction expansion is insignificant owing to the thinness of the nanocomposites.

Thermal expansion of the transparent nanocomposites is much lower than those of the transparent polymeric films reported as optoelectronic substrates (Fig. 4.11 and Table 4.5) [12,26,28]. In particular, the CTE of the CN300 nanocomposite was 3.4 and 5.5 ppm K^{-1} in the temperature ranges 20–100 °C and 20–150 °C, respectively. These values are comparable with those of highly stable borosilicate glass (~4 ppm K^{-1}) [24], and semiconducting silicon crystals (~3 ppm K^{-1}) [1].

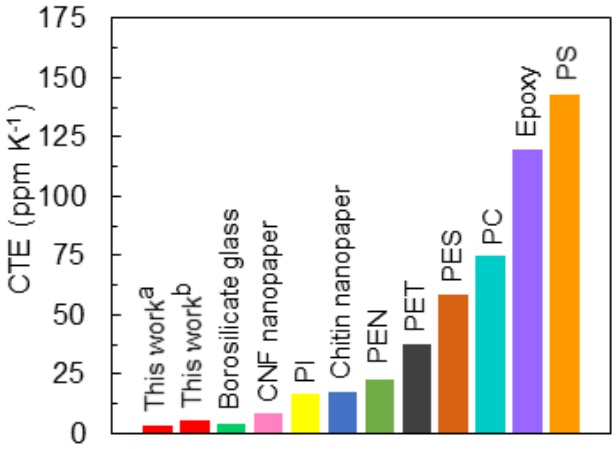

Figure 4.11. CTE of the CN300 transparent nanocomposite compared with a variety of other transparent optoelectronic substrates. [a]CN300 @ 20–100 °C; [b]CN300 @ 20–150 °C; borosilicate glass [24]; CNF nanopaper (this work); PI, polyimide [26]; chitin nanopaper [26]; PEN, polyethylene naphthalate [26]; PET, polyethylene terephthalate (this work); PES, polyether sulfone [26]; PC, polycarbonate (this work); epoxy [12]; and PS, polystyrene [28]. Also, see Table 4.5 for more details.

Table 4.5. CTE of the transparent nanocomposite (CN300) and a range of transparent polymer films.

Material	CTE [ppm K^{-1}]	Temperature range [°C]	References/ comments
This work[a]	3.4	20-100	CN300
This work[b]	5.5	20-150	CN300
Borosilicate glass	~4.0	-	24
CNF nanopaper	8.5	20-150	This work
PI (Polyimide)	17.1	40-170	26
Chitin nanopaper	17.5	40-170	26
PEN (Polyethylene naphthalate)	23	40-110	26
PET (Polyethylene terephthalate)	38	20-150	This work
PES (Polyether sulfone)	58.6	40-170	26
PC (Polycarbonate)	74.7	25-100	This work
Epoxy	120	50-150	12
PS (Polystyrene)	143	30-100	28

"-" indicates no data available.

4.3.6. Thermo-optical stability of the nanocomposites

In addition to the thermo mechanical and thermal dimensional stability, the thermo-optical stability of a transparent substrate is also an important requirement. The substrate must maintain high optical clarity after the high-temperature (~100–150 °C) processing steps, such as the fabrication of the transparent conductive electrode (TCE) and deposition of functional materials [4]. Amazingly, the nanocomposites still transmitted ~83% (at 600 nm) of specular light (i.e., regular or linear transmittance) even after 120 min heating at 180 °C, which was ~86% before heating (Fig. 4.12). The diffusive transmittance (i.e., total transmittance) was ~90%, and it decreased to ~88% after 120 min heating (Fig. 4.12). This high-level thermo-optical stability was because of the high thermo-optical stability of the acrylic resin. The slight decrease in the transparencies of the nanocomposites with increasing time was probably because of initiation of thermal decomposition of the cellulose at about 180 °C [18]. However, TGA revealed that the nanocomposites were fairly stable against thermal decomposition (Fig. 4.13). The CN4K and CN1K nanocomposites lost 1% of their weight up to ~290 °C, and the CN400 and CN300 nanocomposites lost 1% of their weight up to ~280 °C.

A commercial PET film was also heated at 180 °C to compare the thermo-optical stability. The film started to turn hazy after 30 min heating. After only 60 min heating, the specular transmittance (linear transmittance) decreased from 86% to 55% and the diffusive transmittance (total transmittance) decreased from 88% to 83% (Fig. 4.12). Similar degradation in the optical quality of the PET film at 150 °C was reported, which was because of the increase in the surface roughness induced by migration of cyclic oligomers to the film surface [4].

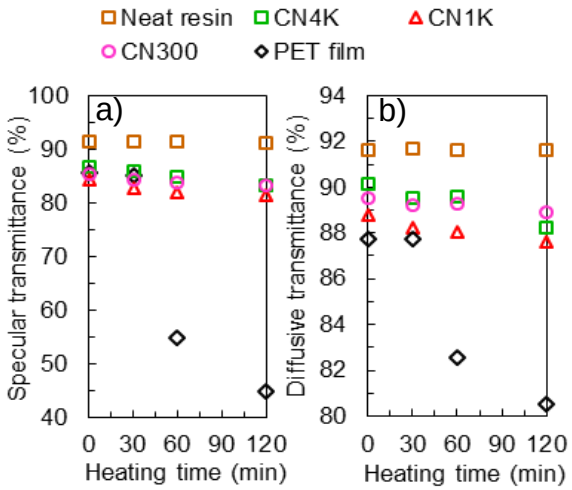

Figure 4.12. Optical transmittance at 600 nm wavelength as a function of the heating time at 180 °C.

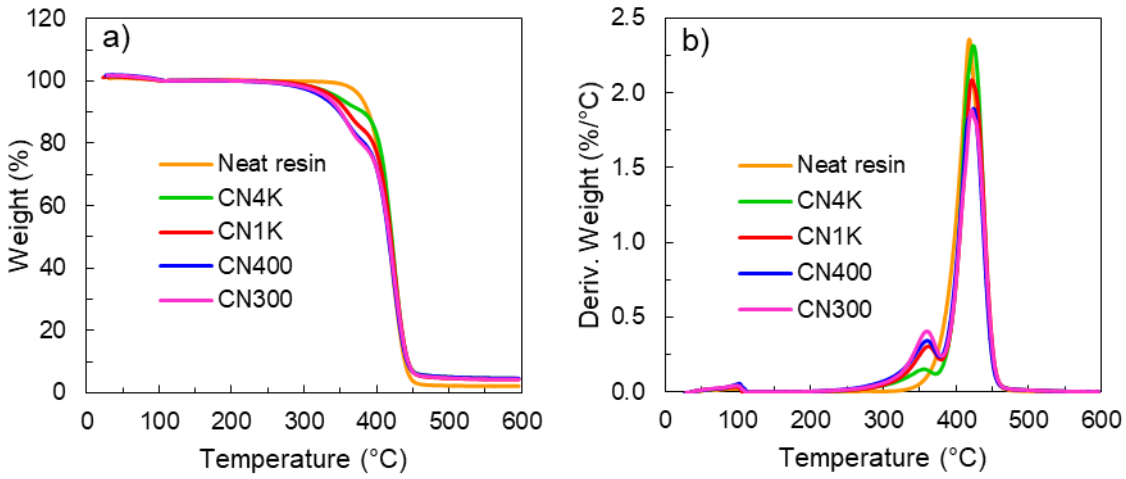

Figure 4.13. Thermogravimetric (a) and derivative thermogravimetric (b) curves of the nanocomposites.

4.3.7. Thermal stability of the µLA on the surface of the nanocomposite

Amelioration of substrates using nano/microscale surface structures for better light management in optoelectronic devices is a rapidly developing field. Nano/microscale surface features improve the efficiency of solar cells, OLEDs, and optical sensors by supporting strong photonic resonance, reducing plasmonic loss, and enhancing photon absorption, scattering, and outcoupling [3,29–32]. As presented in Chapter 2, the surface of the CN/resin nanocomposites could be patterned in situ during hot compressing by simply sandwiching the CN/resin mat between a glass slide and an oppositely patterned template (one-sided) or between two templates (two-sided), as shown in Figure 2.26 (Chapter 2). Formation of the pattern was facilitated because the strong CN-network held the resin in the liquid state in the mat. Hence, nano/microscale polymeric structures could be easily and directly obtained with great precision on the surface of the CN-reinforced transparent nanocomposites.

Based on the excellent thermal stability of the nanocomposites, in situ fabricated patterns on the nanocomposites were expected to be highly thermally stable. As a demonstration, a µLA that showed rainbow colors owing to diffraction of light was fabricated (Fig. 4.14a). A custom experiment was designed to demonstrate the thermal stability of the µLA in real time (Fig. 4.2). The µLAs on the highly stable CN300 nanocomposite and a neat polymer film were separately clipped on glass slides and a green laser beam was pointed at them. As shown in Figure 4.14b(i) and (ii), the laser beam was diffracted by the periodic microlenses on the polymer film and pro-

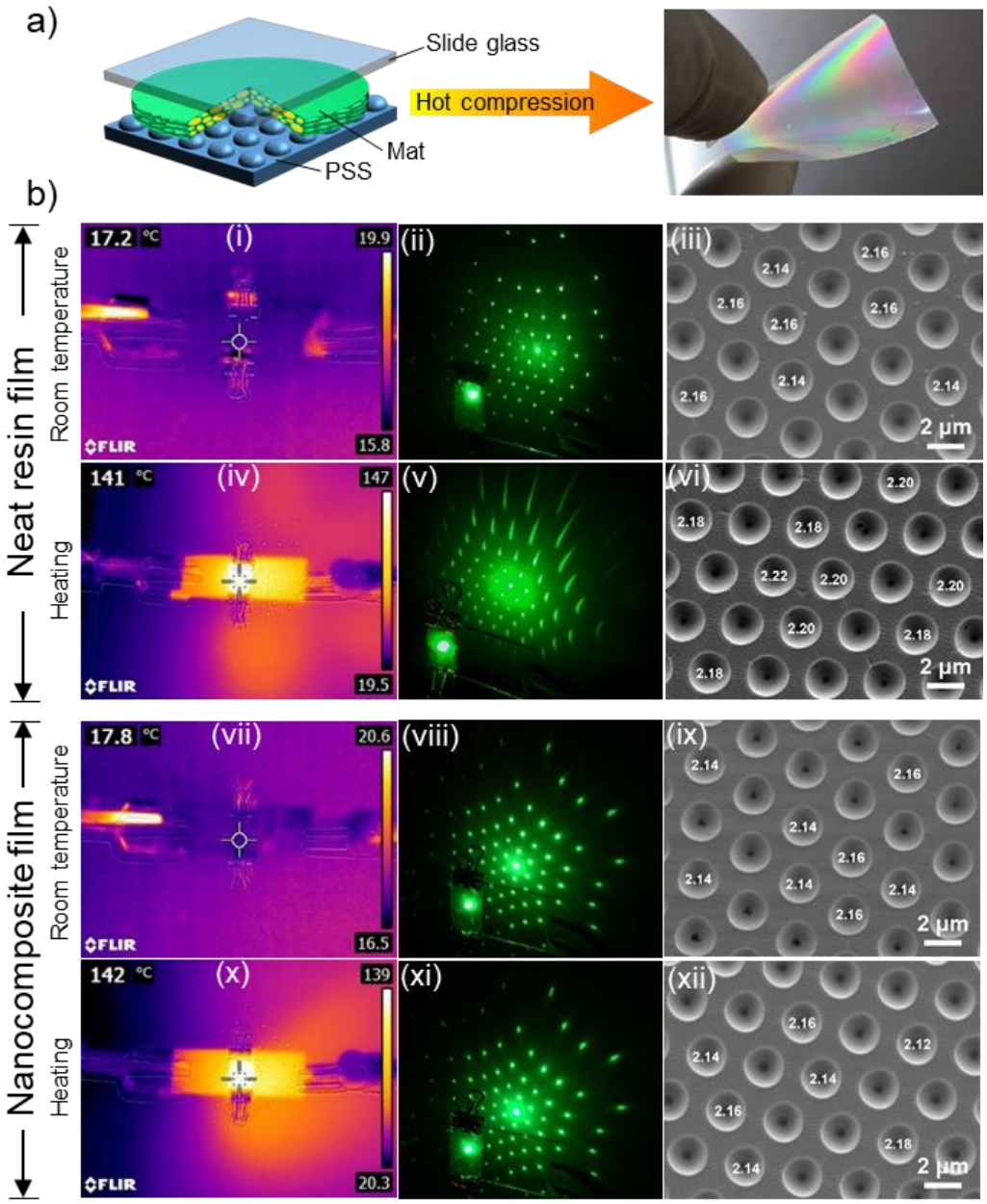

Figure 4.14. Thermal stability of the micropattern on the surface of the transparent nanocomposite. (a) Fabrication of a μLA on the surface of the CN300 nanocomposite. (b) Thermal stability of the μLA on the nanocomposite compared with that on the neat resin film. (i), (iv), (vii), and (x) Thermal images, (ii), (v), (viii), and (xi) laser beam diffraction patterns (μLAs are highlighted by the yellow dashed line), and (iii), (vi), (ix), and (xii) FE-SEM images of the μLA before and after heating.

duced a well-defined pattern on the back screen at room temperature (~17 °C). When the μLA on the polymer film was heated to ~140 °C for only 2 min with a heat gun, the film expanded and produced a deformed diffraction pattern, as shown in Figure 4.14b(iv) and (v). FE-SEM images before and after heating (Fig. 4.14b(iii) and (vi)) revealed that the diameter of the microlenses increased from ~2.15 to ~2.19 μm owing to very large planar expansion of the neat polymer film. The increase in diameter was about 1.86%, which was less than the aforementioned planar expansion of the neat polymer film from 20 to 150 °C (2.42%). This was probably because of shrinkage of the polymer film between the thermal-stability experiment and FE-SEM imaging. In contrast, the μLA on the transparent CN300 nanocomposite was highly stable and there were no significant differences in the laser diffraction patterns and microlens diameters before and after heating (Figure 4.14b(vii–xii)). The strong hierarchical CN network restricted planar thermal expansion of the polymer, so the microlenses on the nanocomposite film were thermally stable. This is advantageous for optoelectronic device processing because any deformation/damage in the nano/microscale features might affect the performance of the device [3]. The high thermal stability of the nano/micropatterned films also could be desirable in other application areas, including 3D imaging and microscopy, optical filters and stealth surfaces, data/energy storage, fuel cells, and molecule filtration [33–39].

4.4 Summary

The effect of nanocellulose length and crystallinity on the microstructure, mechanical properties, and thermal stability of the nanocomposites prepared via Pickering emulsification process were studied. A tunable mechanical properties with high flexibility (high elongation-at-break) together with a tunable thermal properties were obtained even at a similar nanocelluloses content. This was due to the difference in the hierarchical microstructure resulted from different network structure of the nanocelluloses with different length and crystallinity around the resin droplets/platelets. The short nanocelluloses with high crystallinity produced stiffer and highly thermally stable nanocomposites; a CTE as low as that of silicon crystals was obtained only at a 10 wt% CN-content. This ultrahigh thermal dimensional stability was attributed due to the combination of a unique hierarchical structure of the nanocomposites and extremely low CTE of the highly crystalline short nanocelluloses. The nanocomposites were highly thermomechanically stable even up to 150 °C, compared to the commercial thermally-stable PET film. Interestingly, stronger nanocomposites were obtained

using a combination of long and short nanocelluloses. Furthermore, the optical transparency of the nanocomposites was high at ~90%, and highly stable even at 180 °C for 2 h. In contrast, the commercial PET film showed sharp decline in transparency while heated. The μLA fabricated on the nanocomposite by direct molding was highly thermal-dimensionally stable even at a high temperature. In addition to these promising characteristics, the nanocomposites also showed no birefringence because of the random in-plane orientation of the nanocelluloses (Fig. 4.15), which is advantageous for display applications.

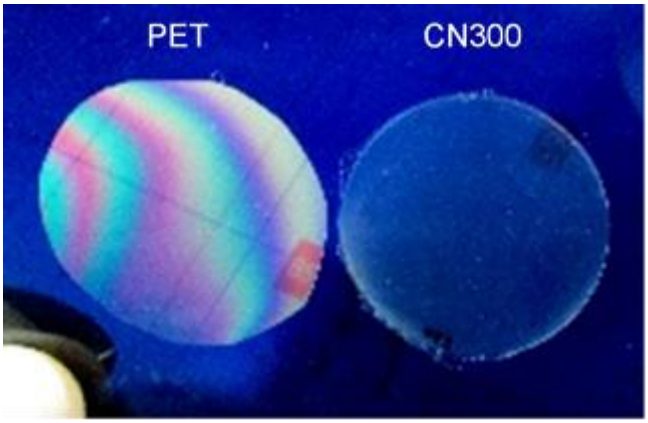

Figure 4.15. Birefringence test by sandwiching a PET film and a nanocomposite film in between cross-polarizers. The nanocomposite on the right side shows no birefringence.

4.5 References

1. Nogi M., and Yano H. Transparent nanocomposites based on cellulose produced by bacteria offer potential innovation in the electronics device industry. Advanced Materials, 2008, **20**, 1849–1852.
2. Cheng I.–C., and Wagner S. Overview of flexible electronics technology. In Flexible Electronics: Materials and Applications; Eds. W. S. Wong, and A. Salleo, Springer, New York, 2009.
3. Hippola C., Kaudal R., Manna E., Xiao T., Peer A., Biswas R., Slafer W. D., Trovato T., Shinar J., and Shinar R. Enhanced light extraction from OLEDs fabricated on patterned plastic substrates. Advanced Optical Materials, 2018, 6, 1701244.
4. Nogi M., Kim C., Sugahara T., Inui T., Takahashi T., and Suganuma K. High thermal stability of optical transparency in cellulose nanofiber paper. Applied Physics Letters, 2013, **102**, 181911.

5. Lee W. S., and Yu J. Comparative study of thermally conductive fillers in underfill for the electronic components. Diamond and Related Materials, 2005, **14**, 1647–1653.
6. Li T.–L., and Hsu S. L.–C. Enhanced thermal conductivity of polyimide films via a hybrid of micro- and nano-sized boron nitride. Journal of Physical Chemistry B, 2010, **114**, 6825–6829.
7. Jeon H., Yoon C., Song Y.–G., Han J., Kwon S., Kim S., Chang I., and Lee K. Reducing the coefficient of thermal expansion of polyimide films in microelectronics processing using ZnS particles at low concentrations. ACS Applied Nano Materials, 2018, **1**, 1076–1082.
8. Sullivan L. M., and Lukehart C. M. Zirconium tungstate (ZrW_2O_8)/polyimide nanocomposites exhibiting reduced coefficient of thermal expansion. Chemistry of Materials, 2005, **17**, 2136–2141.
9. Zhang X., Zhang H., Lin J., Li L., and Wu Q. Thermal conductivity and thermal stability enhancement of ethylene propylene diene methylene with carbon nanotube. Journal of Reinforced Plastics and Composites, 2014, **33**, 767–774.
10. Carvalho H. W. P., Santilli C. V., Briois V., and Pulcinelli S. H. Polymer–clay nanocomposites thermal stability: Experimental evidence of the radical trapping effect. RSC Advances, 2013, **3**, 22830–22833.
11. Klemm D., Cranston E. D., Fischer D., Gama M., Kedzior S. A., Kralisch D., Kramer F., Kondo T., Lindström T., Nietzsche S., Petzold-Welcke K., and Rauchfuß F. Nanocellulose as a natural source for groundbreaking applications in materials science: Today's state. Materials Today, 2018, **21**, 720-748.
12. Yano H., Sugiyama J., Nakagaito A. N., Nogi M., Matsuura T., Hikita M., and Handa K. Optically transparent composites reinforced with networks of bacterial nanofibers. Advanced Materials, 2005, **17**, 153–155.
13. Kontturi E., Laaksonen P., Linder M. B., Nonappa, Gröschel A. H., Rojas O. J., and Ikkala O. Advanced materials through assembly of nanocelluloses. Advanced Materials, 2018, **30**, 1703779.
14. Wang H. H. C. Cellulose and pulp. In Forests and Forest Plants, Vol. 2; Eds. J. N. Owens, and H. G. Lund, Eolss Publishers/UNESCO: Oxford, 2009.
15. Dufresne A. Nanocellulose: A new ageless bionanomaterial. Materials Today, 2013, **16**, 220–227.
16. Nishino T., Matsuda I., and Hirao K. All-cellulose composite. Macromolecules, 2004, **37**, 7683–7687.

17. Kalashnikova I., Bizot H., Bertoncini P., Cathala B., and Capron I. Cellulosic nanorods of various aspect ratios for oil in water Pickering emulsions. Soft Matter, 2013, **9**, 952–959.
18. Agustin M. B., Nakatsubo F., and Yano H. Improving the thermal stability of wood-based cellulose by esterification. Carbohydrate Polymers, 2018, **192**, 28–36.
19. de Oliveira F. B., Bras J., Pimenta M. T. B., Curvelo A. A. d. S., and Belgacem M. N. Production of cellulose nanocrystals from sugarcane bagasse fibers and pith. Industrial Crops and Products, 2016, **93**, 48–57.
20. Svagan A. J., Busko D., Avlasevich Y., Glasser G., Baluschev S., and Landfester K. Photon energy upconverting nanopaper: A bioinspired oxygen protection strategy. ACS Nano, 2014, **8**, 8198–8207.
21. Li Y., Yu S., Chen P., Rojas, R., Hajian A., and Berglund L. Cellulose nanofibers enable paraffin encapsulation and the formation of stable thermal regulation nanocomposites. Nano Energy, 2017, **34**, 541–548.
22. Xu X., Liu F., Jiang L., Zhu J. Y., Haagenson D., and Wiesenborn D. P. Cellulose nanocrystals vs. cellulose nanofibrils: A comparative study on their microstructures and effects as polymer reinforcing agents. ACS Applied Materials and Interfaces, 2013, **5**, 2999–3009.
23. Steinmann W., and Saelhoff A.-K. Essential properties of fibres for composite applications. In Fibrous and Textile Materials for Composite Applications. Eds. S. Rana, and R. Fangueiro, Springer, Singapore, 2016; pp 39–73.
24. Ashby M. F. Materials selection in mechanical design, 3rd ed. Butterworth-Heinemann: Oxford, UK, 2005; pp 522−531.
25. Zhu M., Song J., Li T., Gong A., Wang Y., Dai J., Yao Y., Luo W., Henderson D., and Hu L. Highly anisotropic, highly transparent wood composites. Advanced Materials 2016, **28**, 5181–5187.
26. Jin J., Lee D., Im H.-G., Han Y. C., Jeong E. G., Rolandi M., Choi K. C., and Bae B.-S. Chitin nanofiber transparent paper for flexible green electronics. Advanced Materials, 2016, **28**, 5169–5175.
27. Song X., Yang S., Liu X., Wu M., Li Y., and Wang S. Transparent and water-resistant composites prepared from acrylic resins ABPE-10 and acetylated nanofibrillated cellulose as flexible organic light-emitting device substrate. Nanomaterials, 2018, **8**, 648.
28. Fujisawa S., Togawa E., and Kuroda K. Facile route to transparent, strong, and thermally stable nanocellulose/polymer nanocomposites from an aqueous Pickering emulsion. Biomacromolecules, 2017, **18**, 266–271.

29. Brongersma M. L., Cui Y., and Fan S. Light management for photovoltaics using high-index nanostructures. Nature Materials, 2014, **13**, 451–460.
30. Wang Z., Peng L., Lin Z., Ni J., Yi P., Lai X., He X., and Lei Z. Flexible semiconductor technologies with nanoholes-provided high areal coverages and their application in plasmonic-enhanced thin film photovoltaics. Scientific Reports, 2017, **7**, 13155.
31. Xiang H.-Y., Li Y.-Q., Zhou L., Xie H.-J., Li C., Ou Q.-D., Chen L.-S., Lee C.-S., Lee S.-T., and Tang J.-X. Outcoupling-enhanced flexible organic light-emitting diodes on ameliorated plastic substrate with built-in indium–tin-oxide-free transparent electrode. ACS Nano, 2015, **9**, 7553–7562.
32. Abramowitz M., and Davidson M. W. Microlens Arrays. https://www.olympus-lifescience.com/zh/microscope-resource/primer/digitalimaging/concepts/microlensarray/ (accessed on Jun 30, 2018).
33. Song Y. M., Xie Y., Malyarchuk V., Xiao J., Jung I., Choi K.-J., Liu Z., Park H., Lu C., Kim R.-H., Li R., Crozier K. B., Huang Y., and Rogers J. A. Digital cameras with designs inspired by the arthropod eye. Nature, 2013, **497**, 95–99.
34. Wu D., Wang J.-N., Niu L.-G., Zhang X. L., Wu S. Z., Chen Q.-D., Lee L. P., and Sun H. B. Bioinspired fabrication of high-quality 3D artificial compound eyes by voxel-modulation femtosecond laser writing for distortion-free wide-field-of-view imaging. Advanced Optical Materials, 2014, **2**, 751–758.
35. Diao Z., Kraus M., Brunner R., Dirks J.-H., and Spatz J. P. Nanostructured stealth surfaces for visible and near-infrared light. Nano Lett. 2016, **16**, 6610–6616.
36. Zhou M., Xu Y., and Lei Y. Heterogeneous nanostructure array for electrochemical energy conversion and storage. Nano Today, 2018, **20**, 33–57.
37. Zhou Z., Dominey R. N., Rolland J. P., Maynor B. W., Pandya A. A., and DeSimone J. M. Molded, high surface area polymer electrolyte membranes from cured liquid precursors. Journal of the American Chemical Society, 2006, **128**, 12963–12972.
38. Yasui T., Rahong S., Motoyama K., Yanagida T., Wu Q., Kaji N., Kanai M., Doi K., Nagashima K., Tokeshi M., Taniguchi M., Kawano S., Kawai T., and Baba Y. DNA manipulation and separation in sublithographic-scale nanowire array. ACS Nano, 2013, **7**, 3029–3035.
39. Kim M.-H., Sawada Y., Taya M., and Kino-oka M. Influence of surface topography on the human epithelial cell response to micropatterned substrates with convex and concave architectures. Journal of Biological Engineering, 2014, **8**, 13.

Chapter 5
Application of the Nanocomposites as the Substrate for Thermally Resilient Transparent Conductive Electrodes

5.1 Introduction

Flexible and transparent plastic substrates are ubiquitous in the preparation of large-area electrodes onto which functional materials are deposited to make optoelectronic devices. An ultrathin layer of conductive coating is generally applied to the plastics to produce transparent electrodes, with indium tin oxide (ITO) currently serving as the predominant coating material. However, ITO is not preferred for flexible electronic applications because of its brittle nature and rising cost [1,2]. Therefore, nanomaterials such as carbon nanotubes (CNTs) [1,3−5], graphene [1,6−8], silver nanowires (AgNWs) [1,2,9−16], copper nanowires [16], and gold nanowires [16] have been widely studied; these materials are able to produce a flexible conductive nano-network on the large-area substrate with a relatively low density. However, most plastics expand and shrink in response to heating and cooling. The thermal expansion of plastics, especially of flexible plastics, often exceeds 200 ppm K^{-1} [17]. This large dimensional change can generate a large mechanical stress that can produce cracks in the ultrathin nano-network of the conducting nanomaterials, resulting in reduction of the conductivity of the electrodes. Devices that experience repeated heating and cooling are particularly susceptible. For example, a device mounted on an aircraft or spacecraft frequently experiences high temperature variation. The temperature on the outer surface of a flying aircraft can vary from approximately −50 °C to >100 °C depending on the Mach number and altitude [18]. In addition, a high temperature (>100 °C) is often required to deposit or anneal functional materials on the electrodes. Therefore, a transparent and flexible electrode with high thermal dimensional stability is highly desirable.

In Chapter 4, it was demonstrated that the thermal dimensional stability of a plastic can be improved by approximately 60 times (from CTE ~190 ppm K^{-1} to CTE ~3.4 ppm K^{-1}) by incorporating nanocelluloses at a content as low as 10 wt%. This incredible result at a low nanocellulose-content was obtained because of the unique hierarchical structure of the

nanocomposites offered by the Pickering emulsification method and the use of highly thermally stable crystalline short nanocelluloses – cellulose nanocrystals or nanorods (CNs). The CNs exhibit incredible thermal stability with a coefficient of thermal expansion (CTE) of ~0.1 ppm K^{-1} and an elastic modulus (E) of ~140 GPa that remains stable from approximately −200 °C to >100 °C [19−21]. Unlike other reinforcing nanomaterials, such as clays, silica, alumina, boron nitride, and zirconium tungstate [22−24], which must be incorporated at a high percentage (often ~50% by weight), the low CN-content also resulted in a high optical transmittance (~90%) and great mechanical flexibility (fracture strain of up to ~15%). The reinforced plastics also retained a high optical clarity even at 180 °C and exhibited no birefringence compared with a thermally stable polyethylene terephthalate (PET) film.

Geared from the excellent result obtained in thermal-dimensional stability of the nanocomposites prepared via Pickering emulsion method, it was hypothesized that a highly thermally resilient transparent conductive electrode of AgNWs could be obtained using those transparent nanocomposites as the substrate.

Therefore, in this part of the study, transparent conductive AgNW electrodes were prepared using nanocomposites as the substrate. The electrodes were repeatedly subjected to extremely high (150 °C) and low (−196 °C) temperatures to investigate the thermo-electrical performances. As a proof-of-concept, a transparency-modulating smart-device of liquid crystals was also fabricated on the nanocomposite electrodes, and then repeatedly subjected to high and low temperatures to reveal the device performances.

5.2 Materials and method

5.2.1. Materials

Wood powder of Japanese Cypress sieved through 60 mesh was used as the raw material for the CNs preparation. The acrylic monomer 2,2-bis[4-(acryloxypolyethoxy)phenyl]propane (Shin-Nakamura Chemical, Japan) was prepared by adding (0.25 wt%) a UV-polymerization initiator 2-hydroxy-2-methylpropiophenone (Wako). AgNWs suspended in water (0.5 wt%) were provided by Seiko PMC Corporation, Japan. Liquid crystal E-7 was purchased from LCC Corporation, Japan. NOA65 UV-curing adhesive was purchased from THORLABS, Japan. Ethanol (Wako), toluene (Wako), acetone (Wako), acetic acid (Wako), $NaClO_2$ (Sigma-Aldrich), KOH (Wako), and HCl (Wako) were used as received.

5.2.2. Preparation of CNs

The CNs were prepared from wood powder following the process described in Chapter 4. Briefly, the wood powder was first extracted with an azeotrope of ethanol:toluene:acetone (1:2:1) in a Soxhlet apparatus for 10 h to remove extractives, and then treated with acidified-$NaClO_2$ and KOH to remove the lignin and most of the hemicelluloses. Subsequently, the purified powder was passed twice through a grinder (MKCA6-2, Masuko Sangyo, Japan) to obtain CNFs, which were then hydrolyzed using 2 N HCl at 70 ℃ for 4 h to obtain CNs.

5.2.3. Preparation of transparent nanocomposites

The fabrication process of the hierarchical nanocomposite substrates was adopted from Chapter 4. Transparent nanocomposites with 10 wt% (TN10) and 20 wt% (TN20) CN-content were prepared. Briefly, a mixture of CNs (0.4 g for TN10 and 0.8 g for TN20), monomer (3.6 g for TN10 and 3.2 g for TN20), and deionized water (196 g) was vigorously blended to form a Pickering emulsion, which was vacuum-filtered, oven-dried (40 °C), hot-pressed (150 °C, 1.5−1.8 MPa, 5 min), and finally, polymerized using a UV light (F300S/LC6, Fusion UV Systems, USA) to obtain transparent nanocomposites of ~100 μm thickness.

5.2.4. Fabrication of AgNW transparent electrodes

The nanocomposites were cleaned with ethanol and ion-etched (Eiko IB-3, Japan) for 5 min to achieve better dispersion of the AgNW–water suspension. The AgNW suspension (0.1 wt%) was poured dropwise on the substrates and spin-coated (Mikasa 1H-D7, Japan) for 20 s at 2000 rpm. The coating process was repeated 3 times at 5-min intervals. Finally, the electrodes were kept at 40 ℃ for 1 h and then pressed at 20 MPa for 1 min at room temperature (~24 ℃) [9,10].

5.2.5. Fabrication of transparency-modulating smart device

Two nanocomposite electrodes (30 × 20 mm^2) were attached to separate glass slides with the help of a thermal release tape (release temperature = 90 ℃; REVALPHA, Nitto, Japan). A homogeneous mixture of E-7 and NOA65 (65:35) was poured on one electrode and subsequently covered by the other electrode. The NOA65 was then cured using the Fusion UV Systems. Finally, the device was released from the glass slides by heating at 90 ℃ for 5 min. Note that the thermal release tape was not used for the AE because of its low thermal stability.

Instead, the intrinsic mild adhesion of the acrylic plastic to the glass was utilized. The resulting transparency-modulating devices had a PDLC layer thickness of ~20 µm.

5.2.6. Characterizations

The FE-SEM and TEM imaging, light transmittance measurement, tensile mechanical testing, XRD analysis, thermomechanical analysis, and thermal expansion analysis were done according to the procedure described in Chapter 2, Chapter 3, and Chapter 4.

The optical haze was determined according to JIS K7136 standard following the procedure shown in Figure 5.1.

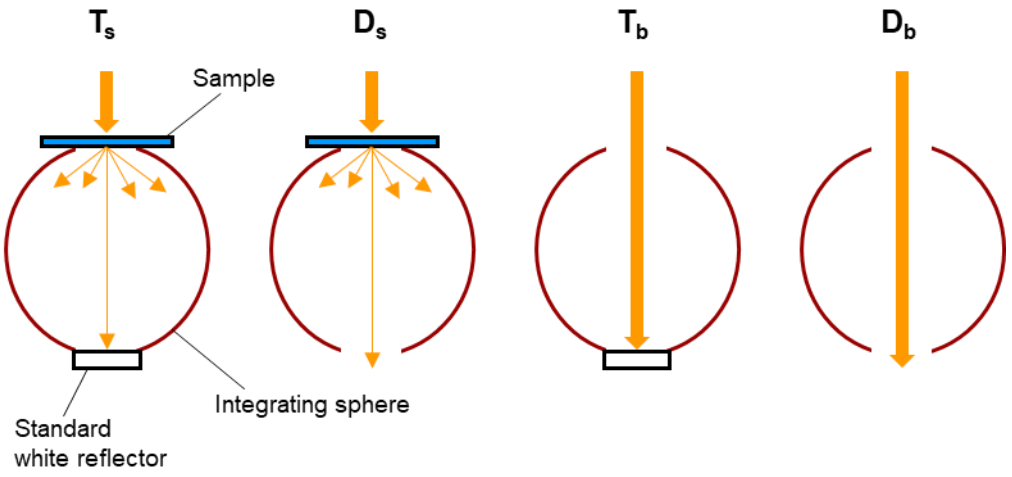

Figure 5.1. Configurations of the integrating sphere with and without sample or standard white reflector for optical haze determination. The haze was calculated according to the following equation:

$$\text{Haze}\ (\%) = \left(\frac{D_s}{T_s} - \frac{D_b}{T_b}\right) \times 100 \qquad \text{---------- (5.1)}$$

Where,

T_s = Total transmittance (sample)

D_s = Diffuse transmittance (sample)

T_b = Total transmittance (standard)

D_b = Diffuse transmittance (standard)

The thermo-electrical measurements were performed on square samples (20 × 20 mm^2) in air by cyclic heating at 80 °C−150 °C on a hot plate for 5 min and cooling in a liquid nitrogen bath for 5 min. The transparency-modulating PDLC devices underwent cyclic heating at 100 °C

in an oven for 2 min and cooling at −30 °C in a freezer for 2 min. The sheet resistance was measured using a custom-made device equipped with a 4-pin probe (pin spacing = 2 mm) by considering an appropriate correction factor. The sheet resistance was also determined by applying two silver contacts (1-mm wide and <1-μm thick lines) on the electrode samples [9]. The contacts were applied such that they made a perfect square, and they were assumed to exhibit infinite conductivity. In this work, the measurement limit for the sheet resistance was up to ~2×10^6 Ω sq^{-1}.

5.3 Results and discussion

5.3.1. Characterization of CNs

The CNs used for the hierarchical reinforcement of the acrylic plastic were prepared from wood cellulose nanofibers (CNFs) using a mild hydrochloric acid (HCl) treatment (Fig. 5.2). The length, width, and crystallinity of the CNs were 320 ± 119 nm, 15 ± 3 nm, and 70%, respectively.

5.3.2. From Pickering emulsion to transparent nanocomposite electrodes

As described in the previous chapters, first, a mixture of CNs and acrylic monomer in water was vigorously blended to form a Pickering emulsion (Fig. 5.3a,b). The process resulted in the production of numerous round micro-droplets (1.09 ± 0.66 μm) of the monomer individually encapsulated with a thin (~100−500 nm) network of the CNs (Fig. 5.3a,c,d). The CN-encapsulated micro-droplets were then collected on a filter membrane by removing water using vacuum filtration. After drying, a self-standing film referred to as “a CN/monomer mat” was obtained (Fig. 5.3a,e). The mat contained numerous liquid monomer droplets interconnected by surrounding CN networks, thereby producing a millimeter-scale bulk network of the CNs (Fig. 5.3a,f). Therefore, a two-tier hierarchical network of the CNs was generated in the CN/monomer mat. The mat was then hot-pressed and polymerized to obtain a highly transparent and hierarchically reinforced nanocomposite substrate with a thickness of ~100 μm (Fig. 5.3a,e,g). In the final step, the AgNWs (average diameter of 35 nm and length of 17.3 μm) were deposited on the nanocomposite substrate from a water suspension (0.1 wt%) by spin coating to fabricate a transparent conducting electrode with a sheet resistance of 12.4−15.6 Ω sq^{-1} (Fig. 5.2a,h,i).

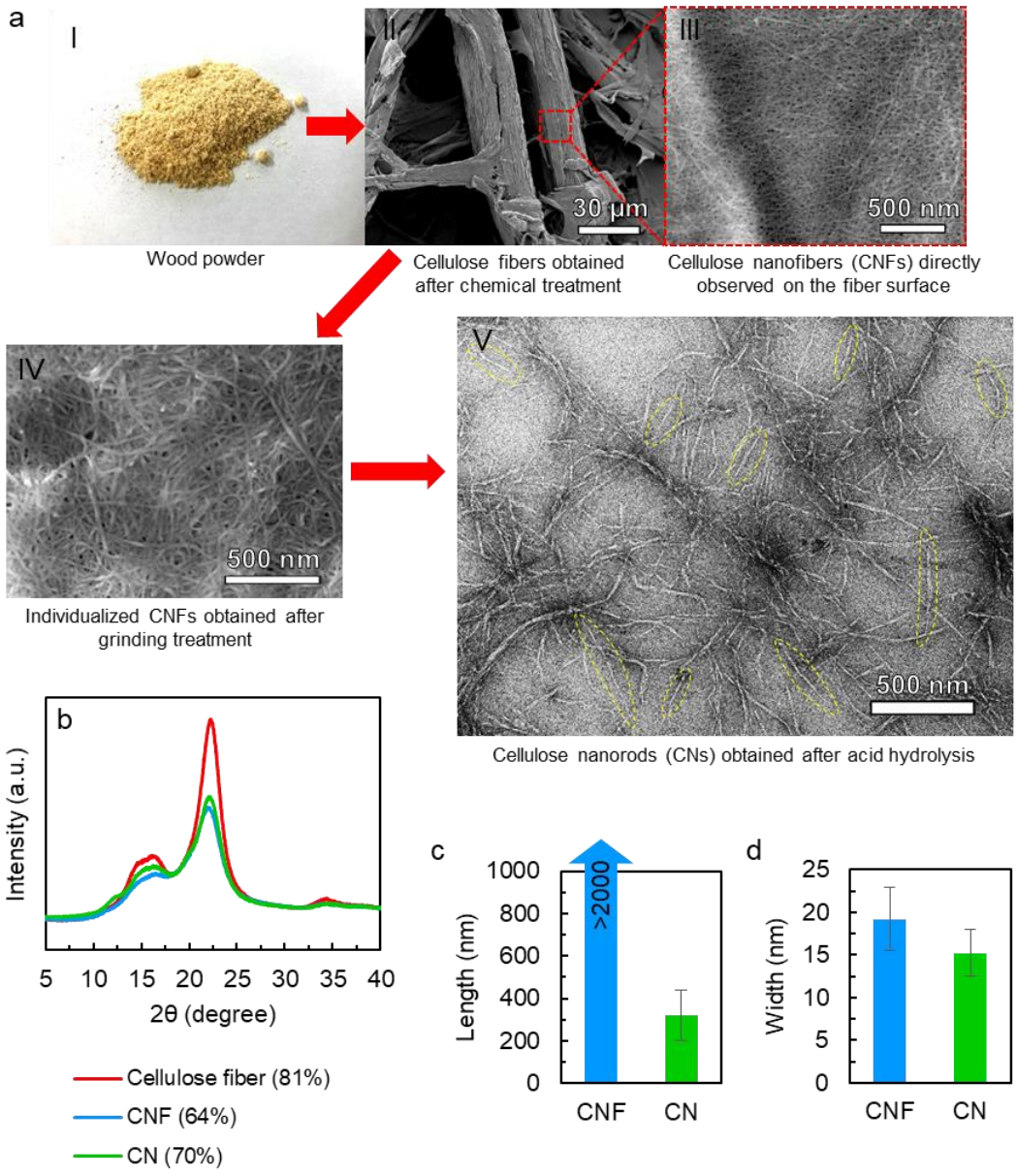

Figure 5.2. (a) Preparation of CNs from wood powder: (I) photograph of wood powder, (II,III) FE-SEM images of the cellulose fibers under different magnifications, (IV) FE-SEM image of the CNFs, and (V) TEM image of the CNs. The yellow dashed lines indicate some easily identifiable CNs. (b) XRD patterns of the cellulose fiber, CNF, and CN with the corresponding crystallinity values. (c,d) Length and width of the CNFs and CNs.

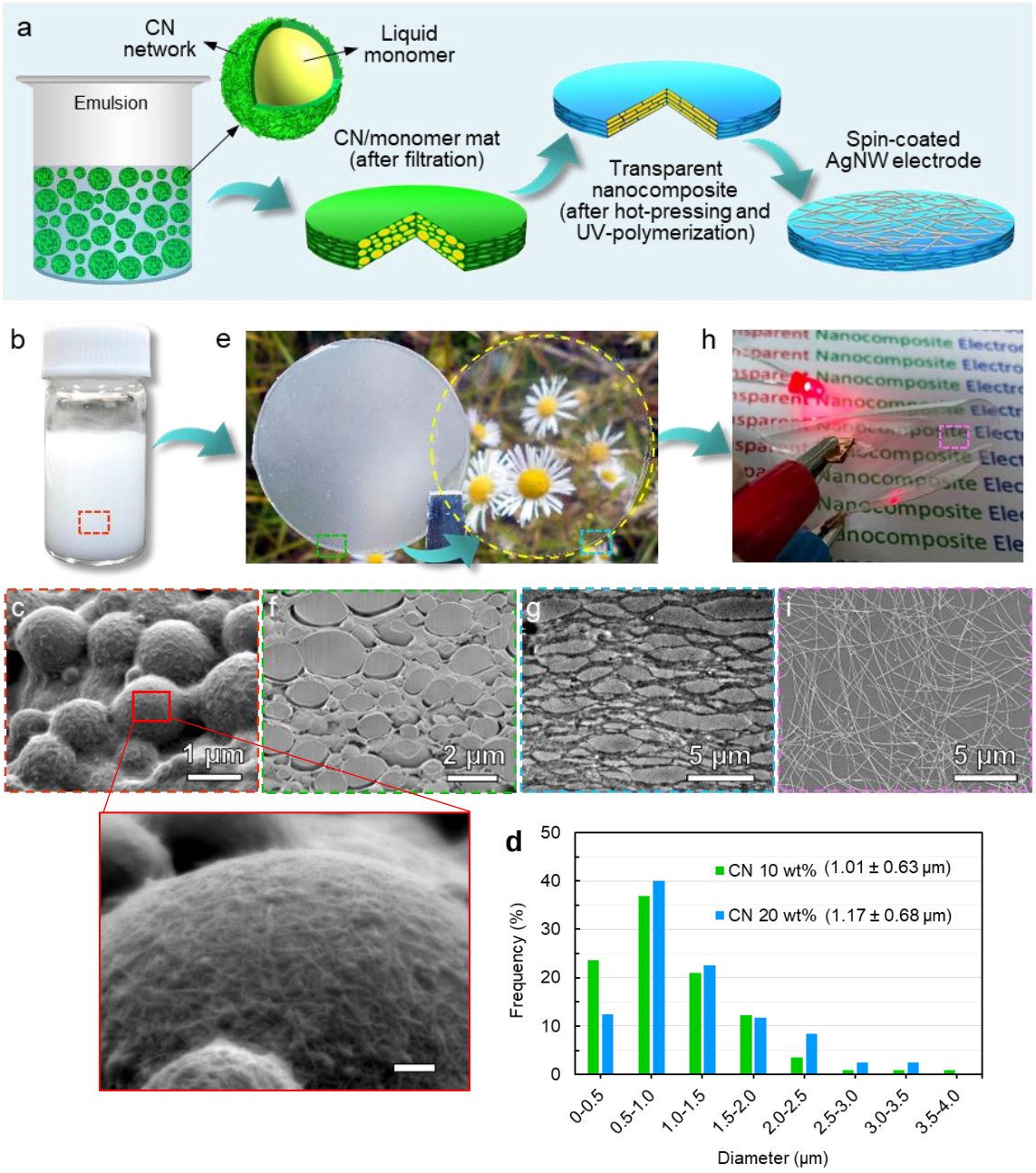

Figure 5.3. (a) Schematic illustration showing the fabrication process of the AgNW transparent electrode on a CN-reinforced hierarchical nanocomposite substrate. (b) Photograph of Pickering emulsion. (c) FE-SEM image of CN-encapsulated acrylic micro-droplets. (d) Diameter distribution of the resin micro-droplets. (e) Photographs of CN/monomer mat with 90 wt% monomer content (left) and transparent nanocomposite (right). (f) FE-SEM image of the cross-section of a mat. (g) TEM image of the cross-section of a transparent nanocomposite. (h) Photograph of transparent AgNW electrode based on hierarchical nanocomposite substrate operating in bending. (i) FE-SEM image of electrode surface showing the conducting network of the AgNWs.

5.3.3. Optical properties of the nanocomposites and electrodes

The optical transmittance spectra and haze of the nanocomposites containing 10 wt% and 20 wt% CNs (TN10 and TN20, respectively) and of their corresponding AgNW electrodes (TNE10 and TNE20, respectively) are presented in Figure 5.4. The TN10 and TN20 substrates transmitted 88% and 86% at 550-nm wavelength, respectively. These transparencies were only 3%−5% lower than that of the acrylic film (AF) because of the much smaller diameter of the CNs compared with the visible wavelength. The high transparency of the nanocomposite substrates is a good trait as a transparency of >85% is required for some flexible optoelectronic applications, e.g., bottom-emissive displays where images are observed through the substrate [25]. The transparencies of the nanocomposite electrodes were 84% and 83% for TNE10 and TNE20, respectively, compared with 87% for an acrylic film electrode (AE), at a sheet resistance of 12.4−15.6 Ω sq^{-1}. The transparencies of the nanocomposite electrodes were comparable to those of other reported transparent electrodes based on AgNW–PET (88.8% vs. 12.1 Ω sq^{-1}) [11] and ITO–glass (84% vs. 12 Ω sq^{-1}) [12] and were superior to those of electrodes based on ITO–PET (85% vs. 40 Ω sq^{-1}) [12], CNT–PET/polyethylene naphthalate (PEN)/cycloolefin polymer film Zeonor® (optimum 84% vs. 60 Ω sq^{-1}) [4], pristine graphene–glass (90% vs. 352.7 Ω sq^{-1}) [6], and modified graphene–glass (89% vs. 91.4 Ω sq^{-1}) [6] (please also see Figure 5.5).

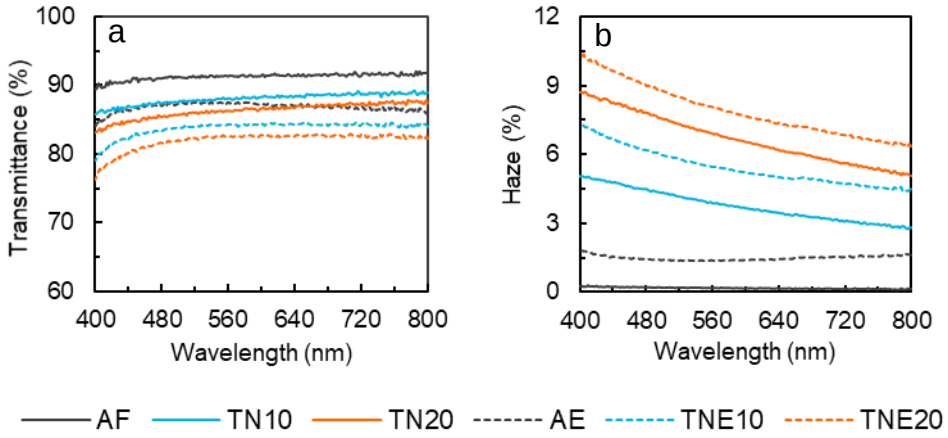

Figure 5.4. Optical properties of the transparent nanocomposites and electrodes: (a) optical transmittance and (b) haze. AF, TN10, and TN20 refer to the acrylic film and the transparent nanocomposites with 10 wt% and 20 wt% CNs reinforcement, respectively (solid lines). AE refers to the acrylic film electrode, and TNE10 and TNE20 refer to the electrodes prepared using nanocomposites having 10 wt% and 20 wt% CNs reinforcement, respectively (dashed lines).

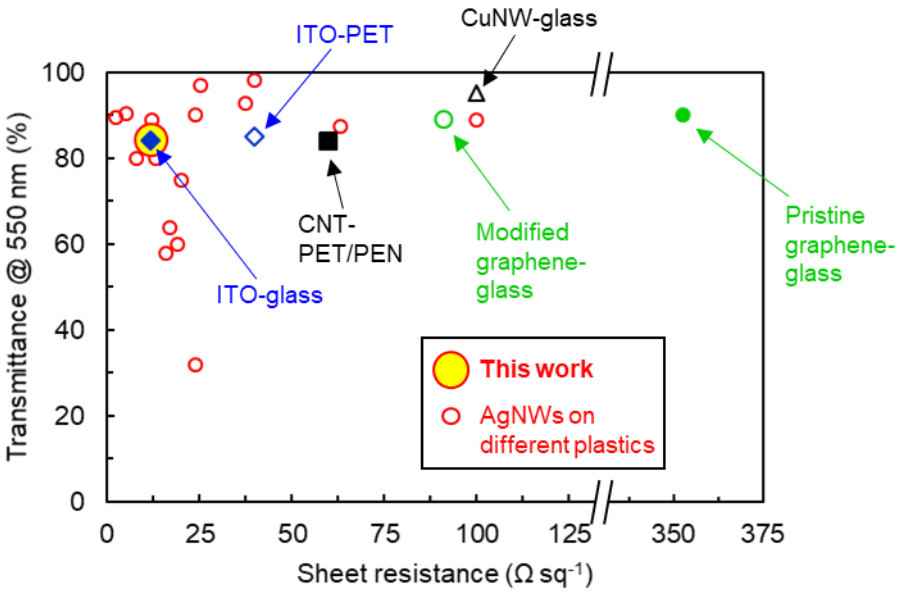

Figure 5.5. Transparency versus sheet resistance of different transparent conductive electrodes [2,4,6,9−15,26,27].

The optical haze of the TN10 substrate was 3%−5% and that of the corresponding TNE10 electrode was 4%−7% (Fig. 5.4b). The haze for the TNE10 electrode was similar to that of a previously reported PET-based electrode prepared using 40-nm-diameter AgNWs [11]. The haze of the electrodes decreased to 1%−3% when 20-nm-diameter AgNWs were used. In this study, AgNWs of 35-nm-diameter were used. The haze of TN20 was 5%−9% because of the increased light scattering from the CNs. Hence, the corresponding TNE20 electrode exhibited a slightly high haze of 6%−10%. A high haze of the substrate or electrode has been reported to increase the solar cell efficiency [28], enhance the light-outcoupling for improved light extraction from a light emitting diode [29], and reduce the glare of a display [30].

5.3.4. Mechanical properties of the nanocomposites and electrodes

Tensile mechanical tests revealed a large improvement in the strength and E of the acrylic plastic after hierarchically reinforcement with 10–20 wt% CNs (Fig. 5.6a and Table 5.1). The nanocomposites exhibited good mechanical strength of up to 23.31 ± 0.75 MPa and an E of up to 1.43 ± 0.06 GPa. No significant difference was observed in the strength and E between the nanocomposites and corresponding electrodes. A thermal-regulation film prepared by encapsulating paraffin wax in a 28 wt% CNF network also exhibited a similar mechanical strength of 30 MPa [31]. Interestingly, the strain-to-failure of the acrylic plastic increased more than two-fold from ~7% up to ~16% with the CN reinforcement. This result can be explained

by a synergistic mechanism in the hierarchical nanocomposites prepared via Pickering emulsification method, by which crack initiation in the plastic droplets by the tensile force was effectively restricted and deflected by their surrounding strong CN network and the load on the droplets was effectively dissipated to the stretchable bulk CN network [32]. The high strain-to-failure of the transparent nanocomposite substrates and electrodes is a desirable feature for flexible optoelectronic applications.

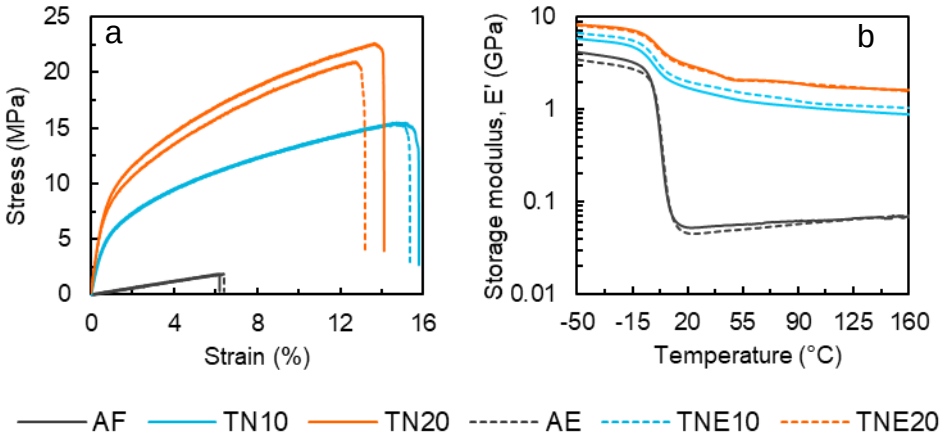

Figure 5.6. Mechanical and thermomechanical properties of transparent nanocomposites and electrodes: (a) tensile stress–strain curves and (b) thermomechanical performance.

Table 5.1. Tensile mechanical data.

Sample	Strength (MPa)		E (GPa)		Strain-to-failure (%)	
AF	1.99	± 0.34	0.03	± 0.00	6.53	± 1.25
AE	2.07	± 0.17	0.03	± 0.00	6.92	± 0.58
TN10	15.20	± 0.51	0.81	± 0.02	14.25	± 1.10
TNE10	16.02	± 0.88	0.86	± 0.02	15.54	± 0.27
TN20	23.31	± 0.75	1.43	± 0.06	14.77	± 1.39
TNE20	20.84	± 0.13	1.30	± 0.07	13.44	± 0.32

The nanocomposite substrates and electrodes also exhibited high mechanical performance at an elevated temperature with a storage modulus (E′) of up to ~1.6 GPa even at 150 °C (Fig. 5.6b and Table 5.2). As the modulus of many plastics decreases drastically (sometimes by an order of magnitude) in the temperature range of ~100°C−150 °C, the retention of a high modulus in the nanocomposites, even at 150 °C, is intriguing. This behavior can be attributed

to the hierarchical strong network of the highly thermally stable CNs that restricted the thermal relaxation motion of the plastic droplets. It is noteworthy that the high thermomechanical performance of the nanocomposite substrates is comparable to or even better than that of commercially available PEN films and thermally stabilized PET films [25,33].

Table 5.2. Dynamic thermomechanical data.

Sample	E′ (GPa)		
	23 °C	100 °C	150 °C
AF	0.05	0.06	0.07
AE	0.04	0.06	0.07
TN10	1.66	1.04	0.90
TNE10	1.95	1.17	1.06
TN20	2.94	1.81	1.64
TNE20	2.78	1.84	1.60

5.3.5. Thermal-dimensional stability of the nanocomposites and electrodes

The most important and desirable property achieved was the very high thermal dimensional stability of the nanocomposite substrates and their electrodes. Figure 5.7 shows that the thermal expansion of the AF or AE was 2.51%−2.57% in the planar direction after heating to 150 °C, which drastically decreased to 0.08%−0.11% with the hierarchical CN reinforcement. These values correspond to a CTE of 5.33−8.03 ppm K^{-1} for the nanocomposite substrates or electrodes compared with 192.32−197.29 ppm K^{-1} for the AF or AE in the temperature range of 20 °C−150 °C (Table 5.3). The CTE of the nanocomposite substrates or electrodes was even lower (3.26−4.68 ppm K^{-1}) in the temperature range of 20 °C−100 °C. Therefore, the nanocomposites can serve as excellent thermal dimensionally stable transparent flexible substrates, not only compared with heat-stabilized PET (20−25 ppm K^{-1}) or PEN (18−20 ppm K^{-1}) [25], but also compared with many other transparent plastics (Fig. 5.7c) [33,34]. Notably, the CTE was very close to that of a semiconducting silicon crystal (∼3 ppm K^{-1}) [17], which is the most commonly used functional material in electronics.

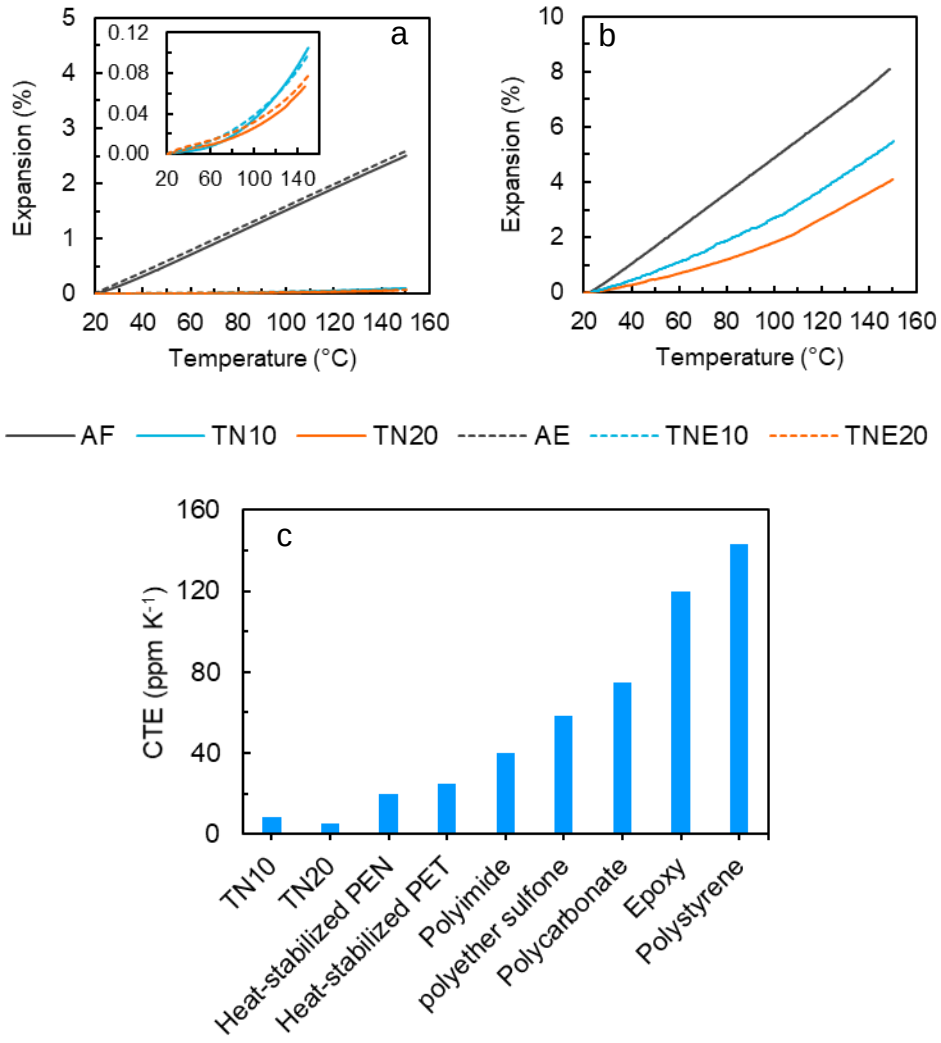

Figure 5.7. Thermal-dimensional performance in (a) planar direction and (b) thickness direction. (c) CTE of the nanocomposite substrates compared with a variety of other transparent plastic substrates [25,33−36].

Table 5.3. The CTE of the acrylic plastic, nanocomposite substrates and electrodes in the temperature range of 20−150 °C.

Sample	CTE in planar direction (ppm K^{-1})	CTE in thickness direction (ppm K^{-1})
AF	192.32	626.05
AE	197.29	–
TN10	8.03	424.85
TNE10	7.45	–
TN20	5.33	315.47
TNE20	6.01	–

The drastic reduction in the thermal expansion of the acrylic plastic only at a CN content of 10−20 wt% is unusual. Previous reports have shown that a nanocellulose content of >60 wt% is required to reduce the CTE of plastics to approximately 10 ppm K^{-1} [35,37]. To reveal the underlying reason for this behavior, the thermal expansion of the nanocomposites in the thickness direction was investigated. In contrast to the planar direction, it was observed that the expansion in the thickness direction is in fact very high at 4.10%−5.53% (Fig. 5.7b), which corresponded to a CTE of 315.47−424.85 ppm K^{-1} (Table 5.3). This behavior most likely resulted from the random in-plane orientation of the CNs in the hierarchical network within the nanocomposite, which made the nanocomposite anisotropic. Note that the CNs were initially oriented three-dimensionally in a random fashion around the round acrylic droplets. However, after filtration and hot-pressing, the CNs were oriented in-plane because the round droplets deformed into a platelet-like shape (Fig. 5.3 1a,f,g). Therefore, the thermal-stress-induced deformation of the acrylic droplets in the planar direction was effectively minimized by the strong network of in-plane oriented CNs and accommodated in the thickness direction [17]. Notably, the thermal expansion in the thickness direction is practically insignificant because of the thinness (~100 μm) of the nanocomposites.

5.3.6. Thermo-electrical stability of the nanocomposite electrodes

The high thermal dimensional stability of the nanocomposite substrates resulted in the high-thermal-performing AgNW transparent electrodes (Fig. 5.8). The electrodes were repeatedly heated in the temperature range of 80 °C to 150 °C and cooled at −196 °C in air. No significant increase in the sheet resistance of the nanocomposite electrodes (TNE10 and TNE20) was observed even after five heating–cooling cycles (H5C5) with a heating temperature of up to 120 °C (Fig. 5.8a−c). In contrast, the AE (the non-reinforced electrode) exhibited a clear sign of increase in the sheet resistance, though insignificant, after H2C2 even with a heating temperature of 80 °C (Fig. 5.8a). The sheet resistance of AE increased rapidly above 100 °C with a cease of electrical conductivity after H4C4 and H3C3 when heated at 120 °C and 150 °C, respectively (Fig. 5.8b−d). In contrast, the nanocomposite electrodes remained conductive even after H5C5 with a high heating temperature of 150 °C (Fig. 5.8d−f). The sheet resistance increased to 698 Ω sq^{-1} for TNE10, and the increase was only up to 369 Ω sq^{-1} for TNE20.

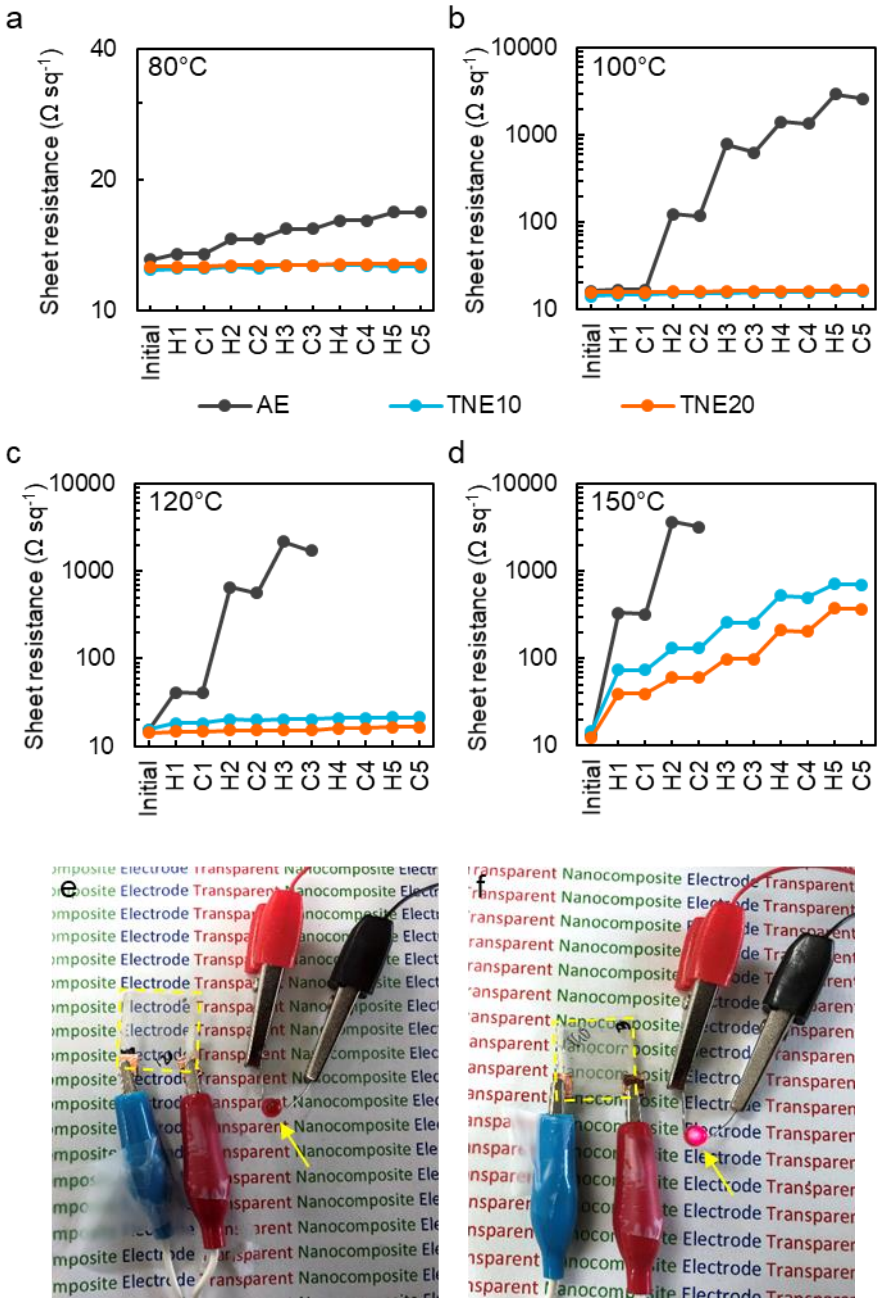

Figure 5.8. Thermo-electrical performance of transparent electrodes under cyclic heating and cooling at heating temperatures of (a) 80 °C, (b) 100 °C, (c) 120 °C, and (d) 150 °C and a cooling temperature of −196 °C. "H" refers to heating and "C" refers to cooling. (e) AE after H4C4, 120°C. (f) TNE20 after H5C5, 150 °C.

To support the above thermo-electrical result, the electrode samples were investigated using FE-SEM. FE-SEM images are presented in Figure 5.9. Evidence of fragmentation of the AgNWs on the AE after H4C4 when heated at 120 °C was observed (Figure 5.9c). In fact, the fragmentation of AgNWs most likely started at 100 °C, considering the rapid increase in sheet resistance observed in Figure 5.8b. In contrast, the AgNWs on the nanocomposite electrodes showed no conspicuous evidence of fragmentation even after H5C5 at the heating temperature of 120 °C, as observed in Figure 5.9d. FE-SEM images of the original AE and TNE10 electrodes are also presented in Figure 5.9a,b, respectively, for comparison. At the heating temperature of 150 °C, the AgNWs underwent thermal oxidation [13,38], as evident in Figure 5.9e,f. However, the extent of AgNW fragmentation was lower for the nanocomposite electrodes retrieved after H5C5 compared with for the AE retrieved after H3C3. Therefore, the nanocomposite electrodes could still conduct electricity even after five cycles of extreme heating and cooling (Fig. 5.8d,f). A decrease in the sheet resistance was observed after each cooling step for the AE electrodes, as shown in Figure 5.8. This decrease resulted from the high shrinkage of the acrylic plastic associated with the previous high expansion during heating, which possibly reconnected the fragmented AgNWs. The high shrinkage may have also accelerated the fragmentation or disconnection of the AgNWs in the subsequent heating steps by loosening their contacts in the nano-network. Clearly, the hierarchically CN-reinforced nanocomposite substrates, which were highly stable against the mechanical stresses generated in the acrylic plastic by the thermal shrinkage and expansion, led to the production of highly thermally stable electrodes by minimizing fragmentation and disconnection of the AgNWs.

In previous studies, it has been reported that the introduction of polyethoxysiloxane or various nanoparticles of TiO_2, Al_2O_3, SiO_2, ZrO_2, and ZnO into the AgNW layer can improve the thermal stability of the electrodes by minimizing thermal oxidation of the AgNWs, sometimes at the expense of a reduction in transparency [12−14]. In this study, a high-thermal-performing AgNW electrode with good electro-optical performance by developing a thermal dimensionally stable nanocomposite substrate that minimized the fragmentation of AgNWs was successfully demonstrated. Combining these present findings with those previously reported indicates that a high-performing electrode could be fabricated for application in future advanced devices.

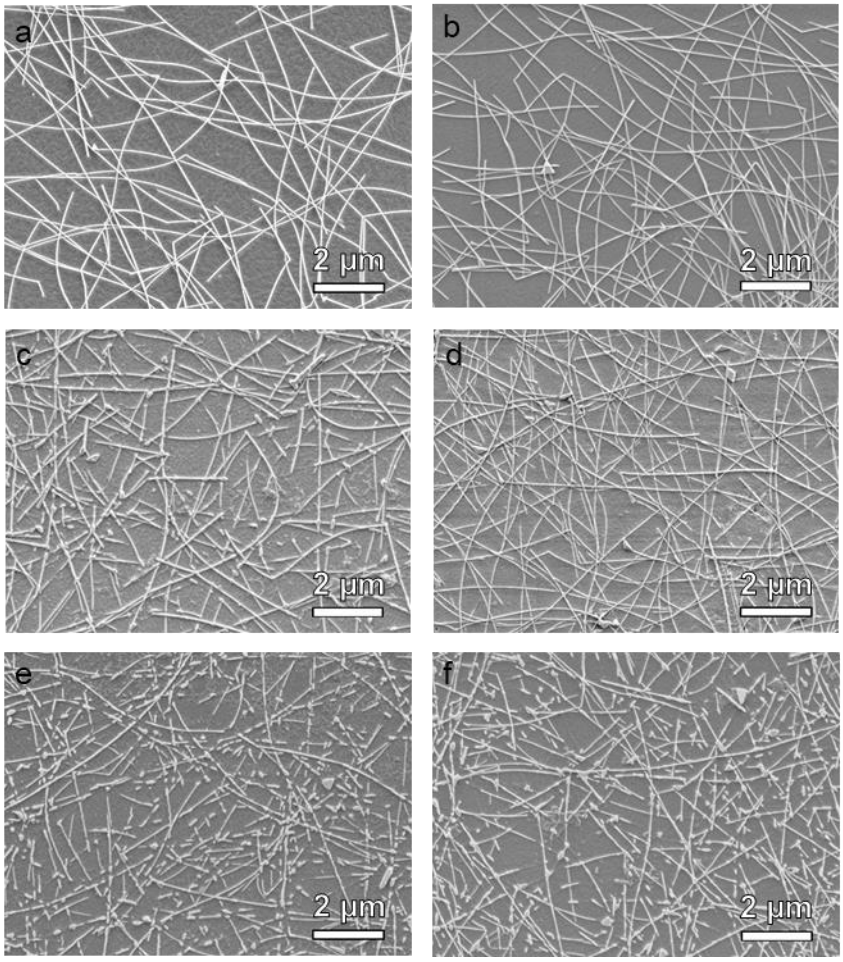

Figure 5.9. FE-SEM images of AgNWs on (A) AE before HC treatment, (B) TNE10 before HC treatment, (C) AE after H4C4@120 °C, (D) TNE10 after H5C5@120 °C, (E) AE after H3C3@150 °C, and (F) TNE10 after H5C5@150 °C.

5.3.7. Thermally stable smart liquid-crystal device

Finally, as a proof-of-concept, a high-thermal-performing transparency-modulating device, widely known as a polymer-dispersed liquid crystal (PDLC) device, was fabricated using the thermally stable nanocomposite electrodes (Fig. 5.10). The device maintained a stable on-state transparency (74% at 550 nm) even after 10 heating–cooling cycles (H10C10) at a heating temperature of 100 °C and cooling temperature of −30 °C (Fig. 5.10e). In contrast, the on-state transparency of a device fabricated using AE was reduced to 55% from 74% after H10C10 (Fig. 5.10f). This result also suggests that the CN-reinforced nanocomposite electrodes maintained a high thermo-electrical integrity because of their high thermal dimensional stability.

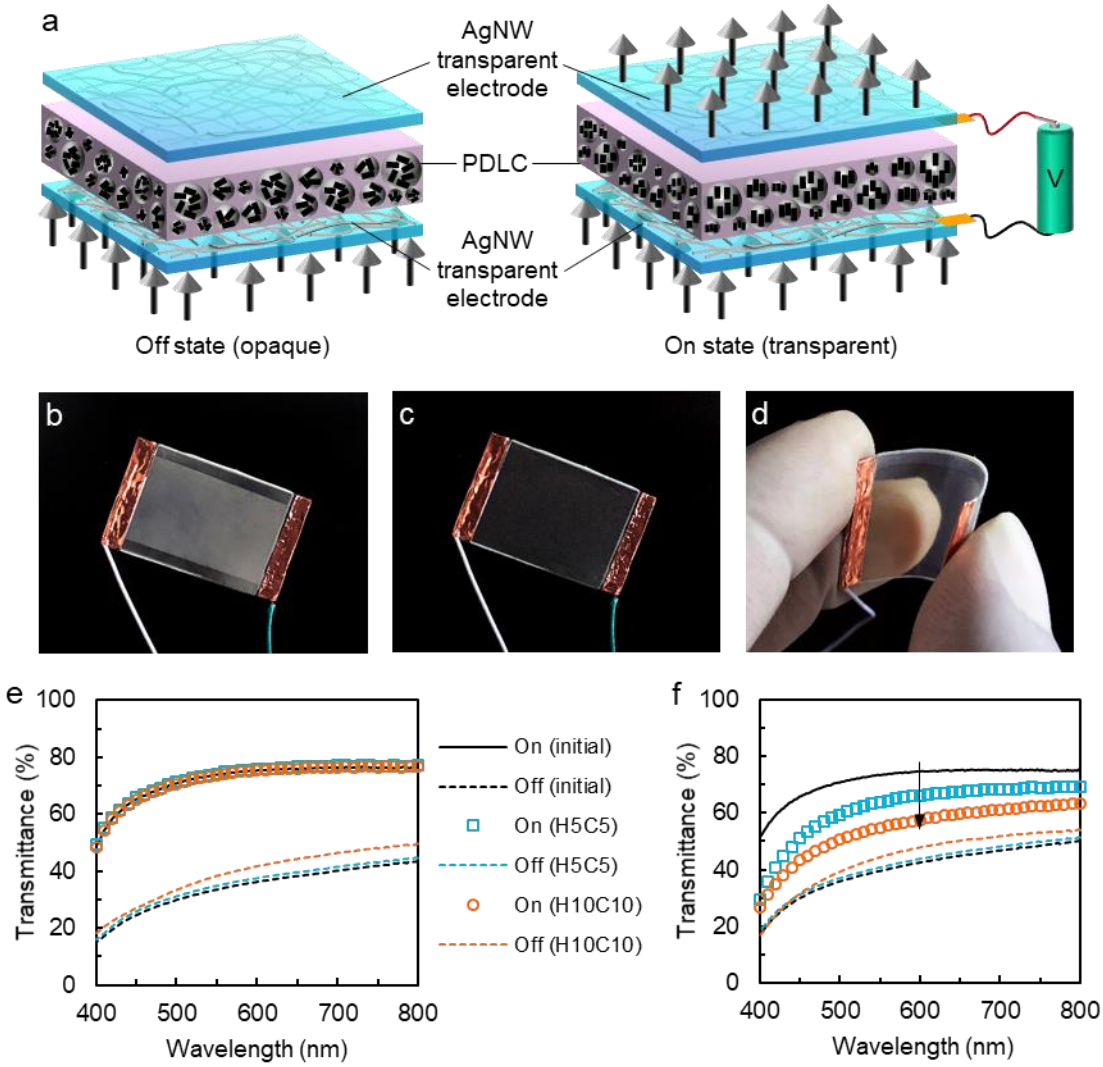

Figure 5.10. (a) Schematic illustration of PDLC device showing the modulation of transparency achieved by changing the alignment of the liquid crystals with an applied voltage. (b–d) Photographs of PDLC device fabricated on the nanocomposite electrodes in (b) off-state, (c) on-state, and (d) on-state under bending. Optical transmittances of the device fabricated on the (e) nanocomposite electrodes and (f) AEs after repeated HC treatment at a heating temperature of 100 °C and cooling temperature of −30 °C.

5.4 Summary

A high-thermal-performing transparent and flexible AgNW electrode was fabricated by developing a highly thermal dimensionally stable nanocomposite substrate. The high thermal-dimensional stability was achieved via hierarchical reinforcement from the CNs, the incredibly thermally stable natural materials. It was successfully demonstrated that The AgNW electrodes fabricated on the thermally improved nanocomposite substrates and the resulting device can

survive repeated heating and cooling at extreme temperatures. The nanocomposite substrates and their corresponding electrodes also possessed high mechanical properties even at an elevated temperature of 150 °C and good electro-optical properties, which were comparable to or even better than those of other plastic substrates and electrodes either available commercially or reported in the literature. In this study, the AgNWs were used as a representative of other conducting nanomaterials, such as graphene and carbon nanotubes. The findings of this study indicate that their high-thermal-performing transparent electrodes could also be fabricated using the thermally ameliorated nanocomposite substrate prepared via Pickering emulsion method. It is noteworthy that the findings of this study can be combined with findings reported previously in the literature to fabricate more upgraded transparent flexible electrodes for application in next-generation advanced devices.

5.5 References

1. Kumar A., and Zhou C. The race to replace tin-doped indium oxide: which material will win? ACS Nano, 2010, **4**, 11–14.
2. Kim I. C., Kim T.-H., Lee S. H., and Kim B.-S. Extremely foldable and highly transparent nanofiber-based electrodes for liquid crystal smart devices. Scientific Reports, 2018, **8**, 11517.
3. Yu L., Shearer C., and Shapter J. Recent development of carbon nanotube transparent conductive films. Chemical Reviews, 2016, **116**, 13413−13453.
4. Zhou Y., Azumi R., and Shimada S. A highly durable, stretchable, transparent and conductive carbon nanotube–polymeric acid hybrid film. Nanoscale, 2019, **11**, 3804–3813.
5. Wang X., Li Z., Xu W., Kulkarni S. A., Batabyal S. K., Zhang S., Cao A., and Wong L. H. TiO_2 nanotube arrays based flexible perovskite solar cells with transparent carbon nanotube electrode. Nano Energy, 2015, **11**, 728−735.
6. Kwon S.-J., Han T.-H., Ko T. Y., Li N., Kim Y., Kim D. J., Bae S.-H., Yang Y., Hong B. H., Kim K. S., Ryu S., and Lee T.-W. Extremely stable graphene electrodes doped with macromolecular acid. Nature Communication, 2018, **9**, 2037.
7. Han T.-H., Lee Y., Choi M.-R., Woo S.-H., Bae S.-H., Hong B. H., Ahn J.-H., and Lee T.-W. Extremely efficient flexible organic light-emitting diodes with modified graphene anode. Nature Photonics, 2012, **6**, 105−110.
8. Kuruvila A., Kidambi P. R., Kling J., Wagner J. B., Robertson J., Hofmann S., and Meyer J. Organic light emitting diodes with environmentally and thermally stable doped graphene

electrodes. Journal of Materials Chemistry C, 2014, **2**, 6940–6945.

9. Hu L., Kim H. S., Lee J.-Y., Peumans P., and Cui Y. Scalable coating and properties of transparent, flexible, silver nanowire electrodes. ACS Nano, 2010, **4**, 2955–2963.
10. Tokuno T., Nogi M., Karakawa M., Jiu J., Nge T. T., Aso Y., and Suganuma K. Fabrication of silver nanowire transparent electrodes at room temperature. Nano Research, 2011, **4**, 1215–1222.
11. Sim H., Kim C., Bok S., Kim M. K., Oh H., Lim G.-H., Cho S. M., and Lim B. Five-minute synthesis of silver nanowires and their roll-to-roll processing for large-area organic light emitting diodes. Nanoscale, 2018, **10**, 12087–12092.
12. Kumar D., Stoichkov V., Brousseau E., Smith G. C., and Kettle J. High performing AgNW transparent conducting electrodes with a sheet resistance of 2.5 Ω Sq^{-1} based upon a roll-to-roll compatible post-processing technique. Nanoscale, 2019, **11**, 5760–5769.
13. Liu B.-T., and Huang S.-X. Transparent conductive silver nanowire electrodes with high resistance to oxidation and thermal shock. RSC Advances, 2014, **4**, 59226–59232.
14. Vinogradov V. V., Agafonov A., and Avnir D. Conductive sol–gel films. Journal of Materials Chemistry C, 2014, **2**, 3914–3920.
15. Xiong J., Li S., Ye Y., Wang J., Qian K., Cui P., Gao D., Lin M.-F., Chen T., and Lee P. S. A deformable and highly robust ethyl cellulose transparent conductor with a scalable silver nanowires bundle micromesh. Advanced Materials, 2018, **30**, 1802803.
16. Ye S., Rathmell A. R., Chen Z., Stewart I. E., and Wiley B. J. Metal nanowire networks: The next generation of transparent conductors. Advanced Materials, 2014, **26**, 6670–6687.
17. Nogi M., and Yano H. Transparent nanocomposites based on cellulose produced by bacteria offer potential innovation in the electronics device industry. Advanced Materials, 2008, **20**, 1849–1852.
18. Starke Jr. E. A., Cornelia R. H., Greszczuk L. B., Karabin L. M., Lewandowski J. J., Saxena A., Seferis J. C., Tressler R. E., and Ward D. D. Accelerated aging of materials and structures: The effects of long-term elevated-temperature exposure. The National Academies Press, Washington D.C., USA, 1996, publication no. NMAB-479, pp. 7–10.
19. Nishino T., Matsuda I., and Hirao K. All-cellulose composite. Macromolecules, 2004, **37**, 7683–7687.
20. Dufresne A. Nanocellulose: A new ageless bionanomaterial. Materials Today, 2013, **16**, 220–227.
21. Wohlert J., Bergenstråhle-Wohlert M., and Berglund L. A. Deformation of cellulose nanocrystals: Entropy, internal energy and temperature dependence. Cellulose, 2012, **19**,

1821–1836.

22. Rao Y., and Blanton T. N. Polymer nanocomposites with a low thermal expansion coefficient. Macromolecules, 2008, **41**, 935–941.
23. Lee W. S., and Yu J. Comparative study of thermally conductive fillers in underfill for the electronic components. Diamond and Related Materials, 2005, **14**, 1647–1653.
24. Sullivan L. M., and Lukehart C. M. Zirconium tungstate (ZrW_2O_8)/polyimide nanocomposites exhibiting reduced coefficient of thermal expansion. Chemistry of Materials, 2005, **17**, 2136–2141.
25. MacDonald W. A., Looney M. K., MacKerron D., Eveson R., Adam R., Hashimoto K., and Rakos K. Latest advances in substrates for flexible electronics. Journal of the SID, 2007, **15**, 1075–1083.
26. Zeng X.-Y., Zhang Q.-K., Yu R.-M., and Lu C.-Z. A new transparent conductor: silver nanowire film buried at the surface of a transparent polymer. Advanced Materials, 2010, **22**, 4484–4488.
27. Ye S., Rathmell A. R., Stewart I. E., Ha Y.-C., Wilson A. R., Chen Z., and Wiley B. J. A rapid synthesis of high aspect ratio copper nanowires for high-performance transparent conducting films. Chemical Communications, 2014, **50**, 2562–2564.
28. Fang Z., Zhu H., Yuan Y., Ha D., Zhu S., Preston C., Chen Q., Li Y., Han X., Lee S., Chen G., Li T., Munday J., Huang J., and Hu L. Novel nanostructured paper with ultrahigh transparency and ultrahigh haze for solar cells. Nano Letters, 2014, **14**, 765 −773.
29. Ding K., Fang Y., Dong S., Chen H., Luo B., Jiang K., Gu H., Fan L., Liu S., Hu B., and Wang L. 24.1% external quantum efficiency of flexible quantum dot light-emitting diodes by light extraction of silver nanowire transparent electrodes. Advanced Optical Materials, 2018, **6**, 1800347.
30. Zhu H., Fang Z., Wang Z., Dai J., Yao Y., Shen F., Preston C., Wu W., Peng P., Jang N., Q Yu., Yu Z., and Hu L. Extreme light management in mesoporous wood cellulose paper for optoelectronics. ACS Nano, 2016, **10**, 1369−1377.
31. Li Y., Yu S., Chen P., Rojas R., Hajian A., and Berglund L. Cellulose nanofibers enable paraffin encapsulation and the formation of stable thermal regulation nanocomposites. Nano Energy, 2017, **34**, 541–548.
32. Wegst U. G. K., Bai H., Saiz E., Tomsia A. P., and Ritchie R. O. Bioinspired structural materials. Nature Materials, 2015, **14**, 23–36.
33. Jin J., Lee D., Im H.-G., Han Y. C., Jeong E. G., Rolandi M., Choi K. C., and Bae B.-S. Chitin nanofiber transparent paper for flexible green electronics. Advanced Materials, 2016,

28, 5169–5175.

34. Jeon H., Yoon C., Song Y.-G., Han J., Kwon S., Kim S., Chang I., and Lee K. Reducing the coefficient of thermal expansion of polyimide films in microelectronics processing using ZnS particles at low concentrations. ACS Applied Nano Materials, 2018, **1**, 1076−1082.
35. Yano H., Sugiyama J., Nakagaito A. N., Nogi M., Matsuura T., Hikita M., and Handa K. Optically transparent composites reinforced with networks of bacterial nanofibers. Advanced Materials, 2005, **17**, 153–155.
36. Fujisawa S., Togawa E., and Kuroda K. Facile route to transparent, strong, and thermally stable nanocellulose/polymer nanocomposites from an aqueous Pickering emulsion. Biomacromolecules, 2017, **18**, 266–271.
37. Song X., Yang S., Liu X., Wu M., Li Y., and Wang S. Transparent and water-resistant composites prepared from acrylic resins ABPE-10 and acetylated nanofibrillated cellulose as flexible organic light-emitting device substrate. Nanomaterials, 2018, **8**, 648.
38. Khaligh H. H., and Goldthorpe I. A. Failure of silver nanowire transparent electrodes under current flow. Nanoscale Research Letters, 2013, **8**, 235.

Chapter 6
Conclusions and Future Prospects

6.1 Conclusions

Aimed to address the issues of immiscibility of native hydrophilic nanocelluloses with hydrophobic resins and non-moldability of the transparent nanocellulose-reinforced composite materials prepared via impregnation method, in this study a very simple water-based method was devised by exploiting the idea of emulsification of oil and water. The dual role of the nanocelluloses as the stabilizer of the resin-in-water emulsion and resin reinforcing nano-component was utilized. The potential of this new method in order to fabricate structurally hierarchical, highly transparent, strong, tough, thermally-stable and macro-to-micro-moldable nanocomposites of hydrophilic 'native' nanocelluloses and hydrophobic resins for application in the next-generation optical devices was explored.

To develop novel transparent materials reinforced with native nanocelluloses, a resin-in-water Pickering emulsion stabilized solely by nanocelluloses was successfully prepared. Nanocellulose-reinforced transparent materials were successfully fabricated via vacuum-filtration of the resin-in-water Pickering emulsions. Because of the strong encapsulation of the resin droplets by the nanocellulose network, the loss of resin during emulsion filtration and nanocomposite processing was negligible. The high optical transparency of the nanocomposites, which was as high as 90%, indicated that a good dispersion of the network of hydrophilic nanocelluloses in a hydrophobic resin can be achieved via Pickering emulsification method without any chemical intervention. Interestingly, the nanocomposites had a unique self-assembled two-tie hierarchical architecture resulted from the aggregation of the nanocellulose-encapsulated resin droplets. The hierarchical structure resembled a brick-and-mortar-like structure, which was reversely similar to that of nacre.

Because of the hierarchical structure of the nanocomposites, they had a rare but desirable combination of high strength, toughness, mechanical flexibility compared to their counterparts prepared via the impregnation method. The resin droplet size also played a role to obtained nanocomposites with tunable mechanical properties but with a similar optical transparency irrespective of nanocelluloses content. Smaller sized droplets produced nanocomposites with high mechanical properties resulted from the more uniform hierarchical structure.

The effect of nanocellulose concentration in the emulsion was found of great importance in terms of morphology of the resin droplets and emulsion stability. As the nanocellulose concentration in the emulsion increased, a denser network was formed, resulting in higher viscosity and higher stability of the emulsions. However, the droplet size and polydispersity were increased with increasing viscosity, i.e., with increasing nanocellulose concentration. Interestingly, the nanocomposites had a high mechanical flexibility, about 2 times than that of neat resin, even with a nanocellulose content as high as 25 wt%. This was attributed to the distinct hierarchical structure of the nanocomposites that provided a synergistic load-bearing, stress-dissipating, crack-deflecting, and crack-delaying mechanism, as can be observed in nacre.

Meanwhile, because of the inclusion of liquid resin droplets in the nanocellulose-network, which also reduced the H-bonding among the nanofibrils, the nanocomposites could easily be molded into 3D-shaped transparent materials. Such a 3D molded transparent material could not be achieved via impregnation method. The surface of the nanocomposites could even be nano or micromolded easily by simple hot-pressing. The successful fabrication of 3D-molded transparent nanocomposites could open new application areas of the nanocellulose reinforced materials. Example of applications could be substrate for micro-electronic contact lens devices, substrate for curved and flexible displays, data storage devices, microlens arrays for high-resolution 3D-imaging, or anti-reflection substrate for the improved light-trapping by a thin-film solar cell.

Using nanocelluloses of different lengths and crystallinities, a tunable mechanical properties with high flexibility (high elongation-at-break) together with a tunable thermal properties were obtained even at a similar nanocelluloses content. This was due to the difference in the hierarchical microstructure resulted from different network structure of the nanocelluloses with different length and crystallinity around the resin droplets/platelets. The short nanocelluloses with high crystallinity produced stiffer and highly thermally stable nanocomposites; a CTE as low as that of silicon crystals was obtained only at a 10 wt% CN-content. This ultrahigh thermal dimensional stability was attributed due to the combination of a unique hierarchical structure of the nanocomposites and extremely low CTE of the highly crystalline short nanocelluloses. The nanocomposites were highly thermomechanically stable even up to 150 °C, compared to the commercial thermally-stable PET film. Interestingly, stronger nanocomposites were obtained using a combination of long and short nanocelluloses.

Furthermore, the optical transparency of the nanocomposites was highly stable even at 180 °C for 2 h. The high thermal stability of the micropatterns fabricated on the surface of the nanocomposite was also demonstrated.

Finally, to demonstrate the great potential of the transparent nanocomposites having an excellent thermal stability as the substrate for optoelectronic devices, a high-thermal-performing transparent and flexible AgNW electrode and a smart optical device were fabricated. It was successfully demonstrated that the resulting AgNW electrodes and smart optical device can survive repeated heating and cooling at extreme temperatures compared to those prepared on non-reinforced polymer films. This was because of the high thermal dimensional stability of the nanocomposite substrates owing to which the thermomechanical stress induced by temperature change was incredibly low, and hence, the conducting AgNW-network remained intact.

Therefore, it is expected that this study will provide significant insight to fabricate unique nanocomposites reinforced with nanocelluloses by using facile Pickering emulsification technique for the application in next-gen advanced optical materials.

6.2 Future prospects

The knowledge acquired in this study can be utilized to incorporate unique functionalities into the nanocellulose-reinforced nanocomposites. For example, as the Pickering emulsification process allows to encapsulate monomer resin into the nanocellulose shell, a self-healing nanocomposite material can be developed. It also would be interesting to form a nanocellulose-stabilized water-in-resin emulsion (note that in this study all of the emulsions prepared were resin-in-water, i.e., O/W type) or even a double emulsion, e.g., water-in-resin-in-water or resin-in-water-in-resin emulsion, with the possibility to obtain a self-healing material having self-reinforcing ability via the formation (or, release) of nanocellulose networks, akin to the formation of collagen fibers during would healing.

Possibility can be explored by incorporating sensitizer and emitter molecules in the resin droplets to fabricate a transparent nanocomposite substrate that would harvest or upconvert infrared portion of the solar radiation for high-efficiency photovoltaics.

Apart from making nanocomposites with unique functionalities, the Pickering emulsion stabilized by nanocelluloses may offer potential application in tribology. For example,

inclusion of resin micro-droplets in a CNF/water suspension can reduce its viscosity (Figure 2.10g in Chapter 2). Therefore, research on the lubricating behavior/performance of the nanocellulose-stabilized Pickering emulsion may open up new application areas of the nanocelluloses.

Last but not least, the emulsification is a well-established industrial process that are being frequently used in food, pharmaceutical, and cosmetics industries. Therefore, Pickering emulsification process using nanocelluloses could easily be scaled-up that would enable new functional applications of the nanocelluloses and the materials thereof.

Research Achievements

Publications

1. "Three-Dimensional-Moldable Nanofiber-Reinforced Transparent Composites with a Hierarchically Self-Assembled "Reverse" Nacre-like Architecture"
   Subir Kumar Biswas, Hironari Sano, Md. Iftekhar Shams, and Hiroyuki Yano. *ACS Applied Materials and Interfaces* **2017**, 9 (35), 30177−30184.
   [Chapter 2]

2. "Optically Transparent Tough Nanocomposites with a Hierarchical Structure of Cellulose Nanofiber Networks Prepared by Pickering Emulsion Method"
   Supachok Tanpichai*, **Subir Kumar Biswas***, Suteera Witayakran, and Hiroyuki Yano. (Submitted)
   ***Equal contributor**
   [Chapter 3]

3. "Thermally Superstable Cellulosic-Nanorod-Reinforced Transparent Substrates Featuring Microscale Surface Patterns"
   Subir Kumar Biswas, Supachok Tanpichai, Suteera Witayakran, Xianpeng Yang, Md. Iftekhar Shams, and Hiroyuki Yano. *ACS Nano* **2019**, 13 (2), 2015−2023.
   [Chapter 4]

4. "Highly Thermal-Resilient AgNW Transparent Electrode and Optical Device on Thermomechanically Superstable Cellulose Nanorod-Reinforced Nanocomposites"
   Subir Kumar Biswas, Hironari Sano, Xianpeng Yang, Supachok Tanpichai, Md. Iftekhar Shams, and Hiroyuki Yano. *Advanced Optical Materials* **2019**, 1900532, DOI: 10.1002/adom.201900532.
   [Chapter 5]

Awards

1. Best poster award, 5th Japan Association for Chemical Innovation (JACI)/Green Sustainable Chemistry (GSC) Symposium, Kobe, Japan, 2016.

2. Best poster award, 7th Annual Meeting of the Nanofiber Society of Japan, Kyoto, Japan 2016.

3. Best poster award, 4th International Cellulose Conference (ICC), Cellulose Society of Japan, Fukuoka, Japan 2017.

4. Best poster award (1st place), Joint Convention of the Society of Wood Science and Technology, USA (SWST) and Japan Wood Research Society (JWRS), Nagoya, Japan 2018.

5. Travel grant award, Joint Convention of the Society of Wood Science and Technology, USA (SWST) and Japan Wood Research Society (JWRS), Nagoya, Japan 2018.

Acknowledgements

First, I would like to thank and express my most sincere gratitude to Prof. Hiroyuki Yano for his kind supervision and support. Thank you for always being enthusiastic and optimistic, and for encouragement and delivering excellent ideas in the course of my study. I would also like to thank Assoc. Prof. Kentaro Abe and Prof. Fumiaki Nakatsubo for valuable discussions and encouragements. My sincere gratitude to Prof. Yoshinobu Tsujii of Division of Materials Chemistry, Institute for Chemical Research, and Prof. Masahisa Wada of Division of Forest and Biomaterials Science, Graduate School of Agriculture for critically reviewing this doctoral dissertation. Thanks to my laboratory colleagues, notably, Mr. Xianpeng Yang, Dr. Supachok Tanpichai (visiting researcher from King Mongkut's University of Technology Thonburi, Bangkok, Thailand) and Ms. Yoko Homma for their kind cooperation. I would also like to thank Dr. Hironari Sano for performing TEM imaging of my samples and Ms. Aya Miura for measuring the CTE of polycarbonate. Special thanks to Ms. Yuki Ishimaru for being so kind and providing me all the necessary administrative support. Finally, the scholarship grant (no. 143492) from the Ministry of Education, Culture, Sports, Science and Technology, Japan (MEXT-Monbukagakusho) is gratefully acknowledged.

Subir Kumar Biswas
June 2019

Title: Three-Dimensional-Moldable Nanofiber-Reinforced Transparent Composites with a Hierarchically Self-Assembled "Reverse" Nacre-like Architecture

Author: Subir K. Biswas, Hironari Sano, Md. Iftekhar Shams, et al

Publication: Applied Materials

Publisher: American Chemical Society

Date: Sep 1, 2017

PERMISSION/LICENSE IS GRANTED FOR YOUR ORDER AT NO CHARGE

This type of permission/license, instead of the standard Terms & Conditions, is sent to you because no fee is being charged for your order. Please note the following:

- Permission is granted for your request in both print and electronic formats, and translations.
- If figures and/or tables were requested, they may be adapted or used in part.
- Please print this page for your records and send a copy of it to your publisher/graduate school.
- Appropriate credit for the requested material should be given as follows: "Reprinted (adapted) with permission from (COMPLETE REFERENCE CITATION). Copyright (YEAR) American Chemical Society." Insert appropriate information in place of the capitalized words.
- One-time permission is granted only for the use specified in your request. No additional uses are granted (such as derivative works or other editions). For any other uses, please submit a new request.

Title: Thermally Superstable Cellulosic-Nanorod-Reinforced Transparent Substrates Featuring Microscale Surface Patterns

Author: Subir K. Biswas, Supachok Tanpichai, Suteera Witayakran, et al

Publication: ACS Nano

Publisher: American Chemical Society

Date: Feb 1, 2019

PERMISSION/LICENSE IS GRANTED FOR YOUR ORDER AT NO CHARGE

This type of permission/license, instead of the standard Terms & Conditions, is sent to you because no fee is being charged for your order. Please note the following:

- Permission is granted for your request in both print and electronic formats, and translations.
- If figures and/or tables were requested, they may be adapted or used in part.
- Please print this page for your records and send a copy of it to your publisher/graduate school.
- Appropriate credit for the requested material should be given as follows: "Reprinted (adapted) with permission from (COMPLETE REFERENCE CITATION). Copyright (YEAR) American Chemical Society." Insert appropriate information in place of the capitalized words.
- One-time permission is granted only for the use specified in your request. No additional uses are granted (such as derivative works or other editions). For any other uses, please submit a new request.

JOHN WILEY AND SONS LICENSE TERMS AND CONDITIONS

Jun 01, 2019

This Agreement between Kyoto University -- Subir Biswas ("You") and John Wiley and Sons ("John Wiley and Sons") consists of your license details and the terms and conditions provided by John Wiley and Sons and Copyright Clearance Center.

License Number	4600551412747
License date	Jun 01, 2019
Licensed Content Publisher	John Wiley and Sons
Licensed Content Publication	Advanced Optical Materials
Licensed Content Title	Highly Thermal-Resilient AgNW Transparent Electrode and Optical Device on Thermomechanically Superstable Cellulose Nanorod-Reinforced Nanocomposites
Licensed Content Author	Hiroyuki Yano, Md. Iftekhar Shams, Supachok Tanpichai, et al
Licensed Content Date	May 6, 2019
Licensed Content Volume	0
Licensed Content Issue	0
Licensed Content Pages	9
Type of use	Dissertation/Thesis
Requestor type	Author of this Wiley article
Format	Print and electronic
Portion	Full article
Will you be translating?	No
Title of your thesis / dissertation	Optically Transparent Nanocellulose-Reinforced Composites via Pickering Emulsification
Expected completion date	Sep 2019
Expected size (number of pages)	152
Requestor Location	Kyoto University Laboratory of Active Bio-based Materials RISH Gokasho Uji, Kyoto 611-0011 Japan Attn: Kyoto University
Publisher Tax ID	EU826007151
Total	0.00 USD
Terms and Conditions	

TERMS AND CONDITIONS

This copyrighted material is owned by or exclusively licensed to John Wiley & Sons, Inc. or one of its group companies (each a"Wiley Company") or handled on behalf of a society with which a Wiley Company has exclusive publishing rights in relation to a particular work (collectively "WILEY"). By clicking "accept" in connection with completing this licensing transaction, you agree that the following terms and conditions apply to this transaction (along with the billing and payment terms and conditions established by the Copyright Clearance Center Inc., ("CCC's Billing and Payment terms and conditions"), at the time that you opened your RightsLink account (these are available at any time at http://myaccount.copyright.com).

Terms and Conditions

- The materials you have requested permission to reproduce or reuse (the "Wiley Materials") are protected by copyright.

- You are hereby granted a personal, non-exclusive, non-sub licensable (on a stand-alone basis), non-transferable, worldwide, limited license to reproduce the Wiley Materials for the purpose specified in the licensing process. This license, **and any CONTENT (PDF or image file) purchased as part of your order,** is for a one-time use only and limited to any maximum distribution number specified in the license. The first instance of republication or reuse granted by this license must be completed within two years of the date of the grant of this license (although copies prepared before the end date may be distributed thereafter). The Wiley Materials shall not be used in any other manner or for any other purpose, beyond what is granted in the license. Permission is granted subject to an appropriate acknowledgement given to the author, title of the material/book/journal and the publisher. You shall also duplicate the copyright notice that appears in the Wiley publication in your use of the Wiley Material. Permission is also granted on the understanding that nowhere in the text is a previously published source acknowledged for all or part of this Wiley Material. Any third party content is expressly excluded from this permission.

- With respect to the Wiley Materials, all rights are reserved. Except as expressly granted by the terms of the license, no part of the Wiley Materials may be copied, modified, adapted (except for minor reformatting required by the new Publication), translated, reproduced, transferred or distributed, in any form or by any means, and no derivative works may be made based on the Wiley Materials without the prior permission of the respective copyright owner.**For STM Signatory Publishers clearing permission under the terms of the STM Permissions Guidelines only, the terms of the license are extended to include subsequent editions and for editions in other languages, provided such editions are for the work as a whole in situ and does not involve the separate exploitation of the permitted figures or extracts,** You may not alter, remove or suppress in any manner any copyright, trademark or other notices displayed by the Wiley Materials. You may not license, rent, sell, loan, lease, pledge, offer as security, transfer or assign the Wiley Materials on a stand-alone basis, or any of the rights granted to you hereunder to any other person.

- The Wiley Materials and all of the intellectual property rights therein shall at all times remain the exclusive property of John Wiley & Sons Inc, the Wiley Companies, or their respective licensors, and your interest therein is only that of having possession of and the right to reproduce the Wiley Materials pursuant to Section 2 herein during the continuance of this Agreement. You agree that you own no right, title or interest in or to the Wiley Materials or any of the intellectual property rights therein. You shall have no rights hereunder other than the license as provided for above in Section 2. No right, license or interest to any trademark, trade name, service mark or other branding ("Marks") of WILEY or its licensors is granted hereunder, and you agree that you shall not assert any such right, license or interest with respect thereto

- NEITHER WILEY NOR ITS LICENSORS MAKES ANY WARRANTY OR REPRESENTATION OF ANY KIND TO YOU OR ANY THIRD PARTY, EXPRESS, IMPLIED OR STATUTORY, WITH RESPECT TO THE MATERIALS OR THE ACCURACY OF ANY INFORMATION CONTAINED IN THE MATERIALS, INCLUDING, WITHOUT LIMITATION, ANY IMPLIED WARRANTY OF MERCHANTABILITY, ACCURACY, SATISFACTORY QUALITY, FITNESS FOR A PARTICULAR PURPOSE, USABILITY, INTEGRATION OR NON-INFRINGEMENT AND ALL SUCH WARRANTIES ARE HEREBY EXCLUDED BY WILEY AND ITS LICENSORS AND WAIVED BY YOU.

- WILEY shall have the right to terminate this Agreement immediately upon breach of this Agreement by you.

- You shall indemnify, defend and hold harmless WILEY, its Licensors and their respective directors, officers, agents and employees, from and against any actual or threatened claims, demands, causes of action or proceedings arising from any breach of this Agreement by you.

- IN NO EVENT SHALL WILEY OR ITS LICENSORS BE LIABLE TO YOU OR ANY OTHER PARTY OR ANY OTHER PERSON OR ENTITY FOR ANY SPECIAL, CONSEQUENTIAL, INCIDENTAL, INDIRECT, EXEMPLARY OR PUNITIVE DAMAGES, HOWEVER CAUSED, ARISING OUT OF OR IN CONNECTION WITH THE DOWNLOADING, PROVISIONING, VIEWING OR USE OF THE MATERIALS REGARDLESS OF THE FORM OF ACTION, WHETHER FOR BREACH OF CONTRACT, BREACH OF WARRANTY, TORT, NEGLIGENCE, INFRINGEMENT OR OTHERWISE (INCLUDING, WITHOUT LIMITATION, DAMAGES BASED ON LOSS OF PROFITS, DATA, FILES, USE, BUSINESS OPPORTUNITY OR CLAIMS OF THIRD PARTIES), AND WHETHER OR NOT THE PARTY HAS BEEN ADVISED OF THE POSSIBILITY OF SUCH DAMAGES. THIS LIMITATION SHALL APPLY NOTWITHSTANDING ANY FAILURE OF ESSENTIAL PURPOSE OF ANY LIMITED REMEDY PROVIDED HEREIN.

- Should any provision of this Agreement be held by a court of competent jurisdiction to be illegal, invalid, or unenforceable, that provision shall be deemed amended to achieve as nearly as possible the same economic effect as the original provision, and the legality, validity and enforceability of the remaining provisions of this Agreement shall not be affected or impaired thereby.

- The failure of either party to enforce any term or condition of this Agreement shall not constitute a waiver of either party's right to enforce each and every term and condition of this Agreement. No breach under this agreement shall be deemed waived or excused by either party unless such waiver or consent is in writing signed by the party granting such waiver or consent. The waiver by or consent of a party to a breach of any provision of this Agreement shall not operate or be construed as a waiver of or consent to any other or subsequent breach by such other party.

- This Agreement may not be assigned (including by operation of law or otherwise) by you without WILEY's prior written consent.

- Any fee required for this permission shall be non-refundable after thirty (30) days from receipt by the CCC.

- These terms and conditions together with CCC's Billing and Payment terms and conditions (which are incorporated herein) form the entire agreement between you and WILEY concerning this licensing transaction and (in the absence of fraud) supersedes all prior agreements and representations of the parties, oral or written. This Agreement may not be amended except in writing signed by both parties. This Agreement shall be binding upon and inure to the benefit of the parties' successors, legal representatives, and authorized assigns.

- In the event of any conflict between your obligations established by these terms and conditions and those established by CCC's Billing and Payment terms and conditions, these terms and conditions shall prevail.

- WILEY expressly reserves all rights not specifically granted in the combination of (i) the license details provided by you and accepted in the course of this licensing transaction, (ii) these terms and conditions and (iii) CCC's Billing and Payment terms

and conditions.

- This Agreement will be void if the Type of Use, Format, Circulation, or Requestor Type was misrepresented during the licensing process.

- This Agreement shall be governed by and construed in accordance with the laws of the State of New York, USA, without regards to such state's conflict of law rules. Any legal action, suit or proceeding arising out of or relating to these Terms and Conditions or the breach thereof shall be instituted in a court of competent jurisdiction in New York County in the State of New York in the United States of America and each party hereby consents and submits to the personal jurisdiction of such court, waives any objection to venue in such court and consents to service of process by registered or certified mail, return receipt requested, at the last known address of such party.

WILEY OPEN ACCESS TERMS AND CONDITIONS

Wiley Publishes Open Access Articles in fully Open Access Journals and in Subscription journals offering Online Open. Although most of the fully Open Access journals publish open access articles under the terms of the Creative Commons Attribution (CC BY) License only, the subscription journals and a few of the Open Access Journals offer a choice of Creative Commons Licenses. The license type is clearly identified on the article.

The Creative Commons Attribution License

The Creative Commons Attribution License (CC-BY) allows users to copy, distribute and transmit an article, adapt the article and make commercial use of the article. The CC-BY license permits commercial and non-

Creative Commons Attribution Non-Commercial License

The Creative Commons Attribution Non-Commercial (CC-BY-NC)License permits use, distribution and reproduction in any medium, provided the original work is properly cited and is not used for commercial purposes.(see below)

Creative Commons Attribution-Non-Commercial-NoDerivs License

The Creative Commons Attribution Non-Commercial-NoDerivs License (CC-BY-NC-ND) permits use, distribution and reproduction in any medium, provided the original work is properly cited, is not used for commercial purposes and no modifications or adaptations are made. (see below)

Use by commercial "for-profit" organizations

Use of Wiley Open Access articles for commercial, promotional, or marketing purposes requires further explicit permission from Wiley and will be subject to a fee.

Further details can be found on Wiley Online Library

http://olabout.wiley.com/WileyCDA/Section/id-410895.html

Other Terms and Conditions:

v1.10 Last updated September 2015

Questions? customercare@copyright.com or +1-855-239-3415 (toll free in the US) or +1-978-646-2777.